High Power Laser - Plasma Interactions for Homeland Security Applications

by

Jungmoo Hah

A dissertation submitted in partial fulfillment
of the requirements for the degree of
Doctor of Philosophy
(Nuclear Engineering and Radiological Sciences)
in The University of Michigan
2018

Doctoral Committee:

Associate Professor Alexander G. R. Thomas, Co-Chair
Professor Karl M. Krushelnick, Co-Chair
Research Scientist Mark D Hammig
Research Scientist John A. Nees
Assistant Professor Louise Willingale

Jungmoo Hah

jmhah@umich.edu

ORCID iD: 0000-0001-5349-0988

To God who is alway faithful

and my wife who is my best friend and supporter

ACKNOWLEDGEMENTS

This dissertation and my Ph.D. journey in Ann Arbor would not have been possible without support from many people. I would like to take this opportunity to sincerely thank them.

First, I am immensely grateful to my advisor, Professor Alec Thomas for his guidance and unwavering support throughout my doctoral studies at Michigan. Thank you for allowing me to join such a wonderful research group – High Field Science group at CUOS, University of Michigan, and your excellent mentorship. To my advisor, Professor Karl Krushelnick, thank you for all your support and insightful comments. Thanks to your advice, I was able to have many breakthroughs during my Ph.D. years. Your hot dogs at the HFS picnic was the best one I ever had! Research Scientist John Nees, I really appreciate all your time and effort to keep the Lambda-Cubed laser alive and operative. From you, I learned a lot about lasers and optics. Also, you inspired me to think as a scientist. To Research Scientist Mark Hammig, thank you for serving on my committee and helping me to expand my research area. I also thank you for your help on my neutron experiment. Also, thanks go to my committee member, Professor Louise Willingale. Your challenging questions improved my dissertation, and I want to thank you for providing detailed comments on my thesis.

Special thanks go to the HFS group members. Dr. Zhaohan He, you are a great lab-mate, and thank you for teaching me how to operate the Lambda-Cubed laser and do lab work. To my cohort of the HFS group, Dr. Keegan Behm and Thomas Batson, you helped me a lot, not only finishing the coursework but also preparing

for the qualifying exam. Tony, Peter, Paul, Amina and Jinpu, thanks for being great group members. To my close friends, Hyeongseok Kim, Jihang Lee, and Eun Seong Moon, thanks for your support and prayers.

Finally, I want to thank all my family members, my parents, Cheonkey Hah and Jungae Kang, my parents-in-law, Young Ha Kim and Jong Nam Park, my brother, Jungdo Hah, my brother-in-law and his wife, Soomin Kim and Jina Bang, and their newly-born twins, Joonwoo and Yeonwoo, for their endless support and encouragement. Last, but by no means least, my dear wife, Dam Hee Kim, for her unbelievable support and prayers. To my wife, I dedicate this dissertation.

TABLE OF CONTENTS

LIST OF FIGURES

Figure

LIST OF TABLES

Table

LIST OF ABBREVIATIONS

AO Adaptive Optics

ASE Amplified Spontaneous Emission

BBO Beta Barium Borate

CCD Charge Coupled Device

CdTe Cadmium Telluride

CPA Chirped Pulsed Amplification

CR39 Allyl Diglycol Carbonate or Columbia Resin 39

CTR Coherent Transition Radiation

CUOS Center for Ultrafast Optical Science

DM Deformable Mirror

FOM Figure-of-Merit

FROG Frequency Resolved Optical Gating

FWHM Full Width at Half Maximum

FWM Four Wave Mixing

GA Genetic Algorithm

HEU Highly Enriched Uranium

HPGe High Purity Germanium Detector

LWFA Laser Wakefield Accelerator

MCNP Monte Carlo N-Particle

Nd:YAG Neodymium doped Yttrium Aluminum Garnet

OAP Off-Axis Parabolic mirror

OR Optical Rectification

PIC Particle-in-Cell

PMT Photo-Multiplier Tubes

SHG Second Harmonic Generation

SNM Special Nuclear Material

SPM Self-phase Modulation

SSNTD Solid-State Nuclear Track Detector

THz Terahertz

TNSA Target Normal Sheath Acceleration

ToF Time-of-Flight

ABSTRACT

Advance in laser technology over the last few decades have allowed progress in intense laser-plasma interaction research. The relativistic plasma generated by intense laser pulses can generate many different forms of radiation. This radiation, including X-rays, has been studied intensively due to the numerous potential applications of these sources. For example, for Homeland Security, radiation sources are already utilized to detect dangerous materials and hidden items that threaten civil safety. Neutrons and THz radiation have been studied as candidates for next generation screening, which may complement typical X-ray techniques. This thesis contains three experimental studies of high-power laser-plasma interactions as sources of radiation for Homeland Security applications, especially at kilohertz repetition-rates using few-millijoule pulses.

First, a neutron generation experiment was conducted using a high repetition-rate laser system (½ kHz) at the University of Michigan. A heavy water (D_2O) stream was irradiated by 40 fs pulses, each containing a few millijoules of energy. Acceleration of deuterons (to $E < 1$ MeV) was achieved through plasma sheath acceleration. Ensuing DD nuclear fusion reactions, in turn, generated neutron fluxes of up to 10^5 s^{-1} into 4π steradians. In order to understand the neutron source characteristics, deuteron spectra were measured with CR39 detectors and compared to particle-in-cell (PIC) relativistic plasma dynamics simulations. The neutron source characteristics were analyzed using various neutron detection techniques, including Time-of-Flight measurements, bubble detectors, and neutron-capture gamma-ray measurements.

Second, THz generation from laser filamentation in air was investigated. For security applications, THz can complement X-ray scanning, because THz can detect non-metallic materials and dangerous chemicals while not ionizing the sample. Even though there have been extensive studies on THz generation from laser filamentation processes, the exact generation mechanisms are yet to be determined. In this thesis, optimization of THz radiation using an adaptive optic with active feedback was demonstrated. Using a genetic algorithm, the THz radiation was improved six-fold without the need for detailed knowledge of the mechanisms. In particular, the use of a high repetition-rate laser system accelerated the optimization of the THz signal. Another strength of this optimization system is that it can enhance certain THz generation mechanisms depending on the experimental circumstances.

Lastly, using a nanosecond pulsed high-power laser system (10 Hz), a long-range detection technique was developed for detection of special nuclear materials. Although direct detection of radiation from nuclear materials can be defeated by radiation shielding, leakage of radiation-ionized gases can provide an alternative indicator of the existence of nuclear materials. For instance, in the presence of ionizing radiation, the ratio of ionized nitrogen to neutral nitrogen would be higher than in no-source air-plasma conditions. By inducing optical breakdown (plasma) near a sample's position, the ionization levels of the surrounding air were analyzed. To enhance the detection efficiency, an adaptive-optic feedback system was introduced with this ratio as a figure-of-merit. This resulted in a 50 % enhancement in the spectral ratio of the nitrogen lines. In addition, aerosol-initiated plasma spectra were distinguished from the original air-breakdown plasma, as a step toward practical deployment.

Role of the author

The author would like to clarify that the work presented in this thesis is a result of collaboration, with other students and research scientists contributing to the studies. The author was responsible for performing all of the studies presented in this thesis except for the following work: In Chapter IV, the 2D Particle-in-Cell (PIC) simulation work was performed by Dr. George Petrov at Naval Research Laboratory. The neutron capture measurement using High Purity Germanium Detector (HPGe) detectors and its Monte Carlo N-Particle (MCNP) simulation were conducted by Dr. Mark Hammig at the University of Michigan. The Michelson interferometer setup in Chapter V was built by Wei Jiang (visiting scholar from University of Electronic Science and Technology of China). Chapter VI includes some previous results from a DTRA basic research project ("Active Detection of Fissile Materials via Laser-Induced Ionization- Seeded Plasmas") performed by Dr. Geehyun Kim and Dr. Inyong Kwon.

CHAPTER I

Introduction

1.1 Motivation – Homeland security

Following the use of two nuclear weapons in 1945, the world became aware of the significance of atomic/nuclear power. Nuclear proliferation accelerated during the Cold War. While the Cold War effectively ended after the fall of the Berlin Wall, an enormous stockpile of nuclear weapons still threaten global security. Today, more than 16,000 nuclear weapons and 137 tons of Highly Enriched Uranium (HEU) exist [1]. However, some of the weapons are thought to be unsecured or may be illicitly acquired. Special Nuclear Material (SNM) that could be used as source material for nuclear devices also affect global security. SNM includes fissile materials, U-233, U-235 and Pu-239. Every year, more than 100 million ground vehicles cross the U.S.-Canada and U.S.-Mexico borders and more than 6 million cargo containers enter through the U.S. seaports (see Fig. 1.1) [2–4]. Among the vast number of container volumes, only 2% of are opened and inspected across borders. A real threat is that rogue agents could smuggle SNM across the boarders using one of these millions of cargo containers. Practically, it is impossible to perform open-inspection to every container. Instead, a possible option is to inspect containers without opening them using highly reliable detection techniques.

In order to secure and suppress the spread of SNM, one can try to detect the

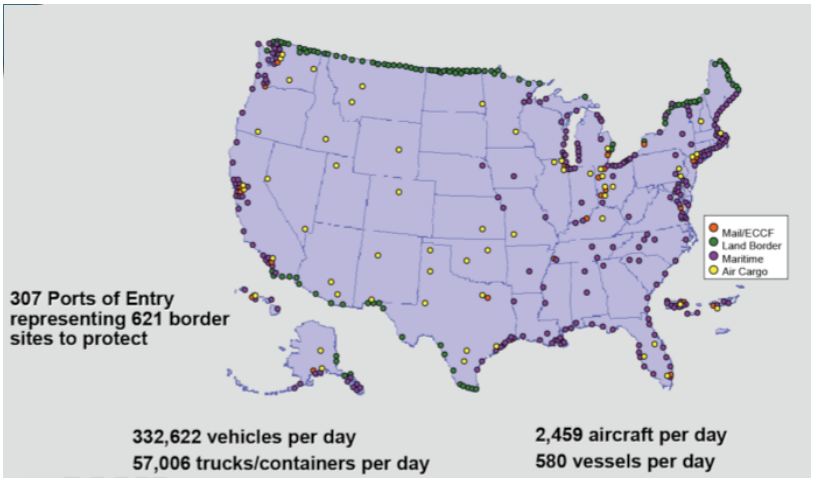

Figure 1.1 Ports of U.S. entry, Image is from Ref. [4]

radiation emitted by the materials. The most common device to detect this radiation is a gas-filled detector such as a Geiger−Müller tube. This kind of detector uses a Townsend avalanche to obtain an electrical signal from ionization events. It had been relied on for the technique of *passive* detection, where the particles emitted from radioactive decay (photons and or neutrons) are used to identify the SNM. Passive detection is simple to deploy but rather ineffective; when the SNMs are shielded. For instance, the most prominent spectral feature of HEU is a photopeak at 185 keV from ^{235}U. Figure 1.2 shows a computer-modeled γ-ray pulse-height spectra from HEU along with background radiation. The 185 keV photopeak feature is easily attenuated by a thin lead slab, and when measured with background signals (a mixture of potassium, thorium, and uranium in soil), the shielding removes the feature and it is barely noticeable. Another trackable particle for passive detection is the neutron. When the SNM experiences a spontaneous fission reaction, neutrons are emitted along with other fission products. These neutrons can easily penetrate typical high-Z shielding materials or other obstacles between the detector and the source SNM because the neutron is not electrically charged. To detect the neutrons, gas-filled detectors and scintillation detectors are used.

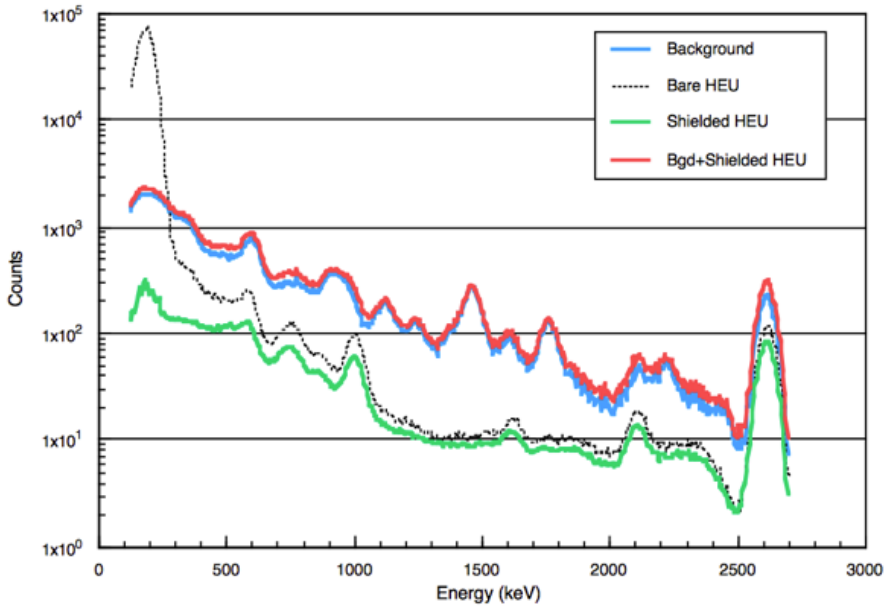

Figure 1.2 Computer synthesized NaI γ-ray pulse-height spectra from HEU and background radiation [5].

1.2 Active interrogation for SNM detection

Passive detection schemes are able to detect radioactivity from SNM, but in most cases the intensity of the signal and the radiation energies are low [6, 7], resulting in poor SNM detection efficiency. In security contexts, most SNM is concealed or heavily shielded, defeating passive detection. To detect shielded SNM, high-energy photons (gamma rays or X-rays) and/or neutrons may be used. These can penetrate many layers of shielding materials and then activate the SNM, thereby inducing fission reactions. As a result of these reactions, other high-energy photons and/or neutrons are produced, which are energetic enough to escape the shielding or surrounding materials. In this case, the energetic photons and neutrons may be detected. This process is known as *active interrogation*. The resultant photon and neutron signals will be released on different time scales; they are emitted promptly or with a delay according to the various nuclear reactions. These reactions can be controlled by the interrogation source (i.e., the interrogating particle type and its energy). Specific

reactions may therefore be induced, and these secondary radiation signals can reveal detailed information on the tested cargo to identify potential SNM. In addition, the increased emission flux due to active interrogation can increase the signal-to-noise ratio.

One example of a deployed active interrogation device is the "Neutron car wash" [8, 9]. Figure 1.3 shows a schematic of the system. It consists of a neutron generator as an interrogation source and detector-array walls to detect the neutron-induced signals. When a cargo container with hidden SNM is scanned by the system, neutrons *wash* the container and fission reactions occur through neutron. Gamma rays or other neutrons released by fission reactions are subsequently detected by the scintillation detector arrays.

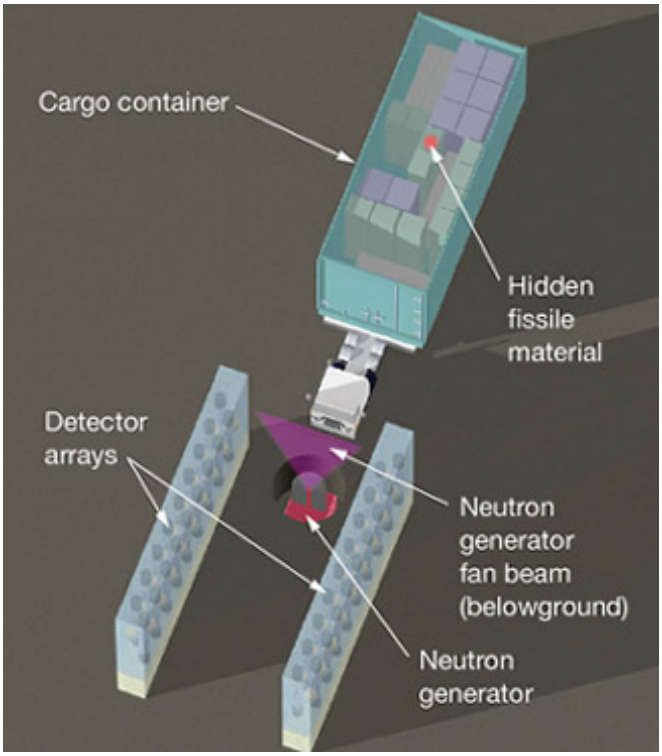

Figure 1.3 A design of "Neutron car wash" system. Image is adapted from [3].

Current sources for active interrogation include conventional accelerators, which

are used to generate photons and/or neutrons. Photons may be generated by conversion of accelerated electrons by *bremsstrahlung*. For example, a typical radio frequency-linear accelerator (RF-LINAC) operating at 100 kHz repetition-rate may generate a high energy electron beam that, in turn, generates photons when the electrons scatter from a strong atomic potential in a high-Z target such as lead. The photon spectrum is determined by the electron energy and Z of the material. A commercially available LINAC-based cargo inspection system (Rapiscan Eagle) has been tested and is currently in use for this application [10]. DD and DT generators may be used as a neutron source, with characteristic energies (in the center-of-mass frame) of 2.45 MeV for DD or 14.1 MeV for DT. The interrogation energy can be adjusted by controlling the deuteron energy and sampling the neutrons from different angles.

Different kinds of nuclear reactions can take place by active interrogation with these sources. A major fission process producing fission fragments. Through the fission processes, gammas and/or neutrons are emitted, both prompt and delayed. The high-energies of delayed gammas ($>$ 3MeV) are uniquely distinguished from the activation of shielding materials and their strong intensity allows for easy detection of the signal over background [3, 11].

Neutrons are complementary to X-rays, which may also be generated by laser-plasma interactions simultaneously. X-rays experience strong attenuation through high-Z materials, but neutrons exhibit a high sensitivity to low-Z materials such as hydrogen and/or organic materials. Potential cover materials for SNMs, in context of smuggling, include lead housing which may be used to shield radiation from inside (fission) and outside (interrogation). Neutrons, however, can penetrate lead housing with almost no attenuation, thereby driving nuclear reactions in the SNM. These reactions yield secondary energetic particles including gamma-ray and/or other neutrons. These secondary particles can reveal information about the activated SNMs through the shielding materials.

1.3 THz for homeland security applications

THz pulses are another kind of radiation used for Homeland Security applications. They have interesting features that may be applied to various fields including biomedicine, basic science research, imaging and security. Typically, "THz" radiation describes radiation in the frequency band from 0.3 to 30 THz, but this definition is somewhat flexible and depends on the research field. THz radiation has a low photon energy (< 10 meV) compared to the other sources described for active interrogation (i.e. gamma-rays) and so obviously cannot be used for active interrogation. THz radiation is used to excite longer wavelength vibrations, such as molecular vibrations in an organic material. This characteristic of THz radiation is a very favorable feature for other homeland security applications. For example, THz radiation can detect dangerous materials in organic forms such as (non-SNM) explosives, or illicit drugs [12, 13]. Such organic materials are not detectable using X-ray techniques. THz technology is a good complement to X-ray detectors for security screening, especially considering that it is non-ionizing, and as such is safer than other radiation for detecting hidden objects or materials on people. Because of these benefits, THz is currently used in airport security in the form of THz spectral-fingerprinting or THz imaging (see Fig. 1.4) [13, 14].

1.4 Laser-plasma based sources for homeland security

Laser-plasma interactions are able to generate many forms of radiation that may be used for Homeland Security applications. For active interrogation schemes, a source of radiation is required, which is not suitable for passive detection, and may be provided by a laser-plasma source. Although conventional accelerator based photon/neutron sources are currently already used for active interrogation, there are further requirements such as a system compactness or portability, a low overall radia-

Figure 1.4 Terahertz image of men with a non-metallic knife hidden with a newspaper. [13]

tion dose (to minimize radiation except in the testing area), and long-range or remote detection. As an alternative to conventional accelerators, laser-plasma based accelerators may have advantages as they are potentially more compact and also produce short, controllable bursts of radiation.

After the laser-plasma wakefield accelerator was proposed by Tajima and Dawson [15] in 1979, laser-plasma based electron acceleration schemes have been intensively studied. As laser technology has improved, more energetic electron beams have been produced. The beams, however, had a large energy spread [16–19], limiting their further application. In 2004, the generation of monoenergetic electron beams was demonstrated, expanding their potential applications [20–22]. Currently, laser-wakefield accelerators can accelerate electrons to energies exceeding multi-GeV [23–26]. In addition to generation of gamma-rays by bremsstrahlung [27–29], strong THz radiation can be generated [30, 31].

Intense laser-matter interactions are also able to generate energetic ions from high density foils [32–34]. By introducing a secondary target, accelerated ions may collide with target ions, driving nuclear fusion reactions, generating neutrons, for example. These fusion-neutron sources have some benefits over other fission/spallation neutron sources; they are triggered by a compact and ultrafast laser, they have: (1) compact system designs, (2) short burst durations. These characteristics of the laser-driven techniques may allow a variety of new potential applications in scientific, medical and security areas. Energetic neutrons from laser-plasma based schemes may be used as a source for active interrogation and nuclear activation.

Beyond Homeland Security applications, neutron imaging with its unique properties is an ideal technique for characterizing the structure and morphology of hydrogen-containing materials. For materials science applications, the following characteristics of neutrons are ideal for imaging applications [35]: (1) contrast for neighboring elements in the periodic table, (2) large penetration distance for many commonly used structural elements and (3) the ability to distinguish isotopes. These benefits are also applicable to industry applications. For example, non-destructive testing with neutron phase-contrast imaging is useful to observe areas concealed by metallic layers [36].

1.5 Dissertation outline

This thesis describes work done to systematically study the generation of radiation with the relativistic λ^3 laser system and a Q-switched Neodymium doped Yttrium Aluminum Garnet (Nd:YAG) laser for applications in Homeland Security.

- Chapter II introduces basic concepts and laser-plasma physics that are used in the thesis. This chapter will cover basic concepts relating to modern high-power lasers and optics, laser absorption and interaction mechanisms with plasma. A

theoretical overview follows, on how radiation for Homeland Security applications can be generated from laser-plasma interactions.

- Chapter III describes the laser systems and radiation diagnostics used in this thesis. Adaptive optics and active feedback for optimization are also described in this chapter.

- Chapter IV presents a study on laser-based short-pulsed neutron source development. Room temperature D_2O target experiments are described and results are discussed. To better determine the neutron source characteristics, supporting 2D particle-in-cell simulations and MATLAB analysis follow.

- Chapter V describes THz generation from a femtosecond laser system. In order to achieve stronger THz radiation, a novel optimization technique is applied using adaptive optics. Improvement of the THz radiation is analyzed.

- Chapter VI focuses on a scheme to sense SNM using a laser based detection. Using an Nd:YAG laser, air breakdown is induced and its spectral analysis reveals the existence of SNM near the laser focal region. Adaptive optics with a genetic algorithm is also applied to the detection system to quantify ratios between neutral and ionized nitrogen emission lines. As a practical consideration, emission initiated by environmental particles are measured and analyzed.

- Chapter VII draws conclusions and gives a future perspective of laser-plasma based radiation sources for active interrogation and Homeland Security applications.

CHAPTER II

Basic concepts

2.1 Nonlinear optics

As a laser intensity increases, the electric field of the laser pulse becomes strong enough to affect the optical properties of materials even before the strong electric field frees electrons from atoms. The dielectric polarization ($\mathbf{P}$) of the modified media responds to the applied laser electric field ($\mathbf{E}$) nonlinearly. Due to the nonlinear response, a number of nonlinear optical phenomena occur, such as frequency-mixing and the Kerr effect. Below, the theoretical background for relevant nonlinear optical effects is discussed.

From Maxwell's equations, the free space wave equation is derived as follows:

$$-\nabla^2\mathbf{E} + \mu_0\frac{\partial^2\mathbf{D}}{\partial^2 t} = 0 \tag{2.1}$$

When the wave travels through a medium, the electric field affects the electric displacement by inducing a local electric dipole moment $\mathbf{P} = \epsilon_0\chi\mathbf{E}$. Here the constant of proportionality χ is called the electric susceptibility of the material. Thus, the modified electric displacement can be rewritten as follows:

$$\mathbf{D} \equiv \epsilon_0\mathbf{E} + \mathbf{P} = \epsilon_0(1+\chi)\mathbf{E} = \epsilon\mathbf{E} \tag{2.2}$$

where $\epsilon = \epsilon_0\epsilon_r$ is the permittivity, and $\epsilon_r = 1 + \chi$ is the relative permittivity of the material.

Substituting Eqn. 2.2 into Eqn. 2.1 gives

$$-\nabla^2\mathbf{E} + \mu_0\epsilon_0\frac{\partial^2(1+\chi)\mathbf{E}}{\partial^2 t} = 0 \tag{2.3}$$

When the wave passes through the medium, an extra term related to χ or polarization field ($\chi\mathbf{E}$) is added to the simple free space wave equations. The polarization field can be expanded using a Taylor expansion

$$\chi\mathbf{E} = \chi^{(1)}\mathbf{E} + \chi^{(2)}\mathbf{E}^2 + \chi^{(3)}\mathbf{E}^3 + ... \tag{2.4}$$

Hence, when the incident E-field becomes stronger, the nonlinear terms introduce new physical phenomena, entering the regime of *nonlinear optics*.

One of the most important effects caused by the $\chi^{(2)}$ term is Second Harmonic Generation (SHG). Consider the electric field $\mathbf{E}_\omega$(t) at frequency ω and amplitude E_ω with a static electric field E_0

$$\mathbf{E}_\omega(t) = E_\omega(e^{i\omega t} + e^{-i\omega t}) \tag{2.5}$$

The second-order term $\mathbf{P}^{(2)}$(t) with a non-zero $\chi^{(2)}$ can be calculated as follows:

$$\begin{aligned}\mathbf{P}^{(2)}(t) &= \chi^{(2)}\mathbf{E}^2(t) \\ &= \chi^{(2)}[E_\omega e^{i\omega t} + E_\omega e^{-i\omega t} + E_0]^2 \\ &= \chi^{(2)}[E_\omega^2(e^{i2\omega t} + e^{-i2\omega t}) + 2E_0E_\omega(e^{i\omega t} + e^{-i\omega t}) + 2E_\omega^2 + E_0^2]\end{aligned} \tag{2.6}$$

The second-order field contains two different oscillation frequencies, ω and 2ω. In Eqn. 2.6, the first term indicates the field radiating at frequency, 2ω, which is referred to as SHG, but is not proportional to the DC field strength, The second term, however,

oscillates at the frequency ω, and it brings about the linear electro-optic effect, which can vary the refractive index in the medium. The last two non-oscillating terms are known as Optical Rectification (OR), which are quasi-DC components converted from the oscillating field.

The third-order coefficient, $\chi^{(3)}$ represents the optical Kerr effect. From the Taylor expansion of the refractive index, n, the first nonlinear term is proportional to the intensity, I

$$n \approx n_0 + n_2 I = n + \frac{\chi^{(3)}_{eff}}{4n_0^2 \epsilon_0 c} I \tag{2.7}$$

were, n_2 is the nonlinear index of refraction, and is on the order of 3 $\times 10^{-19}$ $\frac{\text{cm}^2}{\text{W}}$ for air and 3×10^{-16} $\frac{\text{cm}^2}{\text{W}}$ for glass. The optical Kerr effect gives rise to Self-phase Modulation (SPM) and self-focusing, otherwise known as Kerr lensing. SPM occurs when an ultrashort laser pulse travels in a medium and nonlinearly modifies the medium's refractive index. The change in refractive index by the laser pulse will produce a phase shift. The SPM process can be derived as follows:
for simplicity, assume a Gaussian ultrashort pulse shape with a constant phase, so the intensity profile is described by

$$I(t) = I_0 \text{exp}\left(-\frac{t^2}{\tau^2}\right) \tag{2.8}$$

where, I_0 is the peak intensity and τ is the half of the pulse duration. When the pulse propagates in a medium, the refractive index will be modified (Eqn. 2.7), and its time dependence is given by

$$\frac{dn(I)}{dt} = n_2 \frac{dI}{dt} = n_2 I_0 \left(-\frac{2t}{\tau^2}\right) \exp\left(-\frac{t^2}{\tau^2}\right) \tag{2.9}$$

This time-varying component of the refractive index causes a phase shift of the pulse

(Eqn. 2.10a) and consequently a frequency shift (Eqn. 2.10b).

$$\phi(t) = \omega_0 t - kz = \omega_0 t - \frac{2\pi}{\lambda_0} n(I) L \tag{2.10a}$$

$$\omega(t) = \frac{d\phi(t)}{dt} = \omega_0 - \frac{2\pi L}{\lambda_0}\frac{dn(I)}{dt} = \omega_0 + \frac{4\pi L n_2 I_0}{\lambda_0 \tau^2} \cdot t \cdot \exp\left(-\frac{t^2}{\tau^2}\right) \tag{2.10b}$$

The frequency shift by Eqn. 2.10b implies that the leading edge of the pulse becomes *redder* and the trailing edge of the pulse becomes *bluer*, in other words, the laser pulse experiences (up-)chirp, and spectral broadening by SPM. This SPM process also takes place in plasma through a relativistic nonlinearity [37]. In a spatial frequency domain, a similar process takes place, causing self-focusing. The self-focusing causes optical damage on a gain medium and limits a generation of high peak power laser systems until an invention of Chirped Pulsed Amplification (CPA) technique. This will be explained more in the following section (Sec. 2.2). In addition, from other nonlinearities we may observe Four Wave Mixing (FWM) or multi-photon absorption processes. These will be discussed more in Chapter V.

2.2 Laser physics

Since the invention of the laser in 1960, laser science has developed very rapidly. Particularly, with regard to the peak laser intensity, there were two important milestones in the early stages of laser technology development called Q-switching and mode-locking. As a consequence of these two techniques, laser pulse durations have been shortened from the nanosecond scale using the Q-switching to the scales of a few femtoseconds using Kerr-lens mode-locking (Ti:Sapphire). With these two techniques, peak power (and focused intensity) increased but optical damage caused by nonlinear effects in the amplifier limited further improvements to approximately a peak focused intensity of 10^{15} Wcm^{-2}. However in 1985, Strickland and Mourou introduced the CPA technique, which allowed the generation of relativistic intensity

laser pulses ($> 10^{18}$ Wcm^{-2}) [38].

2.2.1 Chirped pulse amplification

For modern high power laser systems, the CPA technique is employed. CPA allows an increase in the laser intensity in the gain material. In order to increase intensity beyond the nonlinearity threshold, a laser pulse is first stretched in duration using a grating. After the stretcher, the seed pulse is *positively* chirped, meaning that the low frequency components are ahead of high frequency components. As a result, the peak power/intensity of the pulse is reduced by a factor of 10^3 to 10^5. Then it is passed through amplifiers without detrimental nonlinear effects. The amplified and stretched pulse is then compressed back to the short pulse width using a grating-based compressor, which removes the chirp. As a result, a high quality beam is efficiently extracted from the gain material and can be focused to have more than 10^{19} Wcm^{-2} intensity. A simple diagram illustrating CPA is shown in Fig. 2.1. This technique has allowed ultra intense laser systems with focused intensities up to 10^{22} Wcm^{-2} [39] and has opened up a new field of relativistic plasma-physics.

Many CPA laser systems employ Titanium-doped sapphire (Ti:Sapph, Ti:Al_2O_3) as a gain medium for the oscillator and the amplifier because it has the necessary properties; (1) broad gain bandwidth, (2) good energy storage capability, (3) good optical quality and (4) high thermal conductivity. Because it can support broad gain bandwidths up to several hundred nanometers ($\sim$ 230 nm), theoretically, Ti:Sapphire lasers can generate few femtosecond pulse ($\geq$ 5 fs). Using Fourier theory, a simple relationship between the pulse duration (τ) and spectral bandwidth ($\Delta\omega$) of the laser pulse is given as follows:

$$\Delta\omega \cdot \tau \;\geq\; 2\pi C_B \tag{2.11}$$

where, C_B is 0.441 for a Gaussian pulse. With a cryogenic cooling system, the high

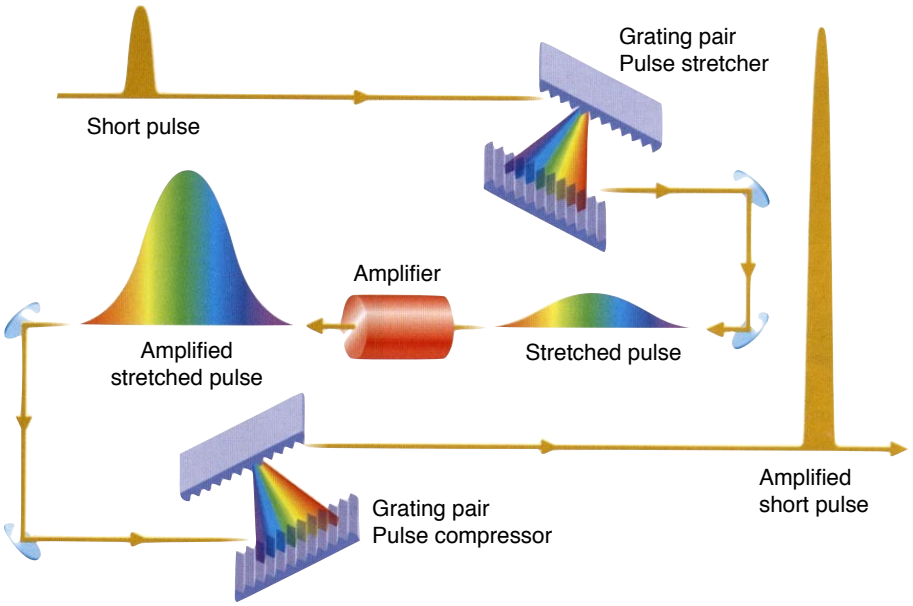

Figure 2.1 A schematic diagram of a chirped pulse amplification laser system. An initial femtosecond laser pulse is stretched using a grating pair. In the stretcher, the low-frequency component of the laser pulse travels a shorter path than the high-frequency component does, resulting in longer pulse duration than the original by a factor of 10^3 to 10^5. The stretched pulse is amplified through an amplifier. Due to the long pulse duration, a pulse can be amplified without damaging the optical components. After amplification, the pulse is recompressed by another pair of gratings, at which the dispersed frequency components of the pulse are combined. As a result, an amplified short pulse is generated. The image is adapted from the website (`https://cuos.engin.umich.edu/researchgroups/hfs/facilities/chirped-pulse-amplification`)

thermal conductivity allows Ti:Sapphire lasers to operate at a high repetition-rate. For example, the λ^3 laser at the Center for Ultrafast Optical Science (CUOS) at University of Michigan, can generate 30 fs pulses with up to 20 mJ energy at ½ kHz.

2.3 Laser plasma interactions

2.3.1 Optical field ionization

When the laser electric field is strong enough, the field may ionize the atoms in the medium thereby creating a *plasma*. The ionization process in its simplest form

can be considered as an energy transfer from an incident photon to an electron in an atom resulting in release of the electron. If the photon energy is higher than ionization potential of the atom, the atom will be ionized (i.e., direct ionization). Typical ionization potentials are higher than 5 eV, corresponding to an ultraviolet wavelength (Figure 2.2).

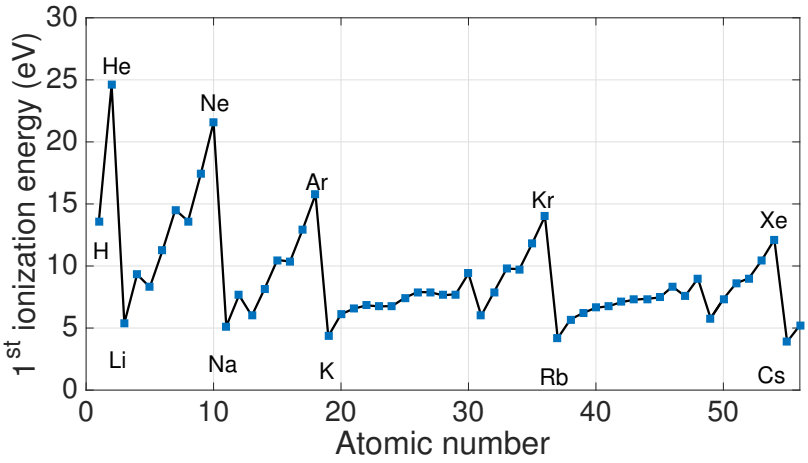

Figure 2.2 First ionization energies of atoms

While Infrared and visible light cannot directly ionize an atom, a nonlinear process can occur, and two or more photons may be absorbed, resulting in a nonlinear ionization process known as multiphoton ionization (MPI) [40, 41]. Alternatively, a very strong electric field introduced by the laser may be able to suppress the atomic potential barrier in the atom, allowing bound electrons to be freed from the atom, which is known as barrier suppression ionization (BSI). Even if the electric field is not strong enough to cause BSI, electrons may also *tunnel* through the distorted potential barrier, a quantum process known as tunnel ionization. Figure 2.3 shows schematics of these ionization processes.

2.3.2 Collisional ionization by electron impact

Through laser-plasma interactions, free electrons may be accelerated by various mechanisms (the details of the electron acceleration processes are not discussed here).

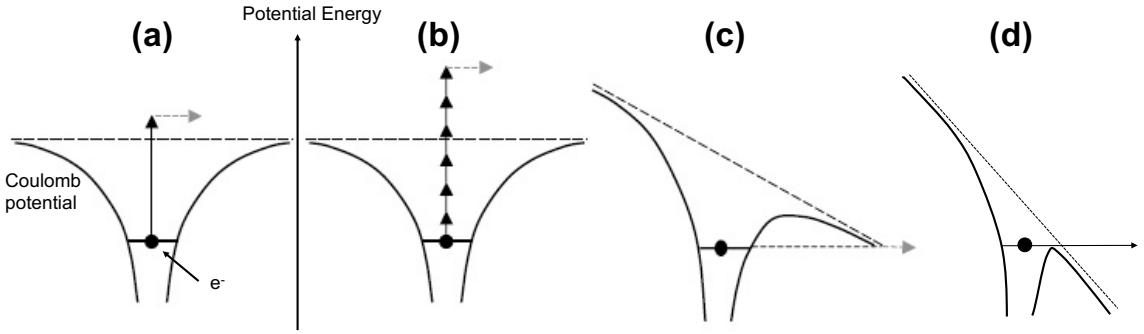

Figure 2.3 Simple schematics of ionization mechanisms: (a) direct ionization, (b) multiphoton ionization, (c) tunneling ionization and (d) barrier suppression ionization.

When these energetic electrons collide with atoms or ions, bound electrons may be released. This process is known as collisional ionization and it is described by

$$e^- + A^{Z+} \rightarrow 2e^- + A^{(Z+1)+} \tag{2.12}$$

where A^{Z+} denotes an atom or ion of charge Z. Equation 2.12 shows a single ionization process, but more than one electron could be released from a single collision of a highly energetic electron, albeit with lower probability.

2.3.3 Relativistic effects

In ultra-intense laser plasma interactions, *relativistic* effects must be included when considering the electron motion. In this regime, we may approximately account for relativistic effects by substituting the electron mass with a relativistic "effective mass" $\langle\gamma\rangle m_e$, where $\langle\gamma\rangle$ is the average Lorentz factor. Using the energy-momentum relation $\gamma m_e c^2 = E = \sqrt{p^2c^2 + m_e^2c^4}$, for circular polarization the Lorentz factor may be defined as follows.

$$\langle\gamma\rangle = \left\langle \sqrt{1 + \frac{p^2}{m_e^2c^2}} \right\rangle = \sqrt{1 + a_0^2} \tag{2.13}$$

where, a_0 is the normalized vector potential.

$$a_0 = \frac{p_{osc}}{m_e c} = \frac{e_0 E}{m_e \omega c} = \sqrt{\frac{I\lambda_\mu^2}{1.37 \times 10^{18}}}\ , \tag{2.14}$$

where λ_μ is the laser wavelength in micrometers and intensity I in unit of Wcm^{-2}. The relativistic correction modifies many laser-plasma parameters. For instance, the plasma frequency (ω_p), one of the most important plasma parameters will decrease under relativistic conditions because the effective mass ($\langle\gamma\rangle m_e$) increases, resulting in a larger effective inertia. This also modifies the dispersion relation of electromagnetic waves in the plasma, which may change it from opaque to transparent. The transparency of the plasma is also connected to the plasma skin depth ($\delta = c/\omega_p$). Relativistically induced transparency allows the laser to penetrate into (overdense) plasma.

From the Lorentz equation, one can derive a force that charged particles experiences in an inhomogeneous oscillating electromagnetic fields.

$$\frac{d\mathbf{p}}{dt} = \frac{\partial p}{\partial t} + \mathbf{v} \cdot \nabla \mathbf{p} - e(\mathbf{E} + \mathbf{v} \times \mathbf{B}) \tag{2.15}$$

where $\mathbf{p} = \gamma m_e \mathbf{v}$ is momentum of the electron. It can be shown that the longitudinal component ($\mathbf{p}_L$) can be expressed as

$$\frac{\partial \mathbf{p_L}}{\partial t} = e\nabla\phi - m_0 c^2 \nabla \sqrt{1 + \frac{p^2}{m_0^2 c^2}}\ , \tag{2.16}$$

where $e\nabla\phi$ is the electrostatic force, and the second term of the right-hand side is called the ponderomotive force. Rewriting this equation as follows to show the laser electric field explicitly:

$$F_{pond} = -\nabla[\langle\gamma - 1\rangle m_0 c^2] = \frac{-e^2}{4m_0\omega^2}\nabla|E|^2 \tag{2.17}$$

, where $\langle\rangle$ denotes the average over the period of the laser. Equation 2.17 shows that the spatially varying electric fields can exert a force, which is proportional to the gradient of laser intensity. Thus the charged particles migrate toward the lower intensity regions of the laser.

2.3.4 Laser absorption

As an intense laser pulse travels though plasma, its propagation is governed by the plasma density (or plasma frequency), which is described by the *dispersion relation*. For simplicity, by assuming a cold, unmagnetized, collisionless plasma and ignoring ion motion, the dispersion relation for a plane electromagnetic wave is given by

$$\omega_0^2 = \omega_p^2 + (k_0 c)^2 \tag{2.18}$$

where ω_0 is the laser frequency and $\omega_p = \sqrt{\frac{n_e e^2}{\gamma \epsilon_0 m_e}}$ is the electron plasma frequency. From Eqn. 2.18, the critical density can be obtained easily by putting when $\omega_p = \omega_0$, so that,

$$n_c = \gamma \frac{m_e \epsilon_0 \omega_0^2}{e^2} = 1.12 \times 10^{21} \frac{\gamma}{\lambda_\mu^2} [\mathrm{cm}^{-3}] \tag{2.19}$$

When the incident laser frequency is equal to the plasma frequency, the wavenumber (k) becomes zero, and the plasma becomes opaque and reflective, at which point the plasma density is called the critical density. When the plasma density is lower than critical density ($n_e < n_c$) it is termed 'underdense', and the other case ($n_e > n_c$) is termed 'overdense'. When the laser pulse travels into plasma, the laser can penetrate the underdense region up to the critical density surface. In the overdense region of plasma ($\omega_0 < \omega_p$), the wavenumber becomes imaginary, the electrons shields out the laser field so the laser wave becomes evanescent with a skin depth, $\delta = c/\omega_p$. At this surface, laser pulse energy can be coupled efficiently into the plasma by a number of different absorption mechanisms.

Resonance absorption

When a P-polarized electromagnetic wave travels with an oblique incident angle (θ), resonance absorption is one of the possible laser-absorption mechanisms. The laser wave drives a plasma wave in a surface plasma with a sufficiently long wavelength. The wave travels through the plasma and experiences a varying index of refraction. As a result of the oblique incidence, there can be a component of the electric field that oscillates along the density gradient direction, (i.e., $\mathbf{E} \cdot \nabla n_e \neq 0$). Part of the energy of the incident light wave is transferred to an electrostatic oscillation (electron plasma wave) [42]. At the reflection surface, Poisson's equation gives

$$\nabla \cdot (\varepsilon \mathbf{E}) = \varepsilon \nabla \cdot \mathbf{E} + \nabla \varepsilon \cdot \mathbf{E} = 0 \tag{2.20}$$

where, $\varepsilon = \varepsilon(z) = 1 - \frac{\omega_p^2(z)}{\omega^2}$. Eqn 2.20 can be rewritten as

$$\nabla \cdot \mathbf{E} = -\frac{1}{\varepsilon}\frac{\partial \varepsilon}{\partial z}\mathbf{E}_z \ . \tag{2.21}$$

It indicates a resonant response when ε=0, i.e., where ω_p=ω. However, assuming with ascending density profile, the obliquely incident laser may not reach the critical surface, if it reflects off at the surface having a density $n_e = n_c \cos^2\theta$ (which is derived using an S-polarization wave.) Its evanescent field, however, may still reach the critical surface and excite resonance.

Brunel heating

In contrast to resonance absorption, the *Brunel* or vacuum heating mechanism is effective even when the laser interacts with steep density gradients. At the critical surface, resonantly driven plasma oscillations with electric field (E_p) will occur at approximately the same frequency as the incident laser field (E_L). Electrons will be

pulled from the surface and returned with approximately the quiver velocity over a half cycle, leading to energy transfer. The amplitude of quiver oscillation is given by

$$x_p \simeq eE_L/m_e\omega^2 = v_{osc}/\omega \ . \tag{2.22}$$

For an exponential plasma profile ($n_e \propto exp[-\frac{x}{L}]$), if the oscillation amplitude (x_p) is greater than density scale length (L), the resonance will break down. The fractional absorption rate is derived from a capacitor approximation model and is given by

$$\eta_\alpha = \frac{4}{\pi} a \frac{sin^3\theta}{cos\theta} \tag{2.23}$$

where $a = v_{osc}/c$. Two relativistic corrections are required from Eqn. 2.23 in the reduced driving field amplitude and relativistic electron velocities. For strong relativistic conditions ($fa\sin\theta \gg 1$, here, f=1+(1−η_α)$^{1/2}$), the corrected absorption rate is given by

$$\eta^{rel} = \frac{4\pi\alpha'}{(\pi + \alpha')^2} \tag{2.24}$$

where $\alpha' = sin^2\theta/cos\theta$, and the peak appears at $\theta_{\rm opt}$=73°. The detailed derivations of Eqns. 2.23 and 2.24 are described in Ref. [43].

j×B heating

When the laser is incident normal to the target surface, the laser E-field is parallel to the target surface and therefore electrons cannot be driven into the target by the electric field. However, the strong B-field of the ultra-intense laser also can affect the electrons motion and result in electrons being accelerated into the target through the Lorentz force. This is presented in the second term on the right hand side of the

equation of motion (Eqn. 2.25)

$$\mathbf{F} = m\left(\frac{\partial \mathbf{v}}{\partial t} + \mathbf{v}\cdot\nabla\mathbf{v}\right) = q(\mathbf{E} + \mathbf{v}\times\mathbf{B}) \tag{2.25}$$

An electron accelerated by the E-field of the laser moves perpendicular to the B-field, and hence the vector product of these two vectors is directed along the laser propagation axis ($\mathbf{k}$). The electron will penetrate into the overdense plasma where the laser fields are shielded by the plasma. This absorption mechanism is known as relativistic $\mathbf{j}\times\mathbf{B}$ heating.

2.3.5 Laser-driven ion acceleration

In this section, a summary of some laser-plasma ion acceleration mechanisms is presented. Details of the physics of intense laser-driven ion acceleration and its recent experimental accomplishments and underlying theoretical explanations were reviewed by Macchi *et al.* and Passoni *et al.* in Refs. [44, 45].

Compared to electron acceleration, direct ponderomotive ion acceleration to relativistic energies using an intense laser system requires more than six orders of magnitude higher intensity ($> 10^{24}$ Wcm^{-2}). Even if direct ion acceleration would be hard to achieve using current laser systems ($<10^{22}$ Wcm^{-2}), the dynamics of electrons accelerated by such lasers can generate strong electrostatic fields ($>$ TV/m) due to charge separation along the target surface. By this strong E-field, ion acceleration can be achieved.

Depending on the laser parameter and target characteristics, many different ion acceleration mechanisms have been explored. Target Normal Sheath Acceleration (TNSA)[46] is the most extensively studied. When a thin foil target (solid density) is irradiated by a laser pulse, hot electrons are stripped from the target and penetrate the target, having a certain divergence due to collisions with background material.

These electrons produce strong electrostatic fields at the rear surface of the target (surface facing away from the arriving laser beam) when they leave the target, thereby generating a *sheath* field. The electric field of the sheath is established in the *target normal* direction and can accelerate ions to energies in excess of an MeV in a distance of $\sim 1\mu$m. The direction of the ion acceleration can be controlled by varying the plasma characteristic scale length [47]. This can be done through judicious choice of laser parameters as discussed in Chapter IV.

In the early stages of research into ion acceleration from intense laser-solid interactions, protons were the most significant contribution to the accelerated ions, in part due to their low mass. This was true even for non-hydrogen containing targets. The target surface is typically contaminated by hydrocarbons or water [48, 49], which are the origin of these protons. Several efforts have been reported to obtain heavy ion acceleration by suppressing the acceleration from the contamination layers. For example, cleaning of the target rear surface [50] and target pre-heating techniques [48, 51] have suppressed the proton contribution by two orders of magnitude. A deuteron target-coating method (heavy water ice and/or deuterated plastic) can be applied to accelerate deuterons selectively [52–54]. These accelerated deuterons are able to trigger fusion reactions such as $\mathrm{d}(d,n)^3\mathrm{He}$ and $^7\mathrm{Li}(d,n)^8\mathrm{Be}$. Laser-based acceleration mechanisms can therefore provide beams of fast neutrons. These have unique properties for applications such as imaging or detection of SNM, as distinguished from X-rays or ion sources [55–57].

Target normal sheath acceleration

From the late 20th century on, experimental demonstrations of ion acceleration (up to several MeVs) has been reported from intense laser interactions with different types of targets, from thin solid targets [58–60], gas targets [61, 62] and clusters [63, 64]. In 2000, collimated proton beams of several MeV were accelerated from the

rear side of thin solid targets [32–34]. The low beam-divergence of these protons coupled with the Bragg peak characteristic of ion energy deposition could make them favorable for applications such as medical ion beam therapy. From Snavely *et al.* [34], a well collimated high-energy proton beam was observed normal to the rear surface of thin foil. There have been both experimental and numerical efforts [46, 65] to explain the acceleration energetic protons from the target's rear surface. After the so-called TNSA concept was introduced by Hatchett *et al.*[65], the TNSA mechanism was extensively investigated and settled as a robust way to explain the ion acceleration from an intense laser-solid interaction [48, 50, 66–68].

Other ion acceleration mechanisms

While TNSA is often the dominant acceleration mechanism in typical laser-plasma interactions, and the most extensively studied, there are other mechanisms noted in the literature. *Radiation pressure acceleration* occurs under certain conditions because the light carries momentum and transfers momentum to the medium upon reflection, resulting in acceleration of ions in the foil. [69–73]. In the case of a sufficiently thin target, the light penetrates the foil and heats electrons over the entire focal volume, generating a large longitudinal E-field localized at the target rear surface. Strong ion acceleration is achieved by the longitudinal E-field – a process known as the *breakout afterburner*. [74, 75]. As an ultra-intense laser evacuates electrons from thin foil targets, another mechanism known as *directed Coulomb explosion* can accelerate ions. [76].

2.3.6 Laser-based fusion neutron production

Neutron sources can be broadly grouped together in terms of the energy of emitted neutrons, fluxes, and the size of the source. The overall size of the whole device is not typically considered in the literature when comparing neutron sources. For practical

deployment, however, comparing the overall size of neutron sources is helpful to understand which may serve as future *portable* sources. Small neutron sources include spontaneous fission radioisotope sources such as Cf-252, or alpha-neutron sources such as AmBe or PuBe although these fission sources require radiation shielding and constantly emit neutrons. Medium sized neutron sources are light ion accelerators that generate neutrons by colliding light ions (hydrogen, deuterium, or tritium) with low-Z materials to generate neutrons through fusion or stripping reactions. Dense plasma focus [77, 78], plasma pinch and high-energy bremsstrahlung photo-neutron/photo-fission systems are also categorized as medium-sized sources. These device-based neutron sources are controllable, in that they may be turned on and off, and would be, therefore, more favorable candidates for a portable neutron source. Large neutron sources such as nuclear fission reactors / fusion systems or spallation sources can generate very high fluxes of neutrons ($> 10^{14}$ $\mathrm{n\,cm^{-2}\,s^{-1}}$) [79]. Compared to other neutron sources, laser-based neutron generation systems (i.e. laser-driven light-ion accelerator neutron source) are beneficial due to a number of reasons, including; less investment and operational cost [80, 81]; short pulse duration (less than a few nanoseconds); and compact size of the system.

In this thesis, we focus on laser-based neutron sources. Laser-based neutrons typically rely on a few specific fusion (or stripping) reactions. These accelerator driven fusion reactions proceed in two steps. First, a selected ion species is accelerated in a laser-target interaction. Second, the ions interact with other ions either in the same target or a secondary target to generate neutrons. Table 2.1 shows probable neutron-yielding nuclear fusion reactions having large cross sections (see Fig. 2.4). Light ions (D or T) are accelerated and collide with other low Z materials including (D or T) giving out neutrons.

The scheme using a secondary target is known as the "pitcher-catcher" method. The P-C method has been employed and successfully generated fast neutrons. By

Table 2.1 List of the most favorable neutron yielding fusion reactions [82]

Reactions		Results
${}_{1}^{2}\mathrm{D} + {}_{1}^{3}\mathrm{T}$	$\rightarrow$	${}_{2}^{4}\mathrm{He} + \mathrm{n}^{0}$
${}_{1}^{2}\mathrm{D} + {}_{1}^{2}\mathrm{D}$	$\rightarrow$	${}_{2}^{3}\mathrm{He} + \mathrm{n}^{0}$
${}_{1}^{3}\mathrm{T} + {}_{1}^{3}\mathrm{T}$	$\rightarrow$	${}_{2}^{4}\mathrm{He} + 2\,\mathrm{n}^{0}$
${}_{1}^{3}\mathrm{T} + {}_{2}^{3}\mathrm{He}$	$\rightarrow$	${}_{2}^{4}\mathrm{He} + \mathrm{p}^{+} + \mathrm{n}^{0}$
${}_{1}^{2}\mathrm{D} + {}_{3}^{6}\mathrm{Li}$	$\rightarrow$	${}_{2}^{3}\mathrm{He} + {}_{2}^{4}\mathrm{He}^{+}\mathrm{n}^{0}$
${}_{1}^{2}\mathrm{D} + {}_{3}^{6}\mathrm{Li}$	$\rightarrow$	${}_{4}^{7}\mathrm{Be} + \mathrm{n}^{0}$

introducing neutron generating targets or coating material, one can selectively accelerate the ions using the laser accelerator ("pitcher") and then choose fusion reactions yielding specific neutron energies. The P-C method for neutron generation and detection has also been used for revealing the origin of the ions in TNSA, i.e. from either the front or rear side of targets [53, 65, 84–87]. Neutron generation results without the P-C arrangement, i.e., no secondary target, have also been reported [53, 86, 88, 89]. For comparison, previous experimental results on laser-produced neutron sources are reviewed in Table 2.2. As shown in the table, most of high neutron flux results were

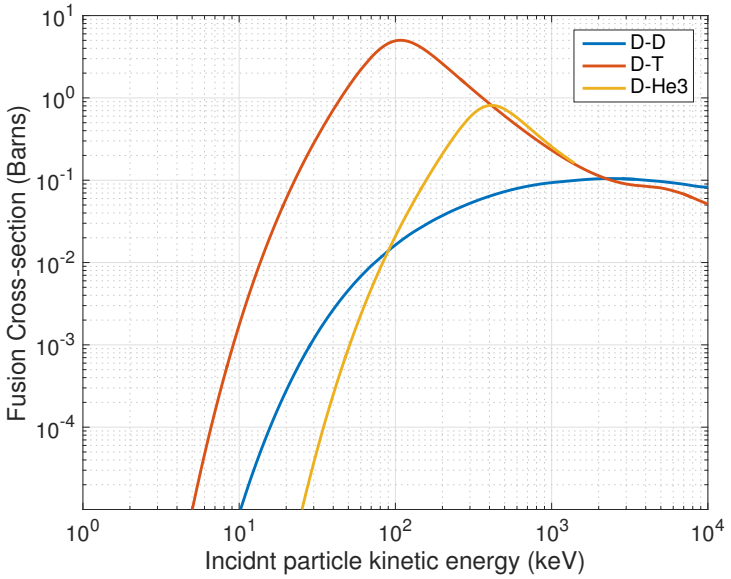

Figure 2.4 Cross-sections of nuclear fusion reactions as function of kinetic energy of incident deuteron [83].

obtained from high pulse energy (> 1 J) pulsed laser systems and very low repetition-rate.

Table 2.2 Laser-based neutron sources

Publications	Neutron yield (n/sr/shot)	Reaction	Energy (J)	Intensity (Wcm^{-2})
Roth *et al.* [57]	1×10^{10}	$^{9}\mathrm{Be(d,n)}^{10}\mathrm{B}$	80	(1–10) $\times 10^{20}$
Higginson *et al.* [90]	8×10^{8}	$^{7}\mathrm{Li(d,n)}^{8}\mathrm{Be}$	360	2×10^{19}
Lancaster *et al.* [91]	4×10^{8}	$^{7}\mathrm{Li(p,n)}^{7}\mathrm{Be}$	69	3×10^{19}
Higginson *et al.* [92]	1×10^{8}	$^{7}\mathrm{Li(p,n)}^{7}\mathrm{Be}$	140	1×10^{20}
Zulick *et al.* [93]	1×10^{7}	$^{7}\mathrm{Li(p,n)}^{7}\mathrm{Be}$	1.1	2×10^{21}
Norreys *et al.* [94]	7×10^{7}	$^{2}\mathrm{d(d,n)}^{3}\mathrm{He}$	20	1×10^{19}
Fritzler *et al.* [85]	1×10^{6}	$^{2}\mathrm{d(d,n)}^{3}\mathrm{He}$	62	2×10^{19}
Zulick *et al.* [93]	1×10^{5}	$^{2}\mathrm{d(d,n)}^{3}\mathrm{He}$	1.1	2×10^{21}
Willingale *et al.* [53]	5×10^{4}	$^{2}\mathrm{d(d,n)}^{3}\mathrm{He}$	6	(1–3) $\times 10^{19}$
Ditmire *et al.* [88]	8×10^{2}	$^{2}\mathrm{d(d,n)}^{3}\mathrm{He}$	0.12	2×10^{16}
Ter-Avetisyan *et al.* [89]	5×10^{2}	$^{2}\mathrm{d(d,n)}^{3}\mathrm{He}$	0.6	1×10^{19}
Pretzler *et al.* [95]	20	$^{2}\mathrm{d(d,n)}^{3}\mathrm{He}$	0.2	1×10^{18}

Among different neutron-yielding fusion reactions, the following two reactions (Eqns. 2.26a and 2.26b) are commonly used for not only commercial neutron sources, but also laser-based neutron sources. Particularly, the DD reaction is more commonly used for generating neutrons because tritium requires more regulations.

$$^{2}_{1}\mathrm{D} + ^{2}_{1}\mathrm{D} \longrightarrow ^{3}_{2}\mathrm{He} + n\,(2.45\,\mathrm{MeV}) \tag{2.26a}$$

$$^{2}_{1}\mathrm{D} + ^{3}_{1}\mathrm{T} \longrightarrow ^{4}_{2}\mathrm{He} + n\,(14.1\,\mathrm{MeV}) \tag{2.26b}$$

Also, using the DD reaction can eliminate an extra catcher target setup by introducing deuterium cluster as primary target [88, 96, 97]. Here, in this thesis, a deuterated water jet (D_2O) was tested to generate neutrons with no secondary target alignment and no cluster generation systems at all. This will be discussed more in Chapter IV.

2.3.7 THz pulse generation using laser interactions

Because of the interesting characteristics and possible applications of THz radiation, there have been many efforts to generate THz radiation. There are two

approaches to generate THz radiation; an electronic approach (lower frequency) and an optical/photonic source (higher frequency). Here, laser-based (optical/photonic approach) sources will be reviewed.

Photoconductive switches

A photoconductive switch method is the most widely used method for the generation of a THz pulses, which was introduced by Auston [98]. A semiconductor (GaAs or silicon on sapphire) device is biased with a voltage of 10 to 50 V, generating a few kVcm^{-1} E-field between the switch. When a laser pulse irradiates the biased gap (an order of 10μm), free charge carriers are liberated and accelerated by the bias field. A sub-picosecond, single cycle of THz pulse is generated during the acceleration of the free carrier inducing polarization change. The THz field strength is proportional to the second derivative of polarization ($\mathbf{P}$) with respect to time.

$$E_{THz} \propto \frac{d^2\mathbf{P}}{dt^2} \tag{2.27}$$

The frequency of the emitted THz pulse is determined by the input laser pulse duration and device materials. The band gap of the materials should be smaller than the photon energy of the laser (e.g., GaAs: 1.42 eV, Ti:Sapphire laser: 1.55 eV). Laser pulse duration and the material's intrinsic carrier rise time govern the rise time of the transient current inside to switch the device. For a 4 μJ laser pulse, THz fields up to 36 kV cm^{-1} at repetition rates of 250 kHz were reported [99], with the device biased at 100 kV cm^{-1}. This method can generate THz from relatively low laser fluences, but due to strong saturation of the laser pulses, scaling to THz energies above the μJ level is generally limited.

Optical rectification

Optical rectification is a nonlinear optical process that generates a quasi-DC polarization when an intense laser propagates through a non-linear medium (with $\chi^{(2)}$). For a slow-varying envelope pulse, the quasi-DC polarization is very small. When the ultrashort pulse changes, however, the DC component varies rapidly, radiating a single-cycle pulse with a broad spectrum. For an input pulse of 100 fs, the resulting radiation frequency would be 10 THz or higher. As an interacting medium, CdTe and DAST is commonly used for room temperature operation, and $LiNbO_3$ is also used with a cooling system. The highest THz pulse energies have been generated using a tilted-pulse-front pumping technique with $LiNbO_3$ [100].

THz from laser-plasma interactions

To obtain very short, single-cycle THz pulses, nonlinear processes in gas plasma can be used. Unlike other semiconductor-based methods, plasma is a damage-free THz emitter and there is no absorption due to the material itself. This method can generate an extremely broad bandwidth of THz pulse, which is limited only by the laser pulse duration. For these reasons, THz radiation in laser-induce plasma method is investigated in this thesis. (Chapter V)

After Hamster *et al.* [101] reported coherent THz generation in 1993, a second harmonic field mixing technique was proposed [102], and currently up to a few μJ of THz pulses have been generated with more than 10^{-4} pump-to-THz conversion efficiency [103]. As well as the high energy of the THz pulse, ultra-broadband THz (up to 100 THz) generation was demonstrated using 19 fs of pulse with BBO crystal angle optimization [104].

CHAPTER III

Methods

This chapter includes a description of the two laser systems used in the experiments in this thesis; 1) Neutron generation, 2) laser-based SNM detection method. The experimental configurations and diagnostics used in this thesis are also described.

3.1 Laser systems

3.1.1 The λ^3 Laser system

Experiments discussed in Chapter IV, and Chapter V were performed using the Relativistic Lambda-Cubed (λ^3) laser system at the Center for Ultrafast Optical Science of the University of Michigan. The λ^3 laser system is a Ti:Sapphire CPA laser and produces 35 fs pulses of 800 nm light at the repetition rate of ½ kHz. The laser system has an Amplified Spontaneous Emission (ASE) intensity contrast of $\sim 10^8$ around 1 ns before the main pulse. It should be noted that the ASE including *prepulse*-pedestal was able to be controlled by the user to examine different plasma characteristics for the neutron generation experiment. A diagram of the λ^3 laser system is shown in Fig. 3.1. A 12 fs pulses are generated from a FemtoLaser oscillator and each pulse goes through an acousto-optic programmable dispersive filter (AOPDF) called a "Dazzler". The Dazzler determines the spectral phase and amplitude of laser pulses. After the Dazzler, pulses are stretched up to 220 ps and

amplified to the few mJ level through a cryogenically cooled regenerative amplifier (Regen). From the Regen cavity, laser pulse undergoes a pulse "cleaning" process in a Pockels cell and is then passed through a 3-pass amplifier. The stretched and cleaned pulse is amplified up to 28 mJ and compressed to 30 fs. This final output pulse has up to 18 mJ of energy.

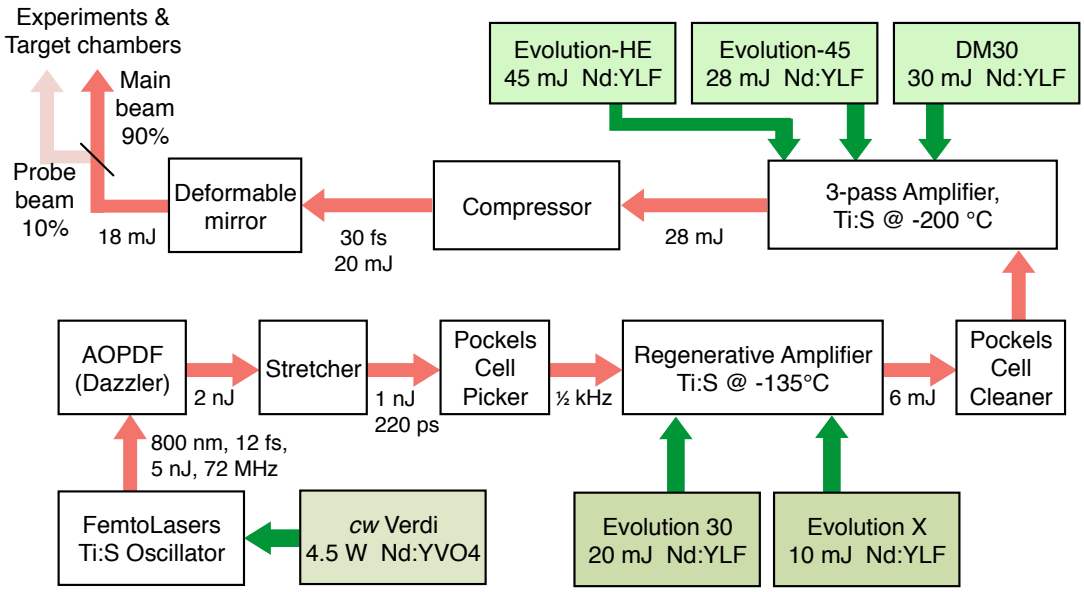

Figure 3.1 A basic schematic of the λ^3 laser system. Depending required beam energies for experiment, user can adjust final energy of the pulse. Image is adapted from Ref. [105]

Pulse duration measurement

To measure the pulse duration of the λ^3 laser, Frequency Resolved Optical Gating (FROG)[106] and 3^{rd} order auto-correlation techniques can be used. The FROG can *completely* characterize ultrashort ($\sim$ fs) pulses, giving not only pulse energy or duration, but also the optical spectrum with the frequency-dependent spectral phase. The information can be retrieved from an autocorrelation trace using the ultrashort pulse itself as a probe. Compared to an intensity correlation technique, the FROG does not require any information of the pulse to be measured. Among various beam

geometries of FROG, SHG-FROG is the most common and sensitive one, and a diagram is shown on Fig. 3.2.

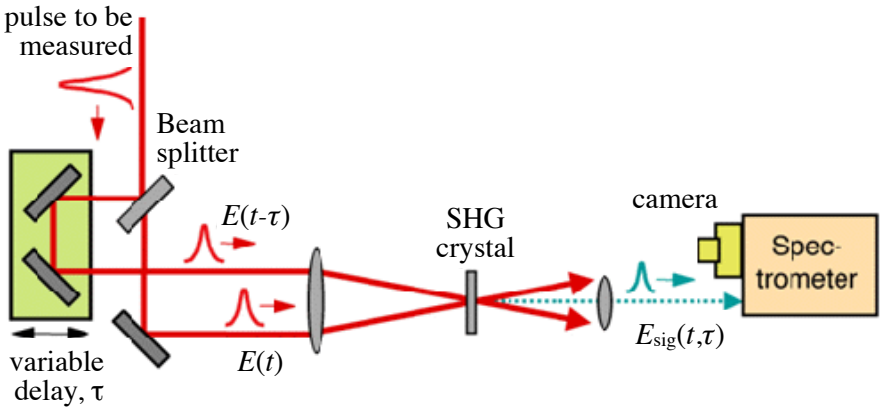

Figure 3.2 Basic principle of operation of SHG-FROG. Figure courtesy of `http://www.swampoptics.com/assets/tutorials-frog-2015.pdf`.

In SHG-FROG, the corresponding spectrogram signal (also called a FROG trace) is given by

$$I_{\mathrm{SHG-FROG}}(\omega,\tau) = \left| \int_{-\infty}^{\infty} E(t)E(t-\tau)\exp(-i\omega t)dt \right|^2 \tag{3.1}$$

From the measured FROG trace, the time-dependent electric field is reconstructed using an iterative algorithm similar to a two-dimensional phase-retrieval problem. Due to a symmetry with respect to the time domain on the trace, FROG cannot provide a direction of the time.

The pulse duration measurement in this thesis (Chapter IV and Chapter V) was performed using a commercial single-shot SHG-FROG device (SwampOptics model 8-9-thin-USB). The device can measure the laser pulse width a range from 10 fs to 100 fs. Thereby, a 3rd order autocorrelator (Amplitude Technologies, BONSAI) was employed for extend laser pulses longer than 100 fs.

3.1.2 Nd:YAG laser system

For the SNM detection experiment (Chapter VI), a commercial Q-switched Nd:YAG laser system was used (Continuum Surelite II). The Nd:YAG is a four-level gain medium and, is pumped by a lamp (It also can be pumped by a diode, but the model used in this experiment employs a flash lamp). The gain medium absorbs mainly in the 800 nm region and emits 1064 nm laser light. Other harmonics can be generated by frequency multiplications.

The laser used in the experiment emits light with a wavelength of 1064 nm operating at 10 Hz. The pulse energy is up to 400 mJ and its duration is 7 ns. A collimated 7 mm diameter beam is generated from the laser output port and it was expanded and refocused to employ a deformable mirror for optimization of the beam spatial characteristics. The spatially modified beam was characterized by a beam profiler (Thorlabs BC106-VIS Beam Profiler). To protect the Charge Coupled Device (CCD) camera of the beam profiler, a combination of neutral density filters (10 dB to 40 dB) was placed on the entrance to the profiler. The profile measurement will be shown in Chapter VI.

3.2 Radiation diagnostics

When an ultra-intense laser pulse interacts with matter, short bursts of radiation and charged and/or neutral particles are generated which can activate surrounding materials, such as chamber walls and optical components, resulting in secondary radiation. This radiation can scale with the strength of the interaction that occurs, i.e., the strength or efficiency of the laser-based radiation source. Radiation from laser-matter interactions can be measured by various detectors. For instance, X-ray diodes and Photo-Multiplier Tubes (PMT) detectors measure bremsstrahlung photons produced by accelerated electrons during the interaction. From the measured signal,

the laser focal spot position can be optimized by scanning through target position and maximizing the measured signals.

In this thesis, various detectors were employed to measure the photons and other charged/neutral particles. Among these detectors, some of the detectors, such as a Allyl Diglycol Carbonate or Columbia Resin 39 (CR39), require a post-processing procedure to reveal the actual dose of radiation (ion flux), but *relatively* fast detectors (e.g. Cadmium Telluride (CdTe) X-ray diodes, and pyroelectric detectors) provide signals without an extra procedure. When the signal is accompanied by an optimization algorithm and high repetition-rate laser system, it can be used for optimizing not only the laser focal spot position, but also a particular signal. For instance, the voltage output from a pyroelectric detector and plasma spectral ratios are used for optimizing deformable mirror shapes, as in Chapter V and Chapter VI, respectively. In this chapter, several radiation diagnostics used in this thesis are described.

3.2.1 CR39

CR39 is the most common Solid-State Nuclear Track Detector (SSNTD) used to detect energetic nuclear particles. The main advantages of CR39 over other radiation detectors are its low cost and the simple configuration of the detector. Since the CR39 detector was invented, this simple plastic detector has been widely used for scientific research satisfying following requirements as a high resolution polymer detector [107, 108];

- high homogeneity and isotropy
- high radiation sensitivity
- high optical transparency and uniformity
- having a non-solvent chemical etchant

When energetic ions travel through target materials, ions lose their energy and stop, which result in *Bragg curve* (See Fig. 3.3).

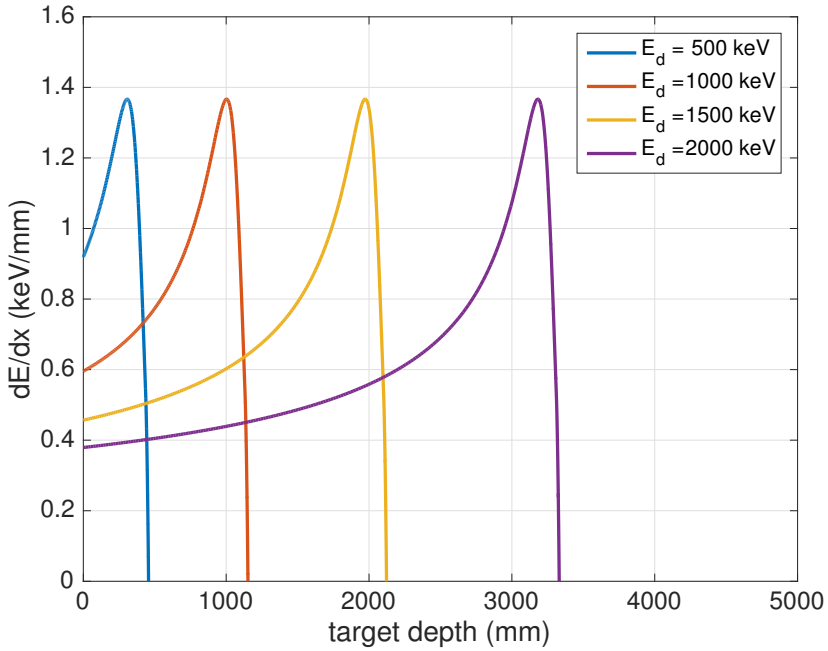

Figure 3.3 The Bragg curves for deuterons in 15 torr of D_2O vapor. It shows a *Bragg peak* on the right side, which is skewed to the left.

Through a CR39 detector, energetic ions deposit their energy in the Bragg peak, breaking chemical bonds. The nm-scale *damaged tracks* have faster etching rate as exposed to the etchant (e.g. NaOH) than the undamaged-bulk materials. Due to different etching rates of damaged/undamaged area, the tracks reveal as pits in the CR39 as shown in Fig. 3.4. The size and shape of the pits provide information about the particles such as mass, energy, and even its direction of incidence. For example, if the particles enter the CR39 front surface at normal incidence, circular pits would be observed. Otherwise, elliptical pits would appear. The most interesting information from the CR39 are incident energy of the ion, flux and/or its divergence. In order to determine ion energy, one can develop the CR39 with well controlled etching conditions (temperature and time), thereby pit size leads to the energy distribution.

However, a filter stack can provide more robust way to determine ion energy. The filter stack sets an energy threshold for incident ions to the CR39. Typically, a 12.5 μm thick of Al, or a 14 μm thick of Mylar can stop 1 MeV of deuterons [109].

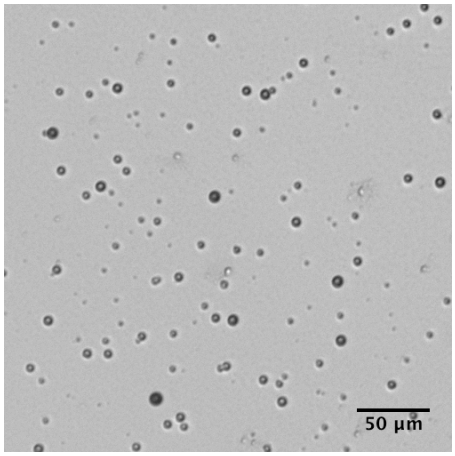

Figure 3.4 A microscope image of CR-39 exposed to deuterons after one hour etching process at 90°.

Ion flux counting

ImageJ software is used for evaluate ion fluxes. The software is an open source image processing program designed for scientific multidimensional images (`http://imagej.net/` or `https://imagej.nih.gov/ij/`). From macroscopic images of the CR39 samples, a few captured images of regions of interest (ROI) were processed using ImageJ. The ion pit counting process for each captured ROI is described as follows. First, the captured image was converted to a 16-bit greyscale format and thereby, the greyscale image went through a treshold value filter to be converted to a binary image. A built-in ImageJ function ("Analyze particles") was used to count final ion pits. Here, one can reject false ion pits by defining "*particles*" with a size (area) and a low circularity. Figure. 3.5 shows ion counting result. Left of the image shows raw captured ROI image of a CR39 sample exposed to deuteron ions. A total of 161 pits were identified from the sample images. However, the identified pit counting

results could be underestimated the actual ion fluxes by the particle define criteria. When multiple ions are deposited on adjacent areas, ion pits could be bigger than defined size criterion, or summed ion pit shape could lose circularity. Examples of rejected correct ion pits by the these reasons are shown in Fig. 3.6. In order to reduce statistical errors, the same ion counting process was conducted for the different ROIs from the same CR39 sample.

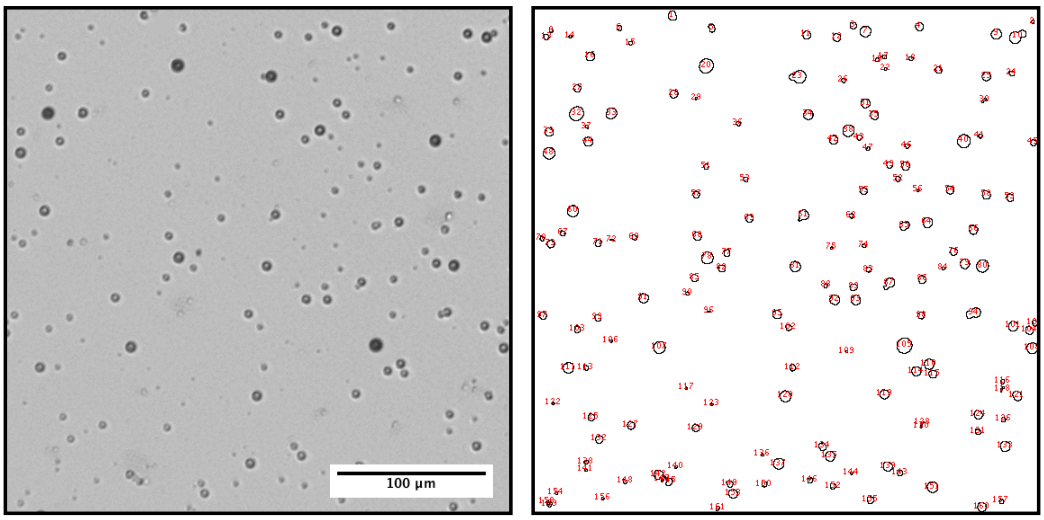

Figure 3.5 Ion pit counting result using ImageJ software. (Left) Captured ROI image of a CR39 sample exposed to deuteron ions. (Right) Counted ion pits using ImageJ built-in function.

Compared to other radiation detection methods, CR39 requires time-consuming post-processing (etching and counting) which limits number of shots. Even though these drawbacks of the CR39 are not suitable for the high repetition rate laser system such as λ^3, CR39 was still valuable measurement tools for an ion diagnostic due to its small dimensions that could be located anywhere inside the experimental chamber.

In this thesis, the CR39 ion detection method was used to measure absolute deuteron flux (Chapter IV).

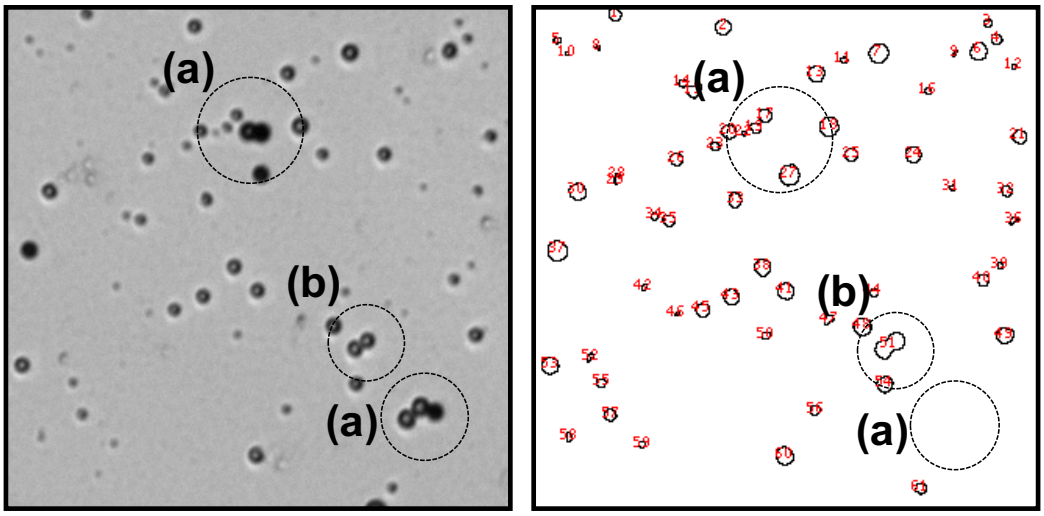

Figure 3.6 False ion counting by multiple hits. (a) Overlapped ion pits are rejected by the circularity filter. (b) Two adjacent ion pits are considered a single ion pit. These fault rejection could underestimate the ion counting.

3.2.2 Neutron Time-of-Flight measurement

In contrast to other particles (ions, and electrons), neutrons rarely interact with materials due to its zero-charge. Charged particles like protons or other light ions only can penetrate a material into a few micron depositing its energy at a Bragg peak, however, neutrons could pass material much longer ($\sim$ few cm) without losing their energy. Thus, to detect neutrons, different types of diagnostics are required. One possible neutron detection method is to consider nuclear reactions taking place or to track the resulting charged particles. For example, ^{3}He proportional detector detects neutron by $^3\mathrm{He}(\mathrm{n},\mathrm{p})^3\mathrm{H}$ reaction and BF_3 detector and Boron lined detector is using the boron reaction ($^{10}\mathrm{B}(\mathrm{n},\alpha)^7\mathrm{Li}$). However, these reactions have peak cross sections near the thermal neutron energy range, thus the detectors are inefficient for fast neutron detection. Also, ^{3}He and BF_3 require careful handling due to its limited access and highly toxic characteristics, respectively. Therefore, another neutron detection method is using energetic ions from elastic collision between neutrons and light ions, instead of initiating nuclear reactions. Recoiled ions can be easily detected due to

their charge and its energy, E_{Rmax} is

$$E_{Rmax} = \frac{4A}{(1+A)^2} E_n \tag{3.2}$$

where E_n is the initial energy of the neutron, and A is the atomic mass. To maximize energy transfer from the neutron, hydrogen-rich organic scintillators (ELJIN, EJ-204) were used for the neutron experiment in Chapter IV. When neutrons transfer the energy to the scintillator, the molecules of the scintillator are excited. The excited molecules decay with a time constant τ_d emitting light which corresponds to energy levels. For better detection efficiency, the scintillator is often coupled to a PMT (Hamamatsu, H2431-50). The light from the scintillator is collected and converted to photoelectrons at the photocathode of the PMT. Through dynode stages of the PMT, photoelectrons are multiplied and an oscilloscope records the time-voltage signals (see Fig. 3.7).

Neutron energy can be measured by determining the neutron speed from the Time-of-Flight (ToF) analysis. The speed of a neutron can be calculated by the required time for the particle from time of creation to the known-distance detector. Note that this time includes scintillator and PMT response time. The kinetic energy of relativistic neutron is given by

$$E_k = (\gamma - 1) m_0 c^2 \tag{3.3}$$

Where, $\gamma = (1 - \frac{v_n^2}{c^2})^{-1/2}$. For the fast neutrons, the neutron velocity can be considered relatively slow, ($v \ll c$), and the γ in Eqn. 3.3 can be extended and simplified by the binomial expansion, and the Eqn. 3.3 can be written by

$$E_k = \left[\left(1 + \frac{v_n^2}{2c^2} \right) - 1 \right] m_0 c^2 = \frac{m_0 v_n^2}{2} \ , \tag{3.4}$$

Figure 3.7 EJ-204 organic scintillator and photo-multiplier. To block room light, scintillator–PMT assembly was sealed with black tape. The assembly was surrounded by 5cm-thick lead bricks and borated plastics and only front side was opened and directed to the target allowing signals from an interaction to be recorded

which is the classical kinetic energy of particle. In Fig. 3.8, the neutron velocity from two calculations is plotted within a plausible neutron energy range. The experiment in this thesis, we ignited D–D fusion reaction yielding 2.45 MeV neutrons. For the 2.45 MeV neutron, relativistic factor γ is 1.0026 and the difference from two calculations is only 0.2%. This leads to 0.1 ns error for 10 m distance. But, in this thesis, relativistic calculation was applied for accuracy.

For as given distance to the detector (D), and the time delay between X-ray signal arrival and neutron arrival ($\delta_{x,n}$), the neutron velocity (v_n), is given by

$$v_n = \frac{D}{D/c + \delta_{x,n}} \tag{3.5}$$

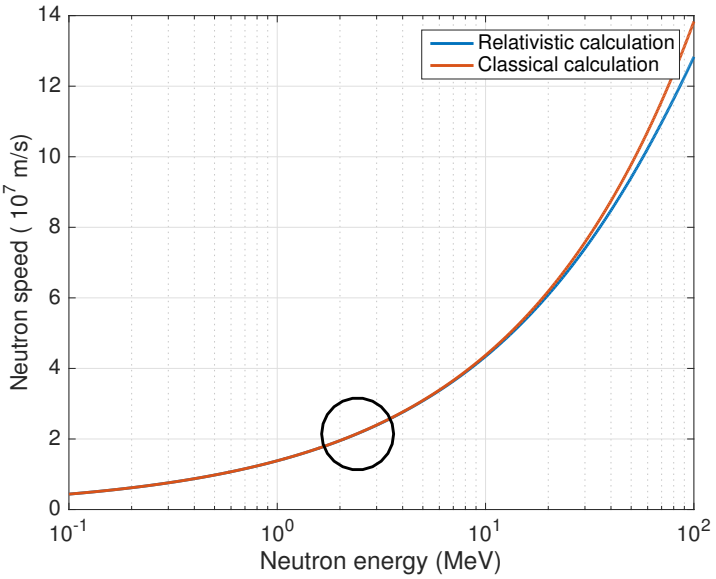

Figure 3.8 Neutron velocity from relativistic/classical calculation. For the 2.45 MeV of D–D fusion neutrons (inside a drawn circle), classical calculation error is negligible.

From a measured time delay ($\delta_{x,n}$) and Eqn. 3.3, the neutron energy can be obtained.

Figure 3.9 shows an actual oscilloscope trace from the EJ-204 Scintillator with PMT assembly (biased at -2.5 kV). The laser interacts with a D_2O target at $t = 0$ sec (the time was calibrated with a laser oscillator reference timing.) and after a certain time delay, (D/c, $\delta_{x,n}$), the X-rays and neutrons arrive at the detector.

When D–D fusion takes place, the fusion reaction has two branches as follows:

$$^{2}_{1}\mathrm{D} + {}^{2}_{1}\mathrm{D} \longrightarrow {}^{3}_{2}\mathrm{He} + n\,(2.45\,\mathrm{MeV}) \tag{3.6a}$$

$$^{2}_{1}\mathrm{D} + {}^{2}_{1}\mathrm{D} \longrightarrow {}^{3}_{1}\mathrm{T} + \mathrm{p}^{+}(3.02\,\mathrm{MeV}) \tag{3.6b}$$

These two reactions occur with a probability of 50 to 50. Eqn. 3.6a yields 2.45 MeV neutrons, which can be detected by the neutron ToF measurement. In this thesis, neutron ToF measurements were reported using two identical plastic scintillators with PMT assemblies. The detectors were located at 2 m and 3.5 m away from the chamber.

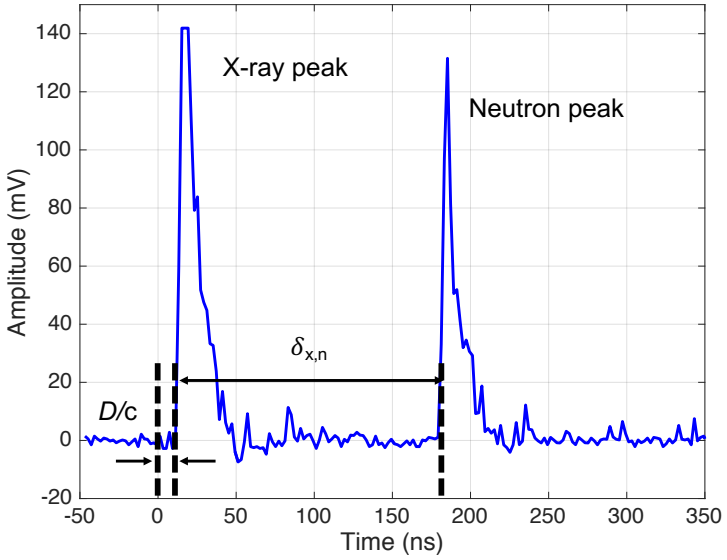

Figure 3.9 nToF trace example. The trace is recorded by an oscilloscope, X-rays and neutrons generate each peak after certain time delay. When the laser pulse interacts with D_2O target, generated X-rays travel at the speed of light and record the first peak at the D/c. Because neutrons generated from D–D fusion have an about 10% of light speed, the neutron peak is delayed by $\delta_{x,n}$. Amplitudes of those peaks are not correctly scaled due to a saturation of X-ray peak. Note that the X-rays peaks are usually modified due to signal saturation problem.

Of course, neutron can be detected by the CR39 from the recoiled particle left track after proper etching process (Sec. 3.2.1); however, the neutron detection efficiency for DD (2.45 MeV) neutrons on CR39 is very low $(6.0 \pm 0.7) \times 10^{-5}$ under similar CR39 etch conditions [110], which is negligible under experimental circumstance in this thesis.

3.2.3 Neutron bubble detector

Another technique for detecting neutrons involves the use of a neutron bubble detector. After the invention of the bubble chamber by Glaser in 1952 [111], methods using superheated liquid emulsions have been intensively studied. In 1979, the superheated emulsion neutron detector was invented by Apfel [112], since then, research and applications using neutron bubble detectors have been widespread [113–124].

Neutron bubble detectors are convenience and reusable, in contrast to the nToF or CR39. The bubble detection does not required any other subsystem or post-process other than bubble counting. In addition, the vaporized bubble is reversible by simply applying pressure with a twist cap on the detector. Within 30 minutes, the bubble shrinks back to micro-bubble phase and the detector is ready to use again. The bubble detector has the following advantages: 1) insensitivity to both X-rays and electron interactions, 2) for the model PD-BND employed in the experiment, a flat response across a broad energy range (0.3 MeV to 10 MeV) [125] and linear bubble generation with respect to neutron flux [126]. Based on these characteristics and the given calibration factor, the neutron flux from the laser-based source can be estimated.

The detector contains superheated (or over-extended) halocarbon and/or hydrocarbon droplets (Fig. 3.10). These droplets are uniformly placed into immiscible host fluids (e.g. aqueous gel [112] or polymeric gel [113]). Because the droplets are in a meta-stable state, they easily vaporize in response to a with a small energy deposition transferred from charged particles. In order to detect the neutrons, moderate levels of superheated halocarbons can be used because they are nucleated only by energetic heavy ions from the fast neutron interaction.

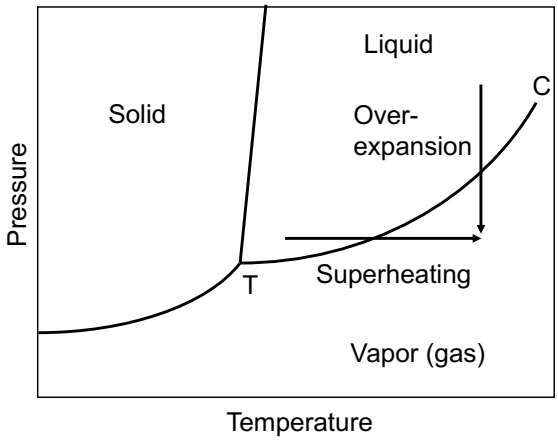

Figure 3.10 Phase diagram of a common material

The general process of bubble generation and required minimum energy for de-

tection can be estimated by thermal fluid dynamics with some assumptions: 1) a macroscopic fluid equation describes the host fluid behavior, 2) the energy is deposited instantly and uniformly. To generate the bubble, the orbital electrons of the liquid composition atoms are knocked out by obtaining energy from recoiled ions with energy of E_k (Eqn. 3.3), leading to liquid vaporization. The critical radius of the bubble is given by

$$R_c = \frac{2\gamma(T)}{P_v(T) - P_0} = \frac{2\gamma(T)}{\Delta P(T)} \tag{3.7}$$

where, γ(T) is the surface tension of the liquid at temperature T, and P_v(T), and P_0 are the pressure of the vapor in the cavity, and the externally applied pressure, respectively. The minimum possible energy, necessary to nucleate a bubble (W_o) is given by [127]

$$W_o = \frac{16\pi\gamma^3(T)}{3(\Delta P(T))^2} \times [1 + \frac{2\Delta H}{\Delta P(T)} - 3\frac{T}{\gamma(T)}\frac{d\gamma(T)}{dT}] \tag{3.8}$$

where, ΔH is the latent vaporization heat of the fluid.

Neutron bubble detector calibration

The bubble detectors were independently calibrated for DD neutrons using a commercial neutron generator at the Neutron Science Laboratory at the University of Michigan (Thermo Scientific, MP-320). The generator yields 1×10^6 neutrons per second in the DD neutron-generation mode. The same four bubble detectors were attached onto the neutron generator tube surface (see Fig. 3.11).

The MP320 neutron generator builds up the voltage to draw the beam current. For ideal D−D neutron operation, voltage and beam current are required to be set as 80 kA and 60 μA, respectively. When the beam current reaches 60μA, the generator emits its known neutron flux (10^6 neutron/sec) into 4π direction. For different exposure times to the generator (from 5 sec to 30 sec), the detectors formed bubbles and

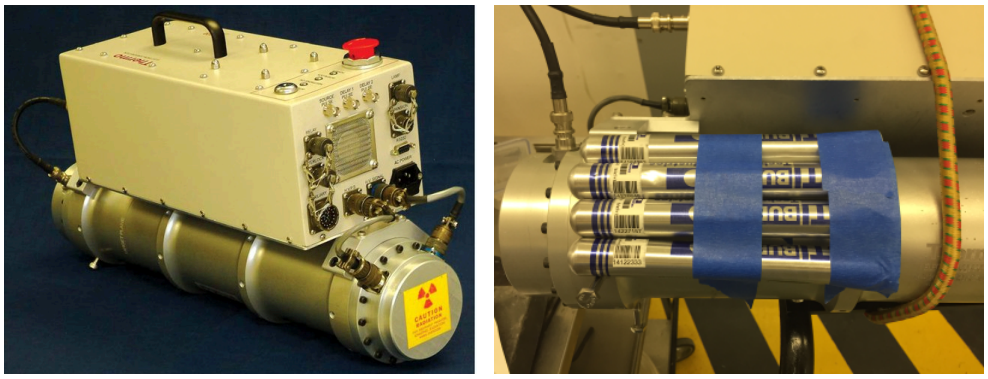

Figure 3.11 (Right) MP320 Neutron generator. (dimension ϕ12.07 cm $\times$ L 57.15 cm). Image is from [128]. (Left) The bubble detectors are located at the generator external surface (6cm from the generator axis).

the results are tabulated and plotted on Table 3.1 and Fig. 3.12. Here, the exposure time represents the time duration while the beam current is above 60 μA. Before and after reaching 60 μA, the generator yields fewer neutrons than the normal flux level (10^6 neutrons/sec), and it may interact with the detector and make bubbles. To compensate for the number of bubbles from the lower neutron flux, the '0'-second measurement was conducted and the measured bubble count (5 bubbles) was set as the y-intercept of the fitted curve in Fig. 3.12. From a fitted curve and a given geometry, the calibration factor for the bubble detector is 6900 neutrons per bubble.

Table 3.1 Neutron bubble detector calibration. 0-second represents that operation is stopped just after the current reaches nominal operating current (60μA).

Exposure time(sec)	# of bubbles	Exposure time(sec)	# of bubbles
0	5 $\pm$ 1	15	32 $\pm$ 0
5	20 $\pm$ 4.2	20	47.3 $\pm$ 4.6
10	23.8 $\pm$ 4.8	30	60 $\pm$ 0

3.2.4 Semiconductor-based radiation detectors for γ-rays

In order to detect radiation such as energetic charged particles and/or photons, various types of detectors can be used. The most widely used types of radiation

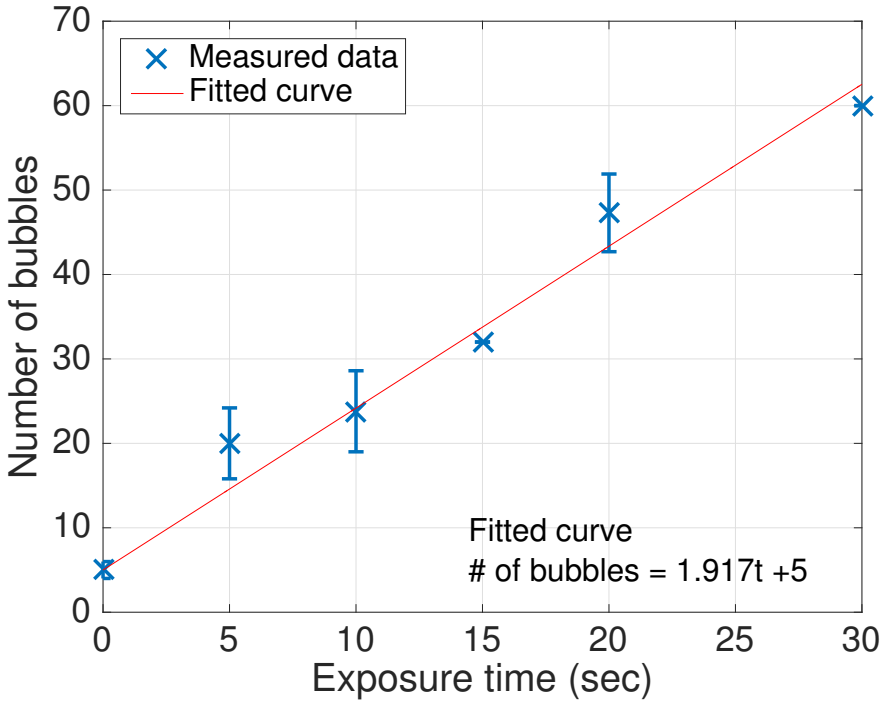

Figure 3.12 Neutron calibrations by MP320, The red line is a fitted curve with a slope 1.917 [bubble per second]. The y-intercept (5 bubbles) is from the 0-sec measurement, which counts the bubble from below the normal neutron flux. (10^6 neutron/s)

detectors are scintillators and gas-filled detectors. Scintillation-based detectors use light output signals from the excited molecules by the radiation. But the scintillation-based detector has relatively poor energy resolution because the final output signal is the result of a two-step process: 1) converting the incident radiation energy to light outputs, and 2) generating final electric signals from the light outputs, subsequently. Here, the energy required to produce a single information carrier (a photoelectron) is an order of 100 eV, yielding only a few thousand of carriers from typical radiation. This small number of carriers causes statistical fluctuations on the energy resolution and it cannot be improved because it is a inherent limitation of the scintillation detectors [129]. The gas-filled detector senses the direct ionization along the radiation track. By applying an electric field, the ionized positive ion and free electrons (ion pair) are collected at the electrode. The ion pair serves as an information carrier, the

total number of ion pairs is proportional to the radiation flux. The *W-value* is defined as energy dissipation per ion pair and is typically a few tens of eV. The gas detectors can yield more information carriers than scintillation-based detectors from the same energy of particle; however, for efficient detections, gas-filled detectors need to be bigger. The semiconductor type solid detector can satisfy both problems: the size of the detector and the number of information carriers. First, as the solid detector, a semiconductor has more than 1000 times greater density than that of a gas, enabling it to be a small size. Second, typically, it requires less than 2 eV for creating a single information carrier (*electron-hole pair*), which is called *bandgap* energy. For example, Ge has 0.67 eV of the bandgap energy and Si has 1.12 eV at 302 Kelvin, respectively. This low bandgap energy allows enough information carriers, resulting in a higher energy resolution. Some basic properties of common semiconductor materials are shown in Table 3.2.

Table 3.2 Properties of common semiconductor materials. Table is adapted from Ref. [129].

Material	Z-number	Density (g/cm^3)	Bandgap (eV)	Ionization Energy (eV per *e-h* pair)	Energy resolution (FWHM)	Ref.
Si (300 K)	14	2.33	1.12	3.61	n/a	[130]
(77 K)			1.16	3.76	400 eV at 60 keV	[130]
(77 K)					550 eV at 122 keV	[130]
Ge (77 K)	32	5.33	0.72	2.98	400 eV at 122 keV	[130]
					900 eV at 662 keV	[130]
					1300 eV at 1332 keV	[131]
CdTe (300 K)	48/52	6.06	1.52	4.43	1.7 keV at 60 keV	[132, 133]
					3.5 keV at 122 keV	[132]

Based on the photon energy, the detector materials interact with photons and the photon energy transfers to electrons in three different ways: *photoelectric absorption, Compton scattering*, and *pair production* (see Fig. 3.13). For lower energy photons ($\leq$ 100 keV), the photoelectric absorption is dominant. In the photoelectric absorption process, a photon disappears after an interaction with an absorber atom, and the photoelectron is liberated from its bound shells. The photoelectron has an energy

given by

$$E_{photo} = h\nu - E_b \tag{3.9}$$

where, E_b is the binding energy of the photoelectron at the original shell.

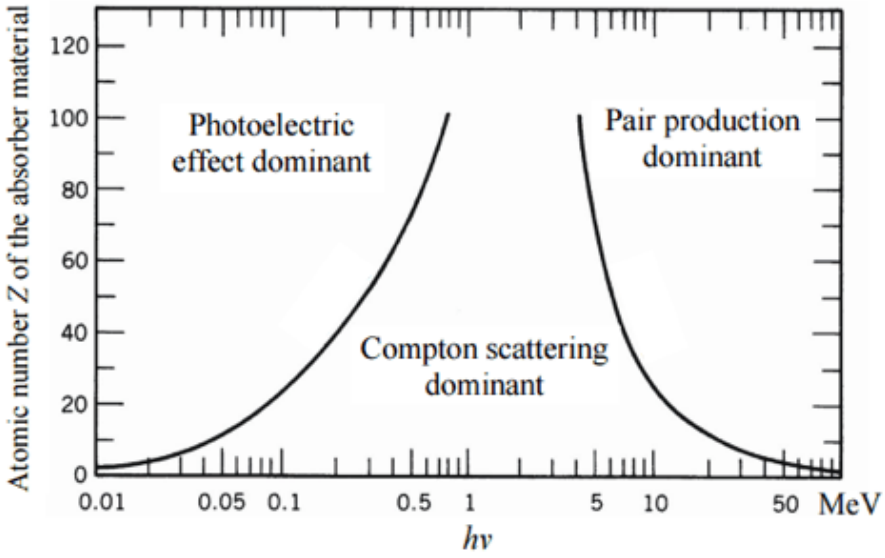

Figure 3.13 Photons (Gamma-rays) interact with matter via three different mechanisms: photoelectric effect, Compton scattering and pair production. Image is adapted from Ref. [134].

When the gamma-ray has more than twice the rest-mass energy of an electron (511 keV $\times$ 2), the pair production process is able to occur. In this process, the high energy photon disappears, creating an *positron-electron pair*. The positron loses its energy in the medium and will annihilate, then two photons are produced and emitted in opposite directions in the most common case. The other photon interaction mechanism is Compton scattering. As shown in Fig. 3.13, photons with a moderate level of energy ($\sim$ 1 MeV) undergo Compton scattering, which most commonly happens to radioisotope-generating photons. The incident photon with an initial energy $E = h\nu$ is scattered/deflected through an angle (θ) with respect to the original direction of the photon. The photon transfers its partial energy to a recoil electron and

the scattered photon will have an energy $E = h\nu'$. Before and after collisions, the energy and momentum conservation equations are valid, and with the initial energy ($E = h\nu$) and scattering angle (θ), scattered photon energy is given by [129]

$$h\nu' = \frac{h\nu}{1 + \frac{h\nu}{m_0c^2}(1 - cos\theta)} \tag{3.10}$$

where m_0c^2 represents the rest mass energy of the electron (511 keV).

High Purity Germanium Detector

HPGe is one of the semiconductor-based radiation detectors. From the view of manufacturing, it can be fabricated up to a few centimeters in size and it can absorb up to a few MeVs of gamma rays as a total absorption detector. The main benefit of the HPGe is great energy resolution. Because of the low bandgap energy (0.67 eV), an adequate number of the information carriers is achievable allowing for a great energy resolution. However, the low bandgap energy limits its operation. At room temperature, thermally excited electrons can cross the bandgap and induce a large leakage current. To suppress the leakage current, the HPGe detector must be cooled to operate without noise and produce high resolution-spectroscopic data. Typically, the detector-cryostat is inserted into a thermally insulated-dewar in which there is a reservoir of liquid nitrogen, and the detector temperature is kept ideally at 77 K, but no higher than 130 K, when the detector is operating. Figure 3.14 shows a common HPGe detector and its configuration.

Cadmium Telluride X-ray detector

CdTe consists of high-Z materials (48 and 52) with a relatively high bandgap energy (1.52 eV), which means that CdTe detector can operate at room temperature

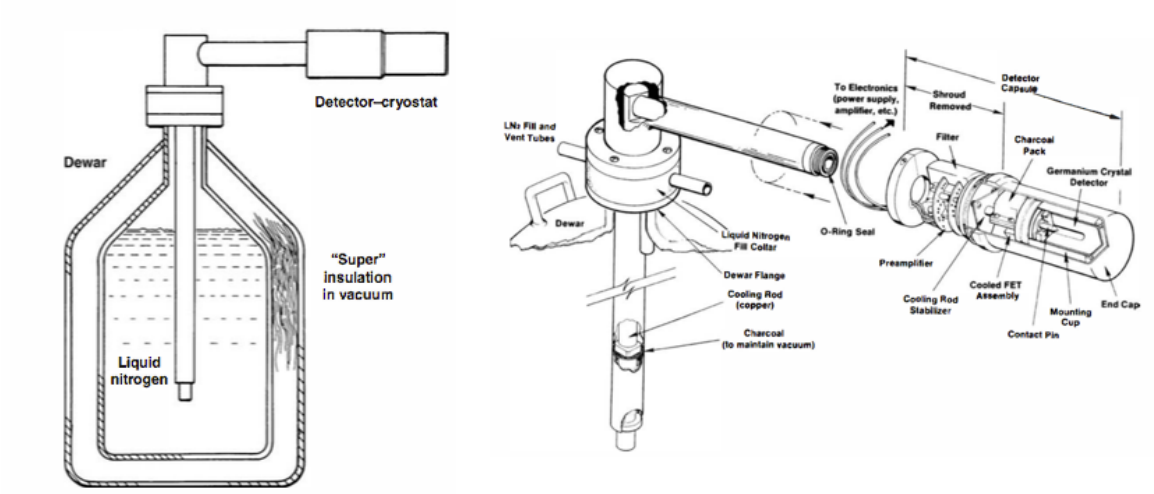

Figure 3.14 A diagram of HPGe detector with a liquid nitrogen dewar. The detector configuration is the horizontal configuration of the detector cryostat. Image is adapted from Ref. [129].

without suffering a leakage-current noise problem. In addition, it has higher probability of photoelectric absorption due to a higher-Z number. The probability is roughly approximated as $\sim Z^n$, where n varies between 4 and 5 depending on the gamma-ray energy level. From this approximation, CdTe would show 5 times higher probability than Ge, and >100 times higher than Si. Although CdTe detectors have lower energy resolution than Si- and Ge-based detectors under high energy gamma-ray conditions, the CdTe detector is favorable to a low-energy gamma-ray detection and an X-ray detection. If spectroscopic information is not required, CdTe detector can be operated with a simple pulse counting mode. Note that the CdTe detector in this thesis was used for a laser-target alignment indicator, for which it detected X-rays and photons from an intense laser-water interaction. Due to the high repetition rate of the λ^3 laser system, the detected signals were averaged over certain time durations, rather than using shot-to-shot values.

3.3 Adaptive optics

The technique called Adaptive Optics (AO) is used for sharpening blurred images by optical defects, including the atmospheric turbulence or optical aberrations from eyes. (Note that it should not be confused with the *active optics*, which is used for correcting mirror shapes to prevent large scale unwanted deformation by temperature variation, wind, and gravity.) While the AO was developed originally for a military purpose during the Cold War to track satellites, after the Cold War, it has been more widely used for astronomical applications [135–137]. Mostly, in the astronomical community, the technique is used for ground-based telescope systems to improve the imaging power of the system by correcting atmospheric distortions. The AO has been spread out to various fields for different applications including microscopy [138] and retinal imaging [139].

AO usually consists of two parts: 1) measuring a wavefront and 2) compensating for the wavefront using a device such as a deformable mirror or a liquid crystal array. However, the wavefront measuring process can be excluded if a user has specific purpose other than having a specific wavefront shape; for example, desiring the maximum optical intensity in the focused pulse. Because of the development of the optical manufacturing and coating technology, the deformable mirror-based adaptive optical system could be used for high power or high intensity laser experiments to achieve better optical performances such as focal spot and pulse duration [39, 140–142]. The DM was implemented into intensity laser systems and changed its shapes by an iterative algorithm to improve an output signal defined by users. In this thesis, the DM was used with two independent laser experiments (Chapter V and VI). These experiments used the DM to correct laser pulse wavefronts, and a Genetic Algorithm (GA) was used to generate test mirror shapes and calculate the Figure-of-Merit (FOM).

3.3.1 Deformable mirror

The deformable mirror (AOA Xinetics, DM37PMNS4) consists of a silver coated thin mirror sheet and 37 piezoelectric actuators arranged on a square grid (7-by-7) with 7 mm spacing between each actuator (see Fig. 3.15). The maximum mechanical stroke range of the actuators is 4 μm at 100 V, and, for these experiments, the voltage range is limited to 50 V in order to keep the device within safe operation. The mirror surface shape is controlled by the independently applied voltages on 37 actuators, and the voltages are randomly generated by the GA.

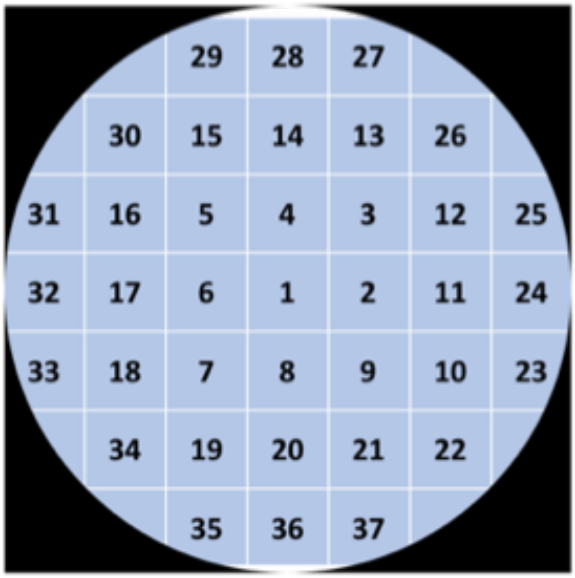

Figure 3.15 A configuration of the deformable mirror. The number represents the arrangement of the 37 electro-strictive actuators.

The final mirror shape is determined by a mirror response to the action of each single actuator (i.e., *influence function*). Therefore, with a phase-retrieval algorithm and the influence function, one can build the specific mirror shape.

3.3.2 Genetic algorithm

A genetic algorithm is a very effective way for solving complex systems with many variables. It is a type of evolutionary algorithm and finds an optimal solution by an

iterative method. It consists of a genetic representation of solution parametric space and a fitness function, which is called Figure-of-Merit to examine how the solutions work for a certain purpose. The GA starts with a one population (1st generation or *parent*). The initial population has a set of solutions and each solution is tested by user-defined FOM and then ranked. Only high-valued solution sets are allowed to become *parents* for the next generations. The selected parents generate a new population by a *crossover/mutation* process, and the new populations are tested by the FOM. This is the one full process of the GA. The loop will go on until a user stops the process. Figure 3.16 shows this process with a simple flow chart. In Fig. 3.16, only key steps of the GA are presented.

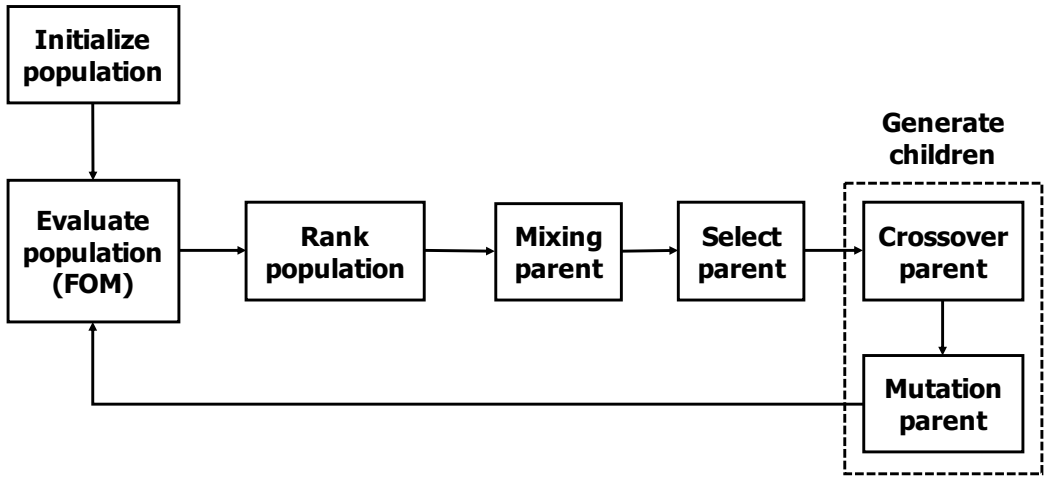

Figure 3.16 A basic flow chart of of the genetic algorithm process. The number of the initial population/parent/children would be changed by users.

The children generating process (inside the dotted line of the Fig. 3.16) makes genetically various pools for the children. One example of the children generating process is shown in Fig. 3.17. A mutation process swaps partial information of one parent to generate new children (Fig. 3.17 (a)), and in case of the crossover process, partial genes from the two different parents are combined to generate new offspring child solutions. (Fig. 3.17 (b)). These processes make various gene pools (sets of solution) to find the optimal solution. In addition to the children generating process,

the mixing process can make the algorithm more efficient. In case all the children are inferior to the prior generation (evaluated by the given FOM), the mixing process keeps some of the good genes from the prior generation.

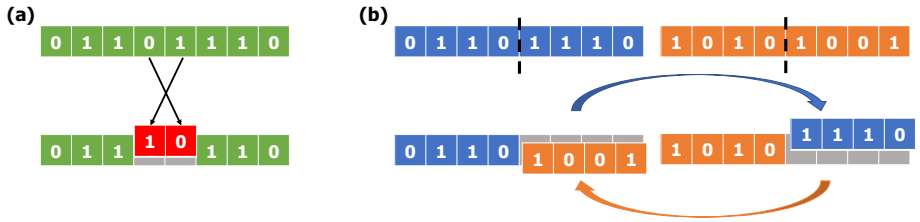

Figure 3.17 Examples of children generating process by (a) a mutation and (b) a crossover.

The GA process is written using LabVIEW program. The LabVIEW code includes not only the GA process but also the DM control subroutine. To operate the 37-actuator DM, GA has a set of 37 voltage values as the genetic genes. The corresponding mirror shapes modify beam shapes and a designated output signal is collected by a detector and the detected output signal is evaluated by FOM. A typical experimental setup with a DM and GA (operated by LabVIEW program) is shown in Fig. 3.18. The DM is located as close as possible to a focusing optics (OAP). Based on the experimental goals, an output signal, generated by each mirror shape, is collected by proper detector systems (e.g. photo-diode, CCD camera, spectrometer). The output signals are collected by a DAQ system, and are passed into GA to evaluate FOM. The GA evaluates FOM, and makes new sets of test voltages. Through a high voltage supplier to convert an input signal to actual voltage, the DM changes the mirror shape.

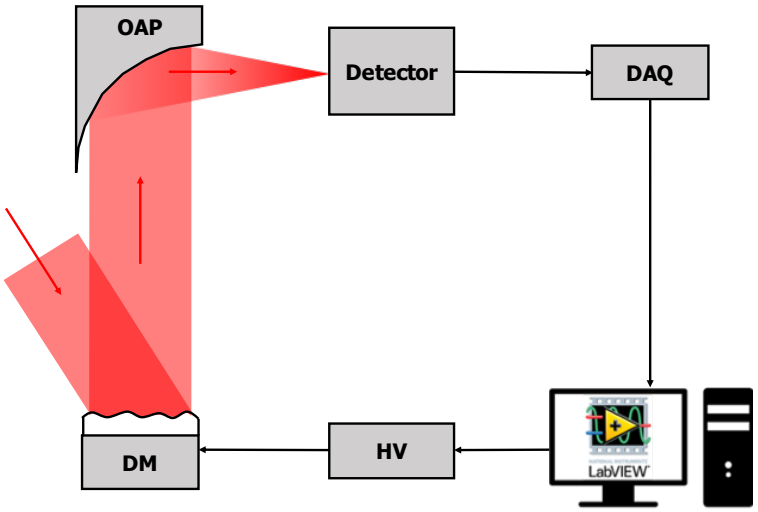

Figure 3.18 A diagram of an active feedback loop with the deformable mirror. DM: deformable mirror, HV: high-voltage supplier, OAP: off-axis parabolic mirror.

CHAPTER IV

Neutron generation

4.1 Introduction

An intense laser interaction with matter is capable of producing high energy particles that are typically produced by nuclear transitions, such as MeV photons, electrons and accelerated ions [143]. As an ion accelerator, laser-based techniques have several advantages including: (1) a compact system design, (2) low emittance, and (3) short burst duration. These characteristics of laser-based ion accelerators allow various possible applications in scientific, medical, and security areas. Since the first reports on proton acceleration from solid targets in 2000 [32–34], different solid target geometries such as different target thicknesses or micro-structured shape modifications have been tested to achieve higher energy ion acceleration [144–150].

Targets are typically fabricated with small dimensions to reduce the electron transfer into un-interacted target areas (a mass-limited target) [151–153]. In spite of the better energy conversion efficiency, such mass-limited target system only allow a few shots, requiring an alternative way for a high repetition rate laser-based ion accelerators. For instance, Henig *et al.* [154] held a microsphere target at the tip of a sub-micron capillary. While the target geometry increased maximum proton energy, the target geometry requires the whole target alignment for every single laser shot. Other thin solid target experiments employ a multiple mass-limited target that held

at grid [155] or fast target position device [156]. These configurations allow multiple shots without replacing a target for every shot, but still is not suitable for high repetition-rate lasers.

Regarding high repetition rate laser systems for ion accelerators, a thin tape or rotating disk was tested, providing a fresh target for every shot [157, 158]. However, these methods still suffer not only from hot electron transfer issue (compared to mass-limited targets), but also from debris inherent to the nature of solid targets. When the solid targets are irradiated by intense laser pulses, debris from target ablation contaminates optical components inside the chamber and thereby degrades optical performances. Instead of solid targets, *liquid*-type targets were proposed to resolve both debris and higher repetition application. By replacing conventional thin foil targets with clusters [85, 88, 96, 97] or liquid jet/droplets targets [86, 89, 159, 160], debris problem is reduced due to homogeneous or less *harmful* compositions of the target. Cryogenically cooled D_2 gas jet/cluster targets, which can reduce the debris-induced optical degradation, were tested as acceleration sources for deuterons from which one can ignite the DD fusion reaction [85, 88, 96]. A bulk cooling system was required to cryogenically-cool the gas to generate clusters.

In this chapter, the acceleration of deuterons and the fusion neutron production from a heavy water stream target are reported. By irradiating a room temperature heavy water jet with a high repetition rate femtosecond laser (½ kHz with several mJ pulse energy), we demonstrate the possibility of a compact and portable laser-based neutron source producing a time-averaged flux of $dN/dt > 2 \times 10^5$ s^{-1}. In order to understand the initial neutron angular and energy distribution, the deuteron energy spectra were measured and compared with the detected neutron Time-of-Flight distribution. As discussed above, the results from laser-based ion accelerations and following neutron generations have limitations: 1) operating at low repetition rate systems (< 10 Hz), 2) requiring relatively high energy of laser pulses (> 1J), 3) re-

quiring cryogenic cooling system, and 4) debris problem. By introducing a heavy water stream as the target, these problems are resolved or minimized. The results presented in this thesis also suggest further potential application to the higher repetition laser system (> 10 kHz), expecting comparable characteristics of neutrons from large neutron sources (e.g. large nuclear fusion systems and/or spallation sources).

4.2 Experiment setup

The experiment was performed using λ^3 laser system at the University of Michigan. The experimental setup is shown in Fig. 4.1. The laser delivers up to 18 mJ energy per pulse focused upon heavy water stream targets. The laser was focused to a 1.3 μm Full Width at Half Maximum (FWHM) focal spot using an $f/1.4$ Off-Axis Parabolic mirror (OAP), which produced a maximum peak intensity of 3×10^{19} W/cm^2 in vacuum. The chamber pressure was maintained at 20 Torr during the experiment by a roughing pump. Heavy water vapor originating from the stream fills the chamber and therefore acts as a catcher for accelerated deuterons for neutron generation in addition

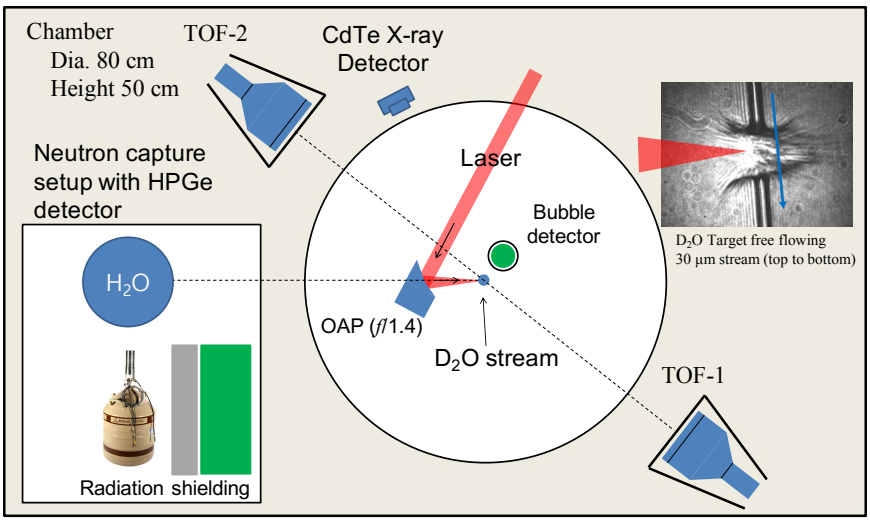

Figure 4.1 Experimental setup. HPGe detector and scintillator characterization detectors for neutron capture signal are position adjustable. Image is not to scale.

to the bulk water stream target. Second harmonic light reflected from the stream and off the parabolic mirror passes out of the chamber and was used to guarantee a normal incidence focus on the stream's surface. The CdTe X-ray detector was then used to optimize this alignment minutely to produce X-ray counts on every single shot. Fine target alignment was performed using linear piezo actuators (Newport Picomotor) for xyz-control of the paraboloid and the water stream.

4.2.1 Water target

A room-temperature heavy water(D_2O) stream from a commercial (Teledyne Isco) syringe pump was used as the target. The syringe pump was used to maintain a constant flow rate of heavy water through a 10 μm capillary, which produced a 15 μm diameter continuous flow of either heavy (D_2O) or light (H_2O) water, with a flow rate of 100 μL/min. The laser focus was set approximately 300 μm below the tip of the capillary and at the first surface normal to the flowing water. Fig. 4.2 shows the water target used. During the experiment, the chamber pressure was held at 15 Torr, which corresponds to the vapor pressure of the water target. This high pressure, relative to typical ion acceleration experiments, not only provide the catcher target but also prevented a target freezing issue; when the water stream is stored at a reservoir, splash-back water is attached onto the reservoir. The water puddle freezes and it grows from the bottom to the top toward the laser-water interaction area. Surface tension may provide another source of freezing from the top to bottom. The water pulled by the capillary surface tension experience the solidification (crystallization).

The deuterium nuclei in the chamber 'catch' accelerated deuterons from the laser interaction, thereby increasing the neutron yield. The effect of different catcher geometries and compositions for DD fusion has been studied both experimentally and computationally [53, 86, 93, 161–163], but the secondary target is not necessarily beneficial for the maximization of neutron flux, it rather depends on the target tem-

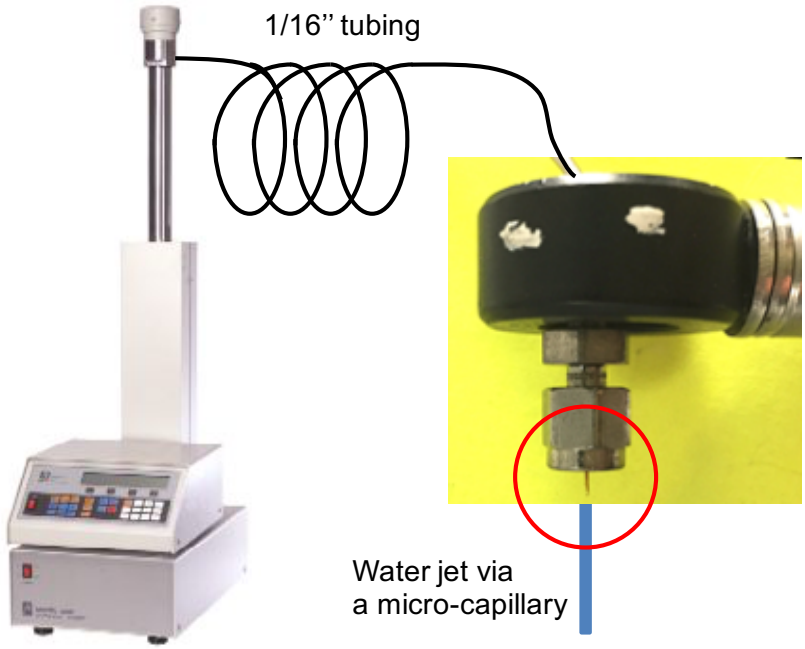

Figure 4.2 A diagram of the water target generation system. (a) Syringe pump (Teledyne Isco, 100DM Syringe Pump) (b) An assembly of the capillary and tubing system. The assembly is connected to the pump using 1/16" stainless steel tube. The micro-capillary was hold onto a 1/16" $\times$ 0.4 mm standard capillary ferrule (GCFerrules). The pump provides can provide pressure under two different operation modes: constant pressure and flow rate.

perature and its corresponding stopping power [53].

There are several reasons that could shorten a capillary life. First, a capillary cutting is made by a hand-operating tool (Shortix Fused Silica Tubing Cutter). The cutting surface is not perfectly clean, breaking a balance of the surface tension. Another defect is a laser-induced shock. The laser focus is $\sim$300 μm below from the end of capillary. The shockwave impacts the capillary aggravating the unbalance surface tension. Due to unbalanced surface tension, the water stream direction would be changed from its original direction (i.e., normal to the ground) to a random direction. This directional change of the water target can become severe when the target generation is resumed after the operation is stopped. Thus, the target location or OAP position was controlled during the experiment. For fine target alignment (including optical alignment of the OAP and probe beam), Picomotors were used for xyz-control

of the paraboloid and the water stream. At the early stage of a target-generating operation, low angle deviation can be corrected by controlling target locations or applying high back pressure on the syringe pump temporarily, but, in case of high angled water target ($> 20°$), the capillary replacement is required. To image the target region (water stream), a microscope objective (60x) was used, with a 405 nm laser diode illuminating the water target. A digital delay generator (Stanford Research System, DG535) controlled the laser diode timing, delayed with respect to the laser oscillator. The image is recorded by CCD camera.

Pre-alignment was conducted manually before closing the experimental chamber. After the chamber lid is closed and the chamber pressure decreases, post-alignment procedures are required, as follows: When laser pulses interact with the water stream, the second harmonic-generation photons are reflected from the stream and subsequently off a parabolic mirror which directs the light out of the chamber, the generation of which is used to guarantee a normal incidence focus on the stream's surface. The CdTe X-ray detector is then used to precisely optimize this alignment to produce X-ray counts on every single shot.

4.2.2 Pre-plasma

In high intensity ($> 10^{18}$ Wcm^{-2}) interactions with solid targets, pre-pulses or ASE in CPA laser systems can be sufficient to ionize the target material, generating *pre-plasma*, i.e., a surface plasma generated prior to the arrival of the main pulse. The pre-plasma expands normal to the target surface with an exponentially decreasing density profile away from the target. The main laser pulse interacts with this plasma at the critical density surface (for $\lambda = 800$ nm, $n_c = 1.8 \times 10^{21}$ cm^{-3}) rather than at the original target surface position. In order to maintain an interaction between the dense material surface and the full intensity of the laser pulse, the laser intensity contrast ratio must be high to limit pre-plasma formation. Several different

methods have been applied for high contrast laser systems such as an electro-optic method [164], optical parametric−CPA (OPCPA) [165] and plasma mirrors [166–168]. Using the plasma mirror scheme, the laser-pulse contrast-ratio can be improved up to 10^{11}, allowing ultra-intense "*clean*" laser pulse interactions with effectively *preplasma-free* targets [169–172]. Several studies demonstrated that ion acceleration from laser-plasma interactions can be affected by pre-plasma characteristics, which can be initiated by different time scales of pre-pulse energy; nanosecond-timescale ASE [47, 173–175] and picosecond-timescale prepulses [176]. Due to the different ion acceleration mechanisms, higher pulse contrast ratio does not guarantee higher ion energies or higher conversion efficiency, i.e., there may be optimal pre-pulse levels (duration and/or amplitude) for a given scenario [47, 174–178].

In the experiment described here, we deliberately introduced an extended ASE with prepulse at shoulder of ASE in advance of the main pulse to increase the energy conversion efficiency. The pre-pulse was controlled by varying the pulse injection and pulse-picker timings. One pulse prior to the main pulse was intentionally leaked out of the laser regenerative amplifier cavity, amplified and compressed ahead of the main pulse. As a result, the ASE was extended from 5 ns to 15 ns and there was a small pre-pulse at 13.4 ns with an intensity contrast ratio of 10^8. Figure 4.3 shows temporal laser profiles with/without pre-pulse. This pre-pulse generated a pre-plasma and increased the absorption of the main pulse energy. As a result, the pre-plasma expanded and the D_2O stream had non-sharp boundaries. The creation of this pre-plasma can be beneficial as it increases the coupling efficiency of the laser energy to the production of hot electrons [174, 175, 179–181], which enhances the energy of the deuterons. In this thesis, an enhancement of neutron fluxes by a prepulse was reported and it will be discussed more in Sec. 4.3.4.

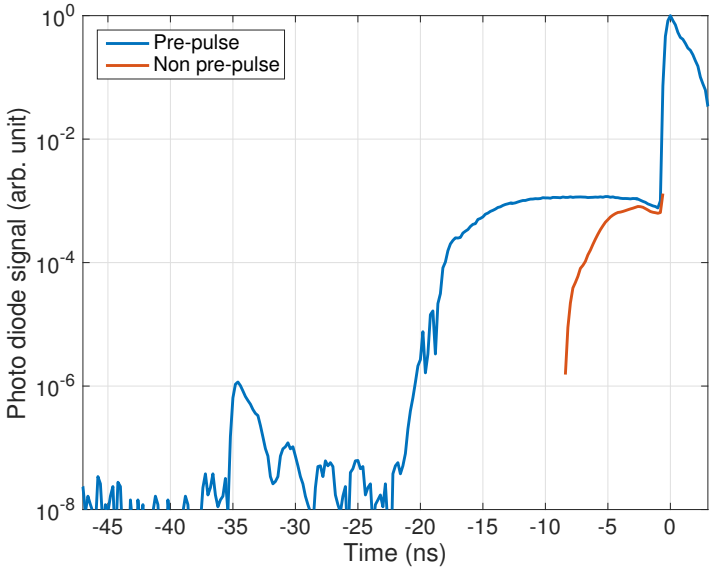

Figure 4.3 Temporal profile measurements of the laser pulse using a fast photo diode. Main pulse is located at 0 sec, prepulse is extended from 5 ns (red) to 15 ns (blue).

4.2.3 Aperture control system

Piezo linear actuators (Newport, Picomotor) have less than 30 nm step size. While the step size could be affected by a load on the Picomotor, the optical parts or target system weight are not heavy enough to affect the step size. Thus, our step size can be assumed 20 nm. The open-loop configuration has no feedback mechanism, it is hard to track current position or total movements of the motors. Alternatively, the relative movements can be measured by keeping the same directional movements and counting relative movement are required.

4.2.4 Deuteron detection

To measure deuteron acceleration, the CR39 plastic track detector is used with a mylar filter stack. The thin mylar films (each of 2 and 3 μm thickness) are overlaid to obtain different cutoff energies of the deuterons extending up to 840 keV, which corresponds to transmission through an 11 μm film. The cutoff energy is calculated

Table 4.1 Calibrated cutoff energies for given mylar film thickness. The latter two columns include corrections for the energy loss in the heavy water vapor.

Thickness (μm)	Uncorrected (keV)	at 13.5 cm (keV)	at 31 cm (keV)
4	375	510	655
6	525	640	770
8	660	760	880
10	780	870	980

with SRIM software [109]. The exposed CR39 plastic sample undergoes an etching process with a NaOH solution for one hour at 90 degrees Celsius. After the process, we use an optical microscope to capture images of the region of interest (See Fig. 4.4) and ImageJ software to counts ion pits. The 15 Torr of D_2O vapor inside of the chamber provides extra stopping power against accelerated deuterons. In this experiment, we located the CR39 detectors at 31 cm and 13.5 cm away from the water target, a separation necessitated by the limited physical access within the chamber. At these separations, exposure times of 5 to 10 s result in a roughly optimized number of countable pits that neither oversaturate the detector nor are unduly sparse. Under this pressure and distance, the cutoff energy of the mylar filter must be corrected for the deuteron's energy loss in the D_2O vapor. For instance, at 13.5 cm and 31 cm, the corrected cutoff energy for a 6 μm film is 640 keV and 770 keV, respectively rather than 525 keV. The corrected cutoff energies are tabulated in Table 4.1.

While neutrons can make extra tracks on the CR39 detector by recoiling protons, the number of tracks due to neutron-proton recoils is negligible in the neutron yield from this thesis. In Ref. [110], the CR39 shows neutron detection efficiency of $(1.1 \pm 0.2) \times 10^{-4}$ and $(6.0 \pm 0.7) \times 10^{-5}$ for the DD (2.45 MeV) and DT (14.1 MeV) cases, respectively, and the efficiency were determined for standard CR-39 etch conditions (etched in 6.0 molarity NaOH held at 80 degrees Celsius). For instance, only 2 neutron-induced tracks are expected on a CR 39 at 10 cm away from the source among 10^1 to 10^3 deuteron-induced ion pits.

4.3 Experimental results

4.3.1 Deuteron acceleration

At two different locations (TOF1: 13.5 cm at $-30°$, and TOF2: 31 cm at $+100°$, see Fig. 4.1), deuterons were detected by CR39 plastic track detectors with mylar filter stacks. This allowed an energy spectrum to be obtained, with the assumption of an exponential distribution with characteristic effective temperature k_BT, by measuring the number of ions transmitted through the various thickness layers. Figure 4.4 shows one scanned image of a typical CR39 plate. The numbers on the image represent the total thickness of the mylar filter layers in micrometers. The central region has a total mylar thickness of 10 μm. The outer annulus of Fig. 4.4 is the shadow of the filter holder.

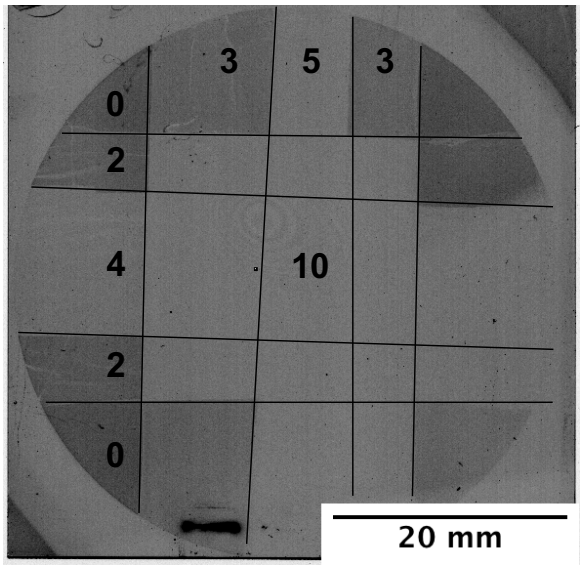

Figure 4.4 A scanned CR39 images of 14 mJ laser pulse with 5 s exposure. A mylar filter stack is applied, and the circular outline is the shadow of the filter holder. The numbers indicate the thickness of the total mylar layers in μm. The central region of the CR39 is covered by a total thickness of 10 μm mylar film. The black lines represent the edges of the filter layers and are added to distinguish the different filter areas.

In Fig. 4.5, the microscope images through different filter thicknesses are shown. Figure 4.4 is the result of a 5 sec exposure for the detector at 13.5 cm at 30°. The

software application ImageJ was used to count the number of ion pits, as illustrated in Fig. 4.6. From the software, false ion signals are rejected by their size and circularity. For each region of interest (via different thicknesses of filters), small areas (780 μm $\times$ 580 μm) within the region were selected and analyzed 2–8 times to obtain better statistics. Deuteron spectra are shown on Fig. 4.7, in which both the measured data and the fitted curves are plotted. Note that data below 0.4 MeV are not plotted and excluded for the curve fits because there are too many ion pits to count. (e.g., 0 μm case of Fig. 4.5)

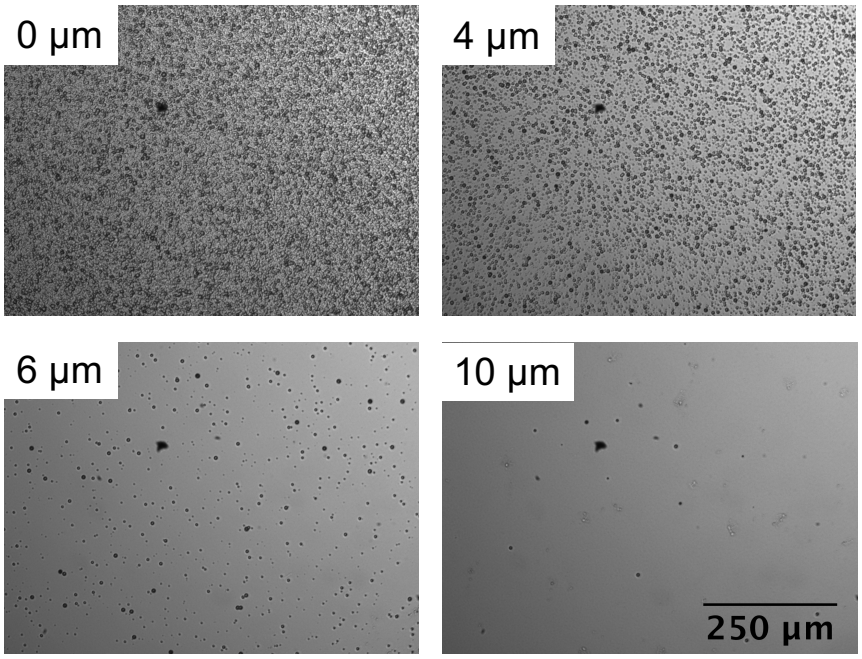

Figure 4.5 Magnified images of ion pits through different thickness of mylar filter. Note that identical four optical defects are located at the center of the images, which is a shadow of dust on the microscope's lens.

The spectra confirm that deuterons are accelerated up to approximately 0.9 MeV. When comparing the flux above the 0.4 MeV region, it is comparable to the 2D PIC simulation result shown in Sec. 4.4 2D PIC simulation showed orders of 10^9 deuterons ($>$ 100 keV) in both directions. The backward traveling deuterons (toward low density side of heavy water vapor side) acted as an additional neutron source.

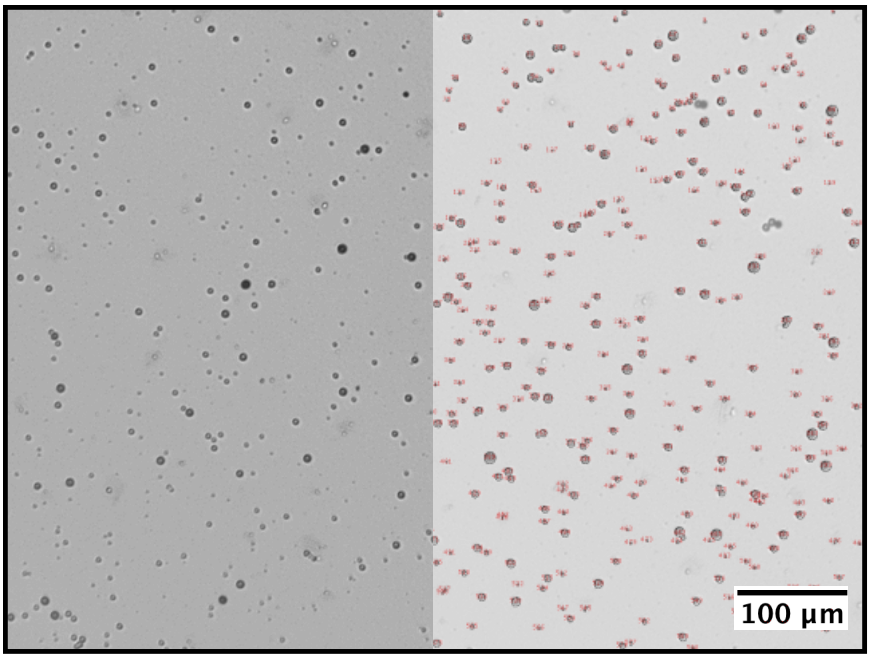

Figure 4.6 An example of the method for counting ions using ImageJ, with 6 μm of mylar filter. The left half shows a raw image, and the ion masks counted by the software are overlaid onto the right half of image.

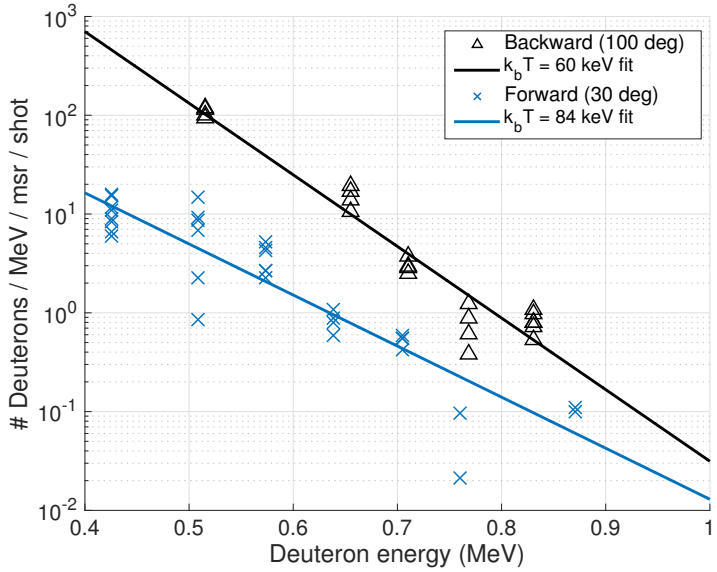

Figure 4.7 Deuteron energy spectra of forward-directed and backward-directed deuterons derived from CR39 detectors after 5 s laser exposure.

4.3.2 The effect of laser z-position on neutron generation

The high-numerical-aperture focusing system in this experiment (f-number = 1.4), gave a short *Rayleigh* range ($2z_r$=9 μm), requiring an accurate alignment of the target to have a high energy conversion efficiency from laser to target. In previous solid target experiments conducted by the group, solid targets were scanned along the laser axis to maximize the X-ray generation [158, 182]. Here, the laser focal position was scanned rather than the target position to achieve better neutron generation, and the relative neutron fluxes at different focal spot positions were measured from the scintillator traces. The focusing optics (OAP) was scanned because the water target translation stage was non-orthogonal to the laser axis. The OAP was attached to a 5-axis stage (three translation and two rotation). Two rotational axes (pitch-, yaw-axis) were manually aligned during the basic alignment procedure before pumping out air. Three translational axes were controlled during experiments by Picomotor. The OAP was moved along the laser propagation axis by the Picomotor within a range from -40 μm to $+20$ μm with a 10 μm step size. Hysteresis due to the open-loop configuration was minimized by keeping the same directional movement of the OAP. It should be noted that when the OAP was moved along the focal axis, its transverse position was modified in order to maximize the radiation flux on the CdTe X-ray detector. Figure 4.8 shows results of the focal-spot scan-experiment. For a given set of system parameters, its *Rayleigh* length (z_R) is 9 μm, and by retracting the focal point 10 μm, the neutron production rate is scaled to half its maximum value. Also, at –20 μm, the expected beam intensity is 17 % of the peak intensity, which happens to match the neutron production rate. At -40 μm, the corresponding beam intensity is 5% of the peak intensity, but the neutron flux is about 40 % of the peak flux. A possible explanation for this odd neutron flux could be the transverse alignment. The Picomotor moves the OAP stage, but the stage axis and actual OAP focal axis could have an offset. When the focal axis was moved, the laser focus was moved not only

along the focal axis but also along the transverse axis. This offset resulted in a 45° incident angle against to the target surface, resulting in a higher coupling efficiency. Another possibility is that the prepulse conditions, such as a scale length could have changed dramatically.

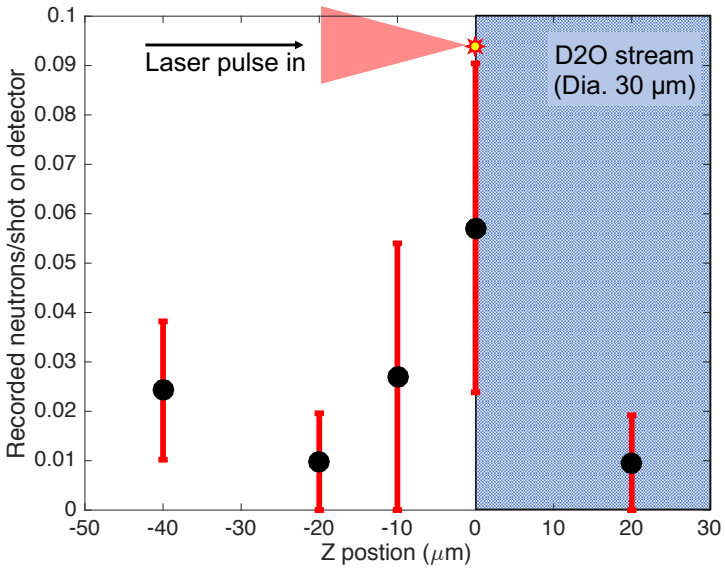

Figure 4.8 Focal spot scan experiment schematic, and the result. Y-axis presents the number of neutron recorded on the plastic scintillator per shot. The OAP stage was moved along the laser propagation axis a range from -40 μm to 20 μm.

4.3.3 Time-of-Flight measurements

Time-of-Flight techniques were also applied to the scintillator trace to confirm the neutron generation and its energy spectrum. The technical details are described in Sec. 3.2.2. From an individual scintillator trace (e.g., Fig. 3.9), if a neutron is generated and detected by scintillation detectors, a neutron peak will appear following an X-ray peak because neutron travels slower than a photon. From the delayed neutron signal, the neutron energy may be estimated.

Averaged traces from the scintillator data are plotted on Fig. 4.9. The graph shows the averaged results of more than 3000 recorded signals, with the amplitudes

normalized with respect to each of the peak X-ray signals after averaging. In the figure, the red line shows the D_2O result and the blue line shows the H_2O result taken with identical experimental setups except the target composition. In the presence of heavy water, a peak corresponding to the average neutron signal follows the X-ray peak with a certain time delay. The secondary peak generated by the neutrons was recorded at 100 ns. The expected time of arrival of 2.45 MeV neutrons is 92 ns for the given detector configuration (at 135° with respect to laser propagation direction, 2 m away from the target). This 8 ns of error will be discussed later with simulation results and a histogram analysis. When the target was replaced by H_2O, X-ray signal appeared at the same time, but no secondary peak was recorded.

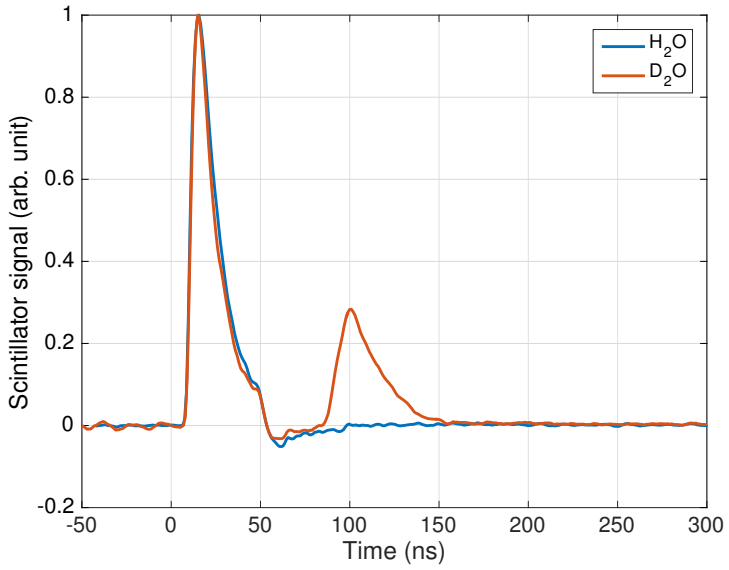

Figure 4.9 ToF traces from D_2O and H_2O targets for 2 m distance. These traces are averaged and normalized with respect to X-ray signals from more than 3000 recorded traces. Both traces show the same response to X-ray. X-rays arrive at 7 ns and neutrons are delayed and arrive around 90 to 100 ns time window.

Another plastic scintillator was located at different In similar way on Fig. 4.9, the secondary neutron peaks appeared at only heavy water experiments (red and black). However, due to the detector distance being larger, the red trace shows a more delayed

neutron peak at around 170 ns.

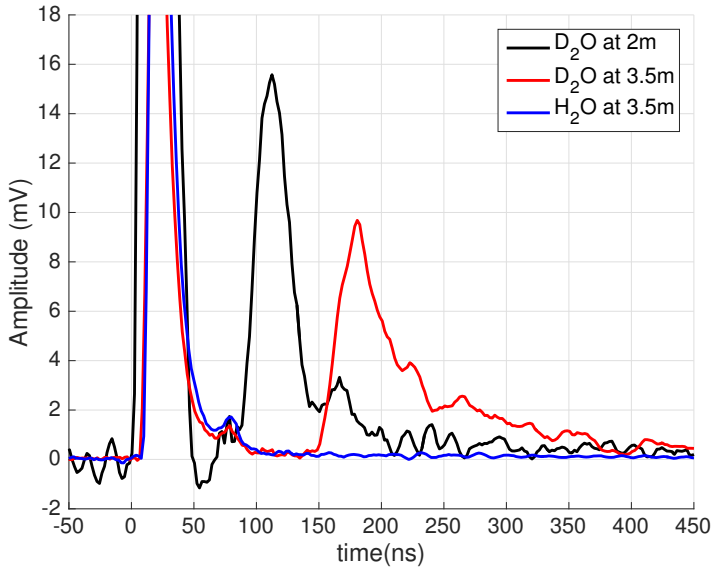

Figure 4.10 ToF traces from D_2O and H_2O targets. X-axis is calibrated as laser-water interaction time, t=0. Y-axis is voltage readout amplified by PMT. H_2O trace (blue) has only X-ray peak, but, the other D_2O (red and black) traces show neutron peaks at corresponding time delays by 2 m and 3.5 m detector distances.

These results confirmed the generation of neutron from an intense laser-heavy water interaction. While the averaged trace lose individual trace of ToF information (rise time, decay time, and amplitude) but it gives general trend of the neutron detection.

From the given detection configurations (D, detector distance) and the measured time difference between X-ray and neutron peaks($\delta_{x,n}$), the neutron velocity is given as follows:

$$v_n = \frac{Dc}{c\delta_{x,n} + D} \tag{4.1}$$

In experiment, without enough shielding for strong X-ray signals from laser-water interaction, scintillator was easily saturated and the signal overran expected neutron peak position, removing neutron information. Due to strong X-ray environment, the scintillator assembly was located behind 10 cm thickness of lead wall, and other sides

except the front had 5 cm of lead wall. This wall attenuated strong X-rays giving moderated level of light output through scintillator, but, some weak X-ray signal would attenuate below the detection level of the scintillator showing only neutron peaks on ToF traces. Figure 4.11 shows two neutron signals at the same time (∼92 ns) with/without X-ray peaks.

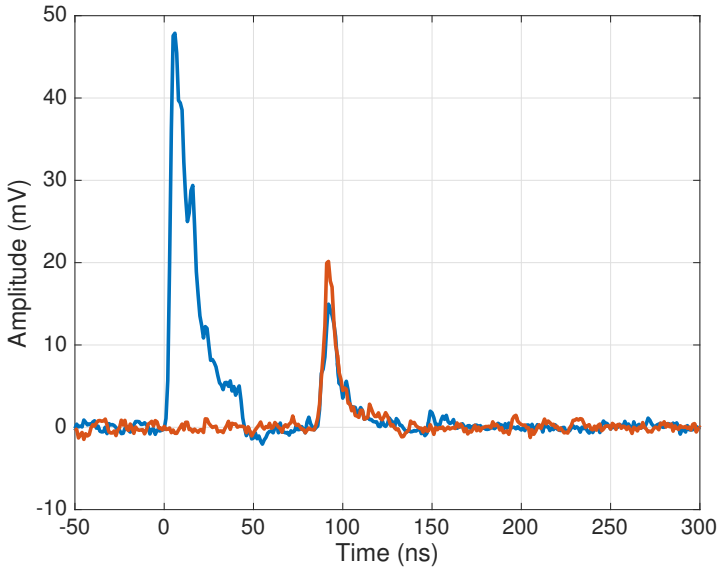

Figure 4.11 ToF traces with a strong X-ray and an attenuated X-ray signals. A radiation shielding (lead wall) blocked photons, not neutrons, generating neutron peak (red). But, some strong photons can penetrate the shielding and yield enough light output showing X-ray peaks (blue).

Because of the missing X-ray peaks on the trace, the time difference between X-ray and neutron peaks($\delta_{x,n}$) may not be available every time, requiring the alternative way to find neutron velocity rather than Eqn. 4.1. Note that there would be an extra time gap between neutron generation and laser-water interaction. This time gap will be discussed later in this section. The absolute zero time can be calculated from recorded X-ray peak time with a given detector distance. All the recorded X-ray peaks showed the same rising-edges, (not the same amplitude), and the rising-edge time would be the time that the photon arrives. Considering this, the neutron velocity

was already derived in Eqn. 3.5 in Sec. 3.2.2.

$$v_n = \frac{D}{D/c + \delta_{x,n}} = \frac{D}{t_n} \qquad \text{(3.5 revisited)}$$

Here, D is a detector distance, $\delta_{x,n}$ is peak time difference and $t_n (= D/c + \delta_{x,n})$ is neutron peak time with respect to zero time. The corresponding neutron energy is obtain with classical kinetic energy equation as follows:

$$E_n = \frac{m{v_n}^2}{2} = \frac{mD^2}{2(D/c + \delta_{x,n})^2} \qquad (4.2)$$

For 2.45 MeV of neutron from D-D fusion, it would have 85.7 ns of peak time difference ($\delta_{x,n}$) or 92 ns of total ToF ($= D/c + \delta_{x,n}$).

Using the MATLAB software, the time-of-arrival distribution of the neutron signal was shown in Fig. 4.12, in which the histogram has a total of 979 neutron arrival data points and each bin width is 4 ns. It should be noted that the MCNP simulation confirmed that attenuation and scattering of fast neutrons may be ignored for 1.95-meter distance including the vapor and the chamber wall. A thermal distribution of deuterons broadens the neutron energy spectrum; the grey-colored histogram in Fig. 4.12 shows the measured neutron arrival time distribution and the red region indicates the expected neutron signal generated promptly from the laser-water target interaction (2.45 MeV$\pm$0.32 MeV). This was calculated using the measured deuteron temperature based on a beam fusion mode model [183], $\Delta E_n = 35\sqrt{T_i}$, where T_i is the deuteron characteristic temperature. $T_i = 84$ keV was taken from the measured effective temperature of the forward directed deuterons. The most probable transit time of the histogram is 90 ns, which corresponds to an energy of 2.45 MeV for a neutron generated at the laser interaction time ('prompt' neutron) 1.95 m from the detector. For the early arrival neutrons ($<$ 90 ns), 497 out of 979 neutrons (50.8 %) were detected before 90 ns, which was well matched to the broadened neutron

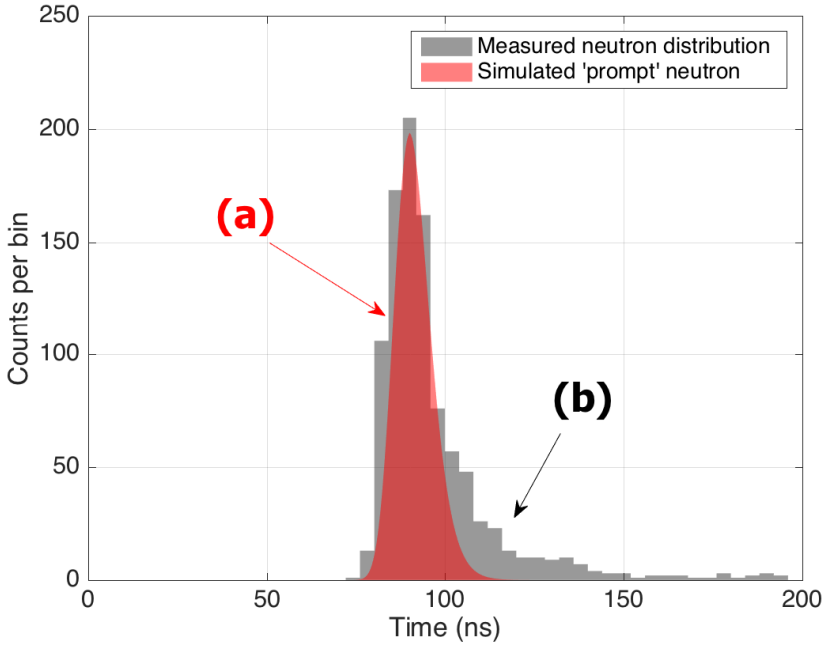

Figure 4.12 Histogram of neutron arrival times. Total neutron count is 979 from 48000 shots of laser. Approximate neutron detection efficiency of the EJ-204 plastic scintillator is 20 %, giving 8×10^4 neutrons/sec. (a) Expected 'prompt' neutron distribution with spectral broadening due to the thermal distribution of the deuterons. (b) Tail of 'delayed' neutrons generated in the vapor.

energy spectrum (red area), area below 0 ns to 90 ns region is 50.7 %. For the late arrival neutrons (> 90 ns), the measured neutron arrival times were lengthened more than the broadening of the neutron spectrum due to the deuteron energy distribution (see Fig. 4.12 (b)), which can reduce the neutron lower energy to 1.56 MeV (113 ns in ToF). The measured data showed that 11% neutrons arrived after 113 ns. These 'delayed' neutrons can be explained by the backward directed deuterons that interact with the vapor. Due to the low density of the vapor, the deuteron stopping distance is significantly extended (a few cm to a few μm). This extra deuteron transit time is a few tens of ns. These escaped deuterons generate fusion reactions which could take place through the entire chamber volume, leading to a delay of ToF signals. The spread of ToF signals also was observed by Karsch *et al.* [86], who employed catcher to catches ions from both front and rear surfaces of water droplets. Here,

a self-generated D_2O vapor catcher stops the accelerated deuterons throughout the chamber and one does not, therefore, observe clear secondary neutron peaks at a highly localized catcher location (see Fig. 4.13).

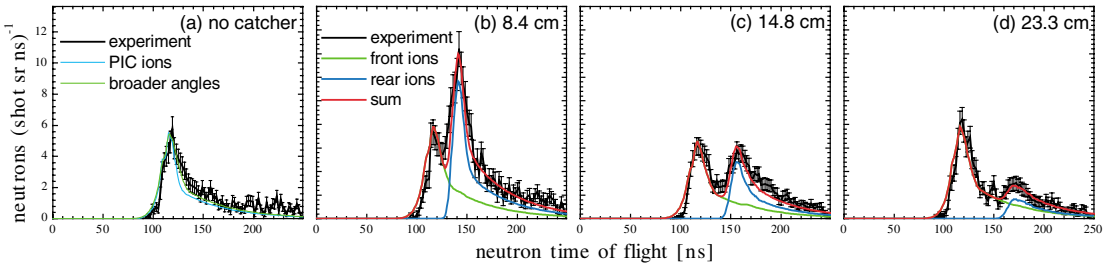

Figure 4.13 Neutron TOF from front/rear surface of heavy water droplet. Adapted from Ref. [86]

4.3.4 Neutron flux measurement

In order to measure the neutron flux, two different techniques were employed: 1) neutron bubble detectors and 2) HPGe detector. First, neutron bubble detectors (Bubble Tech Industries, BD-PND) were placed inside the chamber and exposed to the laser-based neutron source for a total of 2 minutes for each experiment. The 2-minute time duration was chosen to limit the number of bubble below a countable number of bubbles. During the measurements, the bubble detectors are covered with a 1 mm thick aluminum tube to avoid direct laser irradiation. With the calibration factor of 6900 neutrons per bubble, the number of bubbles can be converted to the neutron fluxes (see Sec. 3.2.3). Second, gamma-ray emissions from neutron-scatter and neutron-capture reactions in surrounding materials are measured by a cryogenically cooled cylindrical HPGe detector (Ortec Pop-Top model No. GEMPM45P4-108, dimension: H 3.27 cm $\times$ ϕ 8.47 cm). The HPGe detector is located 1.67 m from the target and a shielding wall consisting of 10 cm of borated-polyethylene and then 5 cm of Pb attenuates the neutron and induced gamma-ray flux as well as the direct X-ray flux directed upon the HPGe detector. A water-filled cylindrical container (H

30 cm × ϕ 27.5 cm, located on the laser propagation axis, 180 °) placed 78.7 cm from the detector is exposed to the direct neutron flux and neutrons are (predominantly) captured by hydrogen nuclei within the water resulting in a neutron-capture reaction and subsequent gamma-ray emission at 2.22 MeV (^{1}H(n,γ)). The measured HPGe gamma spectrum was compared with that produced by a MCNP simulation that included an isotropically emitting (point) neutron source, the water container, and the HPGe detector. The captured gamma-ray interaction rate within the HPGe detector can be derived from both simulated and measured spectra, from which the neutron flux of the source can be estimated. The location of both the detectors is shown in Fig. 4.14.

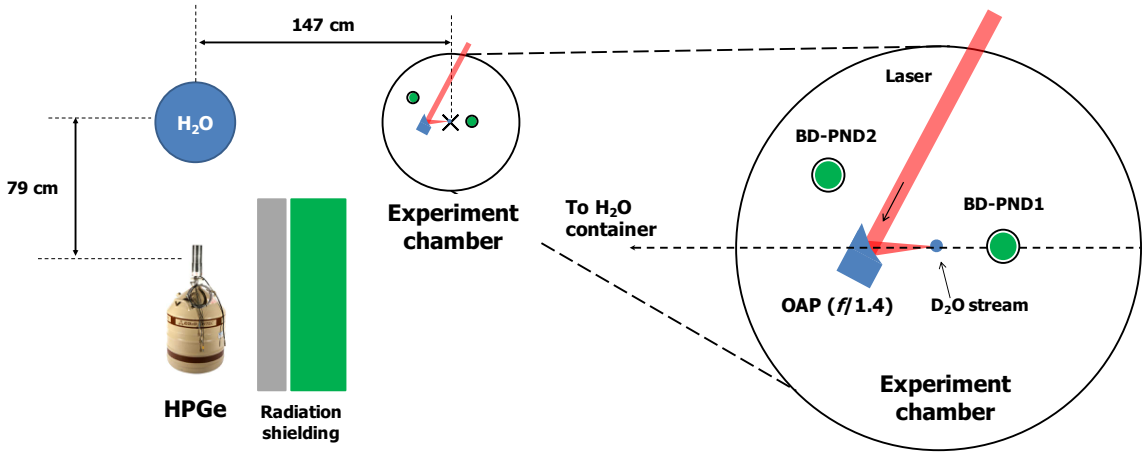

Figure 4.14 Detector location diagram. HPGe detector and bubble detectors are located outside/inside the chamber. Inside the chamber, two BD-PND detectors are located at 4cm, 0° and 6.8 cm, 120°. BD-PND: Bubble detector, Radiation shielding: (Gray) 5 cm of Pb, (Green) 10 cm of borated-polyethylene slab.

Neutron fluxes were measured by the bubble detectors with different incident laser energies. The λ^3 laser system delivers up to 18 mJ energy of pulse with a 35 fs of pulse width (FWHM). A half-wave plate is located before the compression grating of the λ^3 system, and used to control a laser pulse energy. In this experiment, the laser pulse energy varied between 6 mJ and 12mJ with a deliberately introduced

pre-pulse (extended ASE with a prepulse at 13.4 ns) Because the detector surface has a curvature (ϕ1.5cm) there is an optical distortion. To reduce error due to this distortion, the same detector was captured in images from four different directions and then counted. Unlike a CR39 ion pit counting, the bubble detector includes a lot of (super-heated) micro-bubbles, which is hard to be filtered by a particle counting function of ImageJ program. Instead of using a built-in function, bubbles are manually counted by sight from the image. Figure 4.15 (d) has a total of 41 neutron-generated bubbles, after irradiation from 12 mJ laser pulse, for 2 minutes. Empirically, 60 bubbles on the one side view is the upper limit for reasonable counting without overlapping or avoiding distortion from the curvature edge.

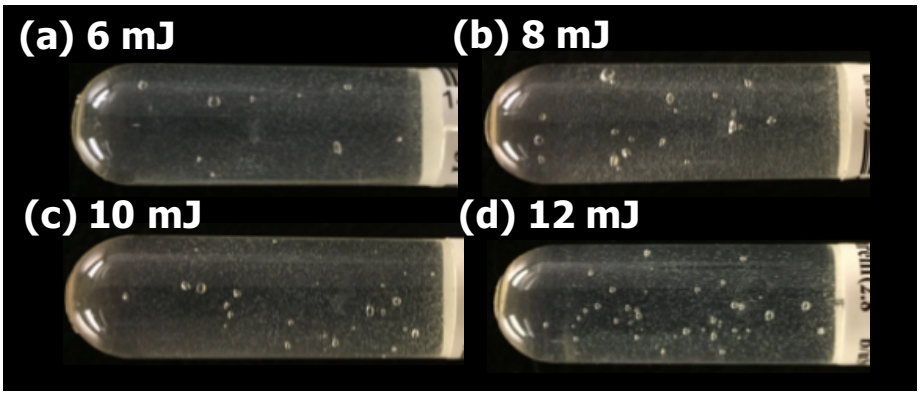

Figure 4.15 Bubble formations on the PD-BND detector. At different laser pulse energies, bubble detectors were exposed for 60,000 shot (2 minutes). Black paper was used as a background for better contrast. (a) − (d) have 9 to 41 bubbles on the detectors.

From the calibration factor (6900 neutron per bubble) and the number of bubbles, the neutron fluxes were estimated and plotted on Fig. 4.16. At each laser pulse energy, 3 to 5 measurements were performed, with different laser pulse energy from 6 mJ to 12 mJ. A calibrated neutron flux varies from order of 10^4 neutrons/s to 10^5 neutrons/s. This neutron flux was also estimated by a simulation. The simulation was performed from the 2D PIC simulation of deuteron spectra and its weighted cross-sectional considerations. More details about the simulation will be described

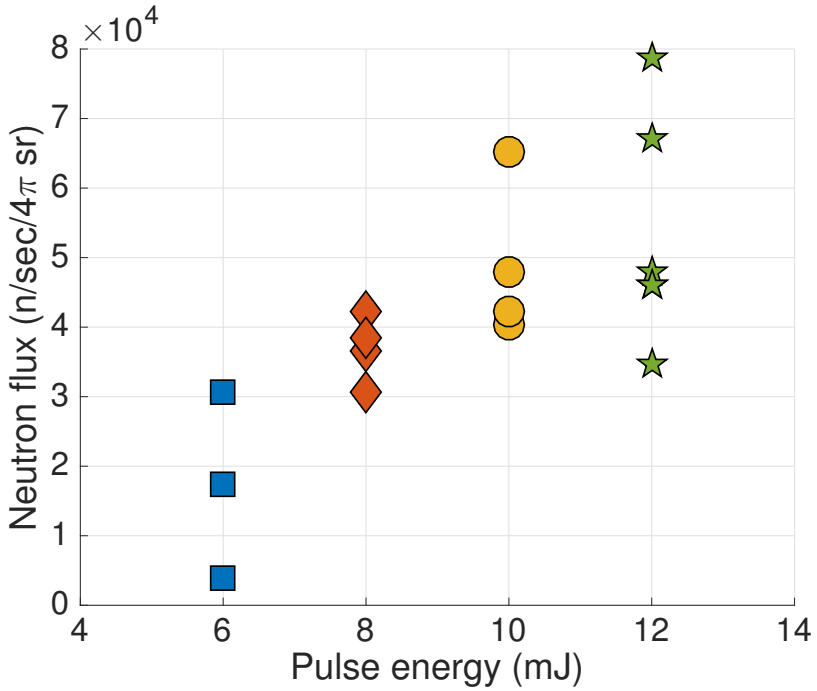

Figure 4.16 Neutron flux scaling with laser pulse energy

in Sec. 4.4. To confirm that the bubble formation was from DD fusion neutrons, the fluidic target was replaced with normal water (H_2O) and the same experiment was conducted. To ensure no remaining heavy water was inside the system (pump and chamber), the reservoir unloaded heavy water and refilled/emptied normal water more than two times. Also, for possible remaining vapor inside the chamber, the chamber was pumped out for more than ten minutes. Under this cleaned deuterated environment, a normal water (H_2O)-laser interaction experiment was conducted with bubble detectors and plastic scintillators. The results were shown in Fig. 4.17. After 2 minutes of exposure, no bubble formation was observed, (Fig. 4.17 (a)), and as shown in Fig. 4.9 already, only a photo peak was detected by the plastic scintillator. These results confirmed that our system generates neutrons, and a flux of the order of 10^5 neutrons/sec.

As another neutron detection method, a proton-neutron capture gamma was used.

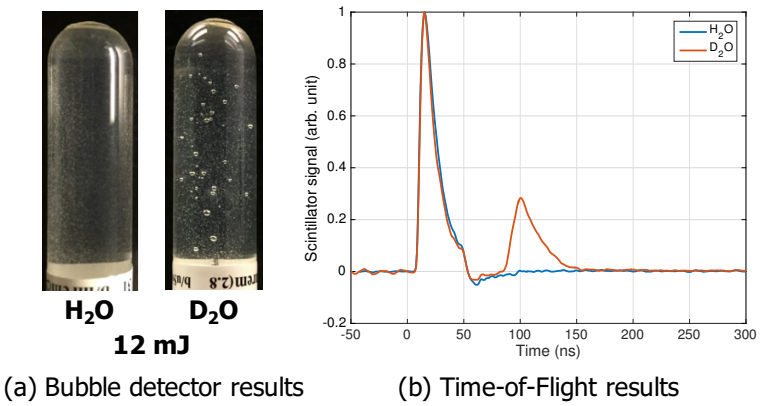

(a) Bubble detector results (b) Time-of-Flight results

Figure 4.17 D_2O vs. HO comparison experiment results. (a) Bubble detectors were exposed to 60,000 laser shots of a 12 mJ pulse energy. (b) Figure 4.9 (revisited). Time-of-Flight measurement results confirmed that neutrons were found in the heavy water experiment, not in the normal water experiment.

Figure 4.18 shows gamma spectra collected during the heavy water experiments. The background gamma-ray distribution (black in plot) of the laboratory was collected for 8 hours and compared with the results from a 2 hour laser run (red in plot). The two spectra were normalized with respect to the live-time (251,100 sec for background and 7,200 sec for laser run) of the measurement. The inset of Fig. 4.18 shows raw data sets. The energy axis was calibrated from 14 lines in the background. The details of background emission lines are tabulated in Table 4.2.

In Fig. 4.19, an energy axis was expanded from 2 MeV to 2.7 MeV. A few isotope-emitted gamma rays were noted on the plot (^{208}Tl, ^{214}Bi) and one distinguished peak was observed at 2.22 MeV. At the peak, a proton-neutron capture gamma signal (^{1}H(n,γ)) grew in intensity with a constant rate across the 2 hours of the experiment. From the MCNP simulation, the 2.22 MeV neutron-capture gamma from hydrogen is the predominant feature regardless of the neutron source (DD or DT). Because the deuteron energy extended only up to 1 MeV (see Sec. 4.3.1), neutrons from these deuterons were likely to be emitted isotropically [161, 184]. When simulating the configuration (DD neutron source, water source, and HPGe detector at each position), 1.59×10^9 neutrons from the isotropic source were required to generate the

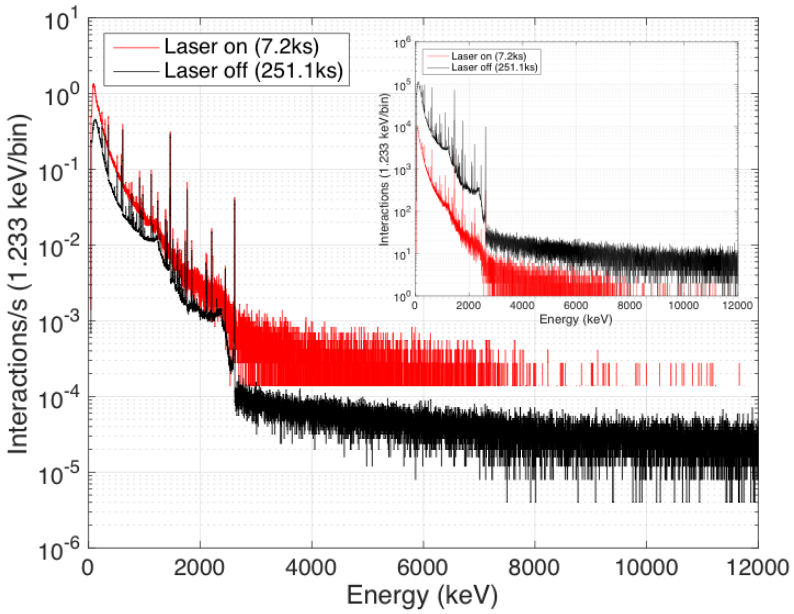

Figure 4.18 HPGe raw data, and normalized w.r.t time(per second)

Table 4.2 Spectral lines used for a HPGe calibration. From these lines, a following calibration equation was obtained. Energy (keV)= channel number × 0.8113 + 0.3195.

Isotope	FWHM (keV)	Energy (keV)	Channel number
Pb-212	0.94	238.5	293
Pb-214	1.01	295.03	363.31
Pb-214	1.06	351.75	433.36
Bi-214	1.29	609.32	750.67
Bi-214	1.66	1120.34	1380.81
K-40	1.94	1460.88	1800.31
Bi-214	2.08	1729.73	2131.53
Bi-214	2.12	1764.63	2174.59
Bi-214	2.16	1847.58	2276.9
Tl-208	3.36	2103.7	2592.38
Bi-214	2.16	2118.73	2611.52
Bi-214	2.37	2204.3	2716.38
Bi-214	2.3	2447.97	3016.48
Tl-208	2.73	2614.533	3222.14

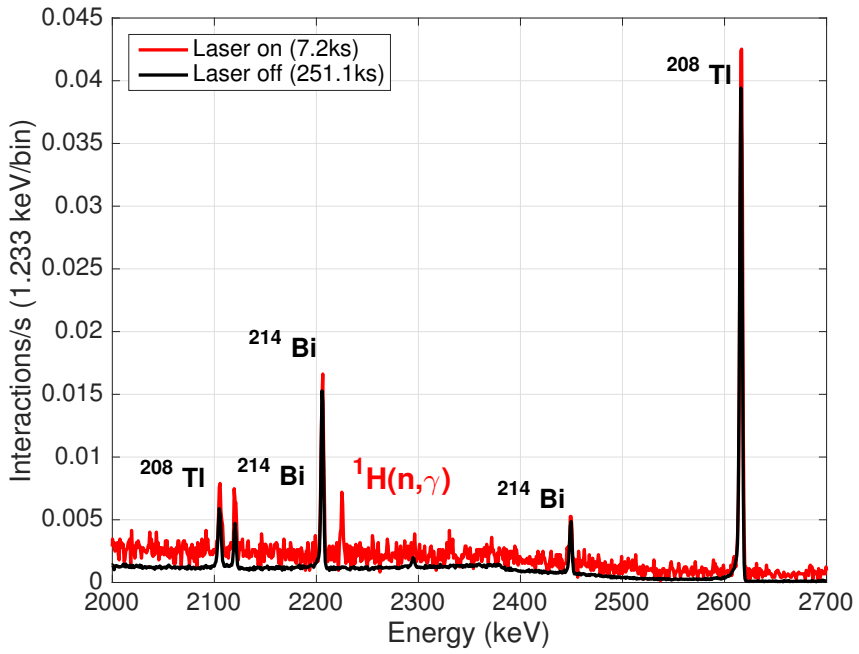

Figure 4.19 HPGe gamma-ray spectra from 2 MeV to 2.7 MeV showing the difference between the background distribution (in black) and the laser-on distribution (in red). The background was collected for 8 hours and the laser-on distribution was collected for 2 hours. ^{1}H(n,γ) peak at 2.22 MeV is distinguished from the background.

86 ^{1}H(n,γ) counts (2.22 MeV peak) in the distribution, which given the measurement time, resulted in 2.2 $\times$ 10^{5} neutron per second.

Additionally, from the simulation, the second most prominent gamma-ray line was found at 596.4 keV (^{73}Ge(n,γ)), which is the nuclear emission following the neutron capture by ^{73}Ge within the detector itself. Although the borated polyethylene and lead shielding reduced the direct neutron exposure upon the HPGe detector, unattenuated and scattered neutrons (from the shielding, the water container target, and surrounding material) can thermalize and interact within the detector, as confirmed by simulations that include the shielding configuration. For unattenuated neutrons that have a direct path to the detector, 99.9 % of 2.45 MeV DD neutrons travel through the vapor-filled chamber without losing their energies, and among them, 36.5 % of neutrons still have 2.45 MeV energy after 5 cm of thick Pb housing. A 5 cm

of borated polyethylene shield reduced the number of unattenuated 2.45 MeV neutrons by 77.6 %. Based on the simulation, ^{73}Ge(n,γ) was looked for in the recorded spectra. Because of high fluxes of photons on lower energy regions, original spectra had high-background counts to blind the information. Compared to the background, ^{73}Ge(n,γ) peak was very small. Each plot's background slope was removed by MATLAB software and the results were plotted in Fig. 4.20. The peak was recognizable, but not enough to estimate the total neutron flux, which interacted with Ge within the detector.

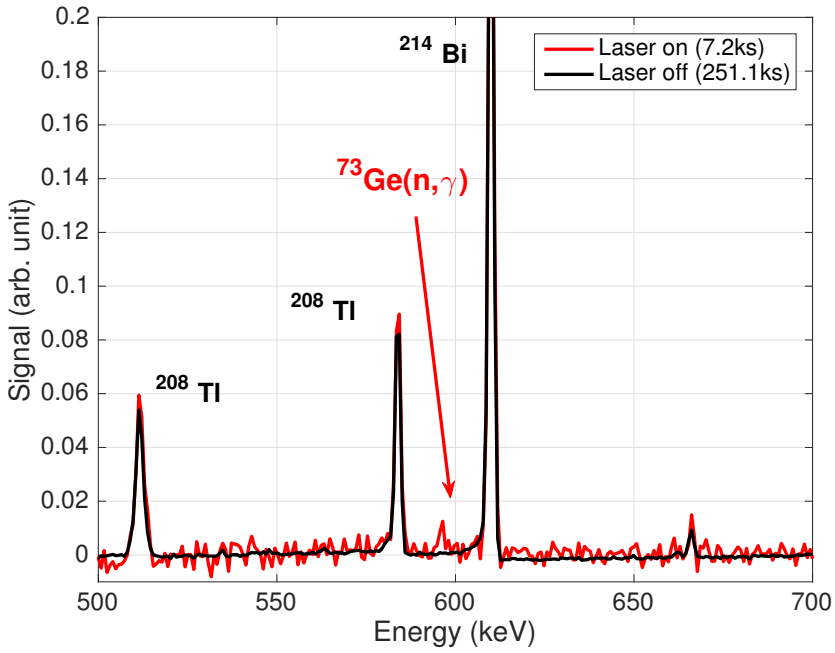

Figure 4.20 HPGe gamma-ray spectra from 0.5 MeV to 0.7 MeV showing the difference between the background distribution (in black) and the laser-on distribution (in red). The background was collected for 8 hrs and the laser-on distribution was collected for 2 hrs. the baseline of the background distribution was removed to clarify the appear of the germanium capture peak.

4.3.5 Back filling helium gas experiment

During the experiment, the chamber was held at 15 Torr to prevent water from freezing and to provide additional catcher atoms (deuterons in heavy water va-

por). For most intense laser experiments, a vacuum environment is required to deliver the laser beam to the target without a breakdown when it is focused. When the atmospheric breakdown occurs, the laser experiences wavefront modification by breakdown-induced plasma (due to refractive index of the plasma) such as self-induced defocusing, plasma absorption, and scattering phenomena. Usually, the modification of the laser wavefront causes its intensity to degrade. To reduce the negative effect of plasma, a shallow focal depth setup or lower electron density can be introduced, and the higher breakdown (ionization) threshold of the environment (gas) can be used. A shallow focal depth can be achieved from a high numerical aperture (or low f-number) optics setup. Electron density or its ionization threshold issue can be resolved simply from the vacuum system. Through the vacuum systems, electrons avoid a scattering due to the atmosphere air and successfully generate X-rays. Although the vacuum system can suppress atmospheric loss the electrons/ions and is beneficial for X-ray generation or accelerating electrons/ions, the vacuum-based experimental setup makes the system more complex and expensive. In order to test vacuum-free X-ray generations, there have been efforts to generate a laser-based X-ray source by filling a helium gas at atmospheric pressure or flowing the helium gas near the target [158, 185, 186]. In this section, we examined deuteron generation and its following DD fusion reaction under different background helium environments. Ion experiences much higher stopping power when traveling through a medium. For example, 100 keV deuteron travel only 12 mm in 1 atm of Helium gas, compared to 170 mm in 50 Torr (1 psi). (see Fig. 4.21)

The experimental setup was the same as a heavy water experiment. To detect neutrons, the same plastic scintillator detector with photo-multiplier tube assemblies were employed to conduct Time-of-Flight analysis. The experimental process is as follows: First, the chamber was evacuated up to 0.3 psi (15 Torr). Here, it should be noted that pressure was read/controlled in psi units because the pressure meter showed in

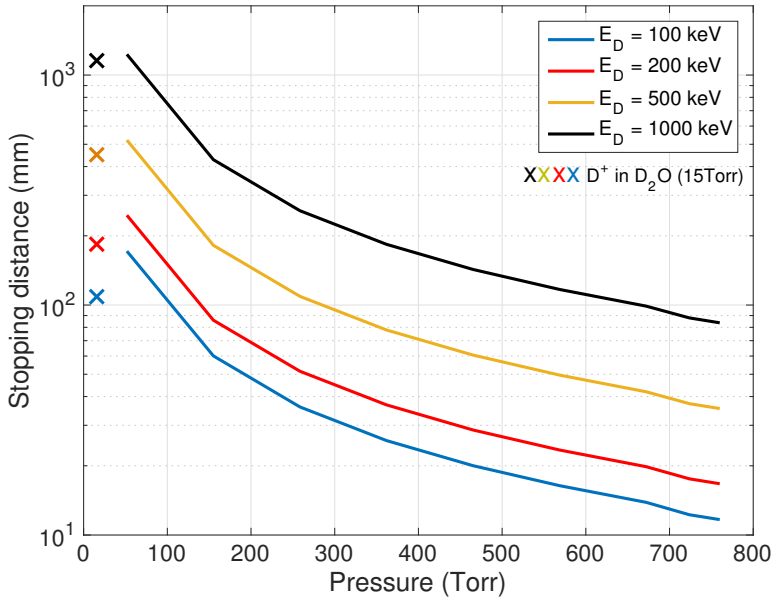

Figure 4.21 Deuteron stopping distance in Helium gas. X data points at 15 Torr represent deuteron stopping distances by only 15 Torr of deuteron vapor without Helium gas.

psi unit. Laser pulses irradiated the heavy water and neutrons were detected by the scintillator. Second, a helium gas was back-filled up to a target pressure. In order to minimize an effect on system alignment by a fast gas flow, a gas supplying tube inside the chamber was covered by housing to guide a gas flow below the optical component. Pressure was varied from 1 psi to atmospheric pressure with a 2 psi step. After filling a helium gas at the test pressure, the OAP was re-aligned by a picomotor along the laser propagation axis (Z-axis), maximizing (time-averaged) X-ray signals on the CdTe detector. Third, when the radiation signals were stabilized, a series of data acquisition were made. The laser operated at 480 Hz repetition rate, and the oscilloscope saved data for a 20-second duration in a triggered-sequential mode. A single trace records 1 μs time duration, and five sets were saved. Thus, a total of 48,000 traces (10-second duration) were saved for each pressure. The result was plotted in Fig. 4.22. Blue line shows relative neutron fluxes measured by plastic scintillators and red line is a FWHM result neutron arrival time distribution.

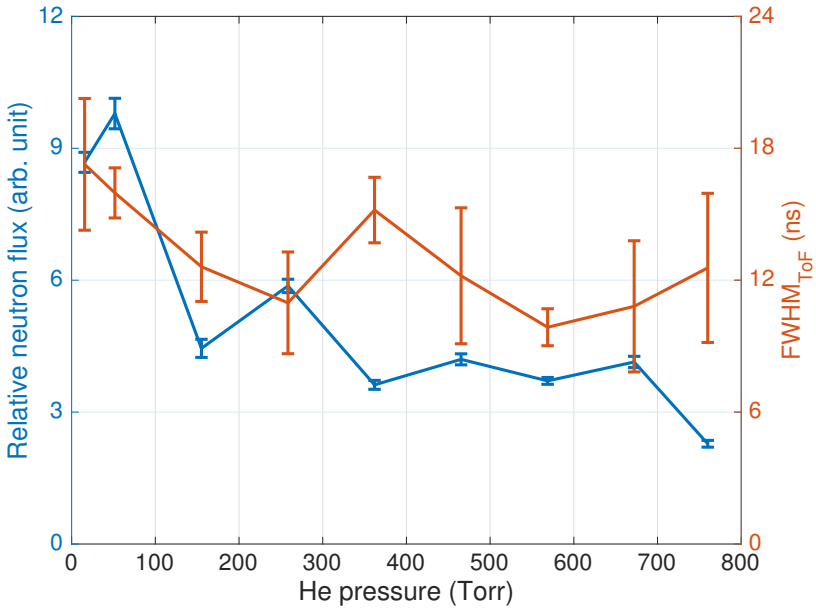

Figure 4.22 Relative neutron flux vs. Helium gas pressure. Left Y-axis (blue) represents relative neutron flux from the scintillation detector and right Y-axis(red) is FWHM of neutron arrival time distribution.

Generally, as back-filling Helium pressure increased, neutron flux decreased. At atmospheric pressure, only 25% neutron flux was measured compared to maximum neutron generation at 50 Torr (1 psi); however, this value corresponds to 50,000 neutrons per sec. Another interesting finding is FWHM of the neutron arrival time spread. The FWHM of the distribution was calculated from a histogram such as Fig. 4.12 with Gaussian curve fitting. As mentioned above, actual distribution was not exactly matched with Gaussian profile, because of 'delayed' neutrons (extended tails toward later time). However, more than 50% of neutrons were concentrated in expected time zone, approximated FWHM can be obtained from Gaussian curve fitting.

Because of extra stopping power of Helium gas, deuterons will stop closer to the target stream. This infer that Helium gas confines fusion reactions within limited volume. From this, FWHM of the neutron arrival time distribution can be interpreted as fusion volume or source size. Therefore, less 'delayed' neutrons and less broadening of

FWHM were expected as higher back-filling Helium pressure. As shown in Fig. 4.22 (red line), FWHM result did not show clear correlation with Helium pressure. There are two possible explanations: 1) More than 50% of stopping distance change by Helium gas occur below 200 Torr and there was not big decrease in stopping distance after 200 Torr. Therefore, above the 200 Torr level, extra source size reduction would not to be expected. 2) Statistically, at the higher pressure, less neutrons were recorded, and even small number of 'delayed' neutron could broaden FWHM calculation by Gaussian fitting. Therefore, a dramatic reduction of source size was not shown in this experiment. Nevertheless, from the backing pressure variation experiment, we showed that a neutron generation can be achieved atmospheric pressure condition.

4.3.6 Pulse duration experiment

The best pulse duration (τ) of the λ^3 system is 45 $\pm$ 2 fs. This pulse duration can be modified by a compressor grating separation. (See Sec. 3.1.1). From the point at the shortest pulse duration generated, we examined how the separation of the grating affects neutron generation, moving the one side of grating position up to 1 mm. Pulse duration was measured by SHG-FROG and 3rd order autocorrelator. Figure 4.23 shows pulse duration measurement results with different compression separation. Different colors represent a direction of grating movement. Like Helium gas experiment, relative neutron fluxes were measured varying laser pulse durations from 46 fs to 300 fs and results are shown in Fig. 4.24.

Result shows that neutron flux is not proportional to pulse durations. One may expect a higher intensity pulse (shorter pulse duration) may give a higher neutron flux. Rather than intensity, neutron flux can be affected by the direction of grating movement. In Fig. 4.24, all blue data points (shorter grating separation) are below red data points (longer grating separation) and from the blue data, neutron flux decrease as pulse duration is extended until 235 fs. In case of red data points, there was no

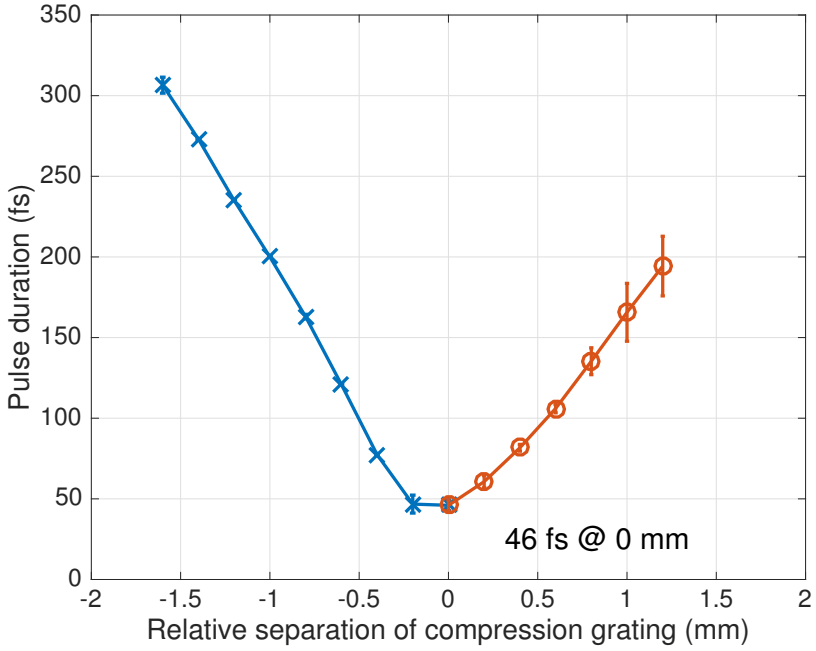

Figure 4.23 Pulse duration measurement result. Pulse duration expands from 46 fs to 300 fs. X-axis represent relative separation of grating. Different colors are applied to distinguish direction of grating movement.

general trend.

From the pulse duration experiment, we can draw two interesting points: 1) Neutron flux is sensitive to pulse duration, especially, chirp condition (direction of grating movement) may be critical. 2) With sub-picosecond pulse, a moderate level of neutron can be generated showing the possibility of longer pulse system like a high-power fiber laser.

4.4 Simulation and discussion

4.4.1 Particle-in-cell simulations

To elucidate the experimental results, particle-in-cell (PIC) simulations were run by George Petrov from the Naval Research Laboratory. Due to the high complexity of the nonlinear and kinetic processes that can occur during the interaction of a high-

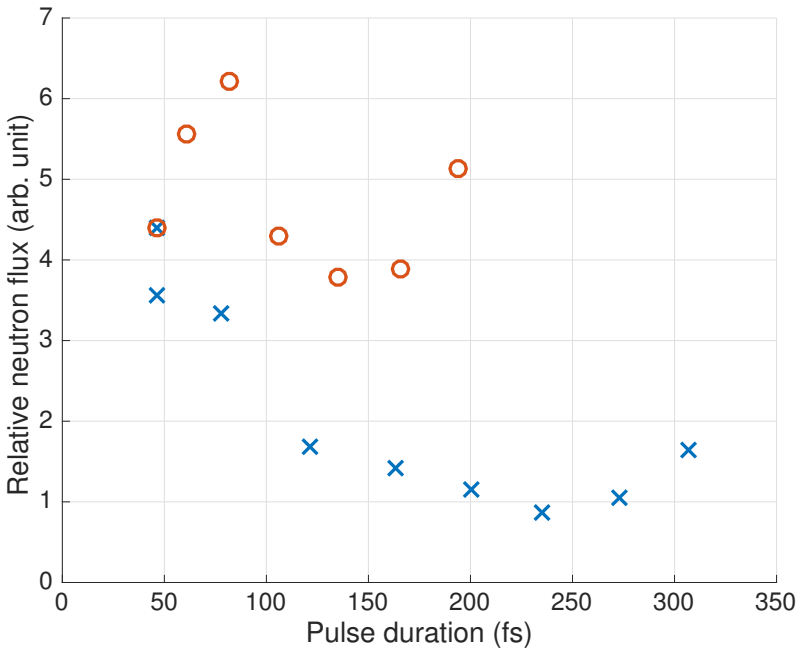

Figure 4.24 Relative neutron flux measurement with different laser pulse duration. Different colors of data points represent the direction of grating movement. This color code is the same as pulse duration measurement. (see Fig.4.23)

intensity laser or particle beam with plasma, computational modeling can be very important. PIC simulation is a great tool for complex systems as it supports the full kinetics of multi-dimensional plasmas.

A PIC simulation models complex laser plasma interactions. In self-consistent EM fields, the PIC simulation tracks collective motion of charges on a particle-mesh grid. More details of PIC method is described in Ref [187]. Briefly, The PIC scheme has the basic steps as follows:

1. Equations of motion are integrated by 'Particle pusher' to calculate particle's position and momentum.

2. Currents charge density calculation is calculated from distribution of weighted particles on the grids.

3. From the results of step 2, solves Maxwell's equations. Here, external fields (laser pulse) and self-induced fields are included.

4. Go to step 1 with the calculation result of weighted fields so that particles move to a new position with new momentum through self-consistently calculated EM fields.

In this thesis, the simulation code was used to simulate only the laser plasma interaction, from which the deuteron spectrum was calculated. It was fitted with an exponential function. Deuterons with weights corresponding to this distribution were transported through the converter, and the neutron yield generated by these deuterons was calculated and accumulated. The angular distribution of neutrons was assumed to be isotropic, which was justified in the limit E_d <1 MeV [161].

The on-target laser energy was varied between 3.7 and 11 mJ/shot. Particles are initialized with charge +1 for ions and −1 for electrons and during the simulations the ion charge of oxygen is dynamically incremented using a standard Monte Carlo scheme for collisional and optical field ionizations. At the beginning of the simulations, the number of particles per cell is 36 for deuterons and 18 for oxygen ions. The momentum distribution of deuterons is plotted in Fig. 4.25. The phase-space plot

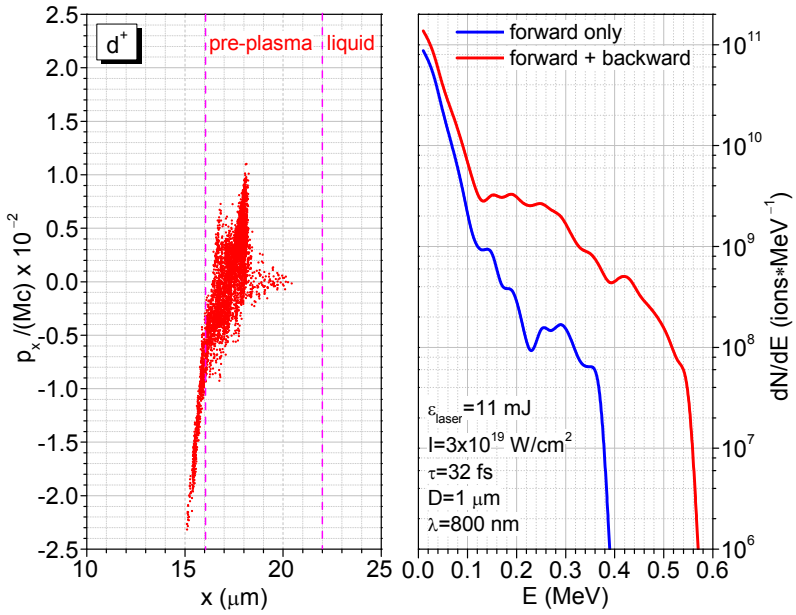

Figure 4.25 (Left) Deuteron momentum $x - p_x$ phase space at the end of simulation, 192 fs. (Right) Deuteron energy spectrum.

reveals the dynamics of the interaction. First, the laser interacts primarily with the pre-plasma and all of the energetic ions originate from the pre-plasma region. The second intriguing observation is that there are two groups of deuterons: one group accelerated forward, and another group blown in the backward direction (towards the incoming laser direction). Their number is comparable, however, the backward moving deuterons are more energetic. While in the forward direction the maximum normalized impulse is $p_x/(Mc)\sim0.01$. The corresponding momentum in the backward direction is doubled. Different acceleration mechanisms therefore are likely explanations for these two groups of deuterons in the experiments; a hole boring mechanism for the forward directed deuterons [72, 73] and TNSA for the backward directed deuterons [46, 65]. The neutron production is very sensitive to the direction of the deuterons. The forward-directed deuterons see increasingly dense plasma, all the way up to liquid density in the stream. Since their range is only a few μm in water (7 μm for a 400 keV deuteron), the forward directed deuterons are stopped within the water stream [109]. These deuterons cause DD fusion reactions and produce neutrons within the water stream. This is a *point source* of neutrons. In contrast, the backward directed deuterons move away from the main stream and interact with the gas/plasma with rapidly decreasing density, which transitions to the 15 Torr background density, where they have a much longer stopping distance. We estimated that at a background density in the chamber of 6.4×10^{17} cm^{-3}, a 400 keV deuteron has a stopping distance of 30 cm, similar to the chamber dimensions. Therefore, the backward-moving deuterons will also contribute to neutron production as a *volumetric source*. This is illustrated in Fig. 4.26 which plots the neutron flux produced by forward and backward moving deuterons, as well as the sum of the two. The experimental data are also plotted for comparison. Table 4.3 provides more details such as the number of deuterons per shot, the neutron yield per deuteron and neutron yield per shot for forward and backward moving deuterons. The dominant neutron

Table 4.3 Simulation result table

Intensity (W/cm^2)	Energy (mJ)	# Deuterons > 100 keV	T(keV)	Neutron yield (neutrons/ions)	Neutron yield (neutrons/shot)	
1×10^{19}	3.7	1.4×10^{9}	18	4.0×10^{-9}	6	Forward
		3.3×10^{9}	45	18×10^{-9}	59	Total
2×10^{19}	7.3	2.6×10^{9}	30	9.5×10^{-9}	25	Forward
		5.0×10^{9}	55	26×10^{-9}	130	Total
3×10^{19}	11	3.7×10^{9}	35	12×10^{-9}	44	Forward
		6.7×10^{9}	65	138×10^{-9}	255	Total

source is fusion from backward moving deuterons and consequently the larger fraction of neutrons have a volumetric origin. It has to be kept in mind, however, that we assumed complete stopping of the backward-directed deuterons, while in reality, some them may not be stopped by the low-density background gas. Thus their contribution is likely overestimated. The volumetric nature of the neutrons was confirmed by the neutron time-of-flight measurements, which showed a delay and increased width of the signal, which can only be interpreted as neutrons coming from different locations.

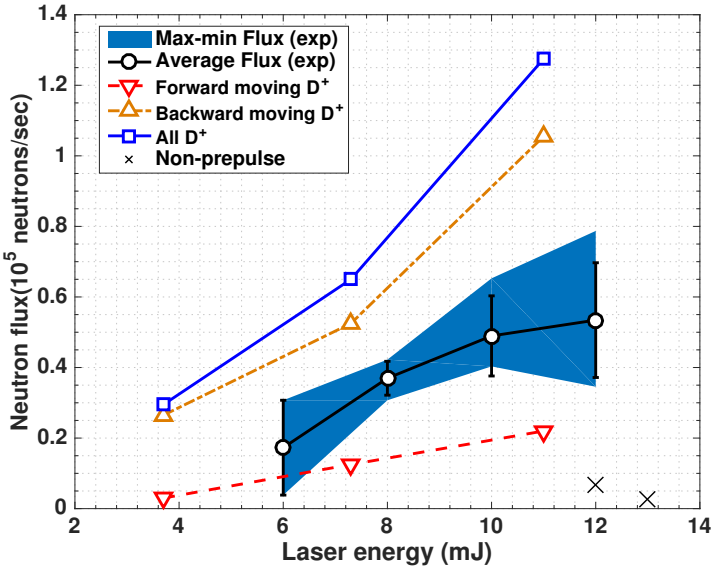

Figure 4.26 Neutron flux as a function of energy from the experiments and simulations.

4.5 Conclusion and future works

In conclusion, the production of fast neutrons via deuteron acceleration and their subsequent D-D fusion reactions at a laser intensity of 3×10^{19} Wcm^{-2} is demonstrated using a multi-mJ, fs duration pulsed laser system operating at a high repetition-rate (½ kHz). The deuteron energy spectra have been measured at two different directions with mylar filter stacks. In both directions, deuteron energies are measured up to 0.9 MeV, and the total numbers of deuterons above 0.4 MeV is comparable to that yielded in a 2D PIC simulation results [188]. Without an extra pitcher-catcher arrangement, accelerated deuterons collide with deuterium nuclei in the heavy water stream ('prompt') and vapor in the chamber ('delayed'), yielding a 2.45 ± 0.32 MeV energy neutron flux of 2.2×10^5 per second. The neutron average flux is comparable to other laser-based neutron sources [85, 88, 91, 95, 189–191], but the neutron source presented here only requires a few mJ of pulse energy, which can be achieved without a bulky and complex cryogenic target-cooling system.

Table 4.4 shows the comparison results of laser-based neutron sources. Based on neutron yield in units of (n/sr/shot), our neutron source does not look attractive; however, when considering a laser repetition rate and pulse energy, our source would be much better than other sources. Furthermore using the high-power fiber optics, which operate at a much higher repetition rate, a very high time-averaging neutron source can be made. Last two experiments (involving helium gas and pulse duration) were preliminary studies for these future applications.

For the better understanding of the source characteristics, a few more studies can be suggested. To enhance neutron flux, there was an extended ASE with a prepulse. From direct comparison between 'clean' pulse and extended pulse, almost 10 times more neutron flux was achieved. As mentioned in Sec. 4.2.2, an existence of pre-pulse (including ASE) brings quite different laser-plasma interactions. Therefore, a systematical control of prepulse and measurement of induced pre-plasmas would lead

Table 4.4 Laser-based neutron sources comparison with our result.

Publications	Reaction	Neutron yield (n/sr/shot)	Repetition rate	Energy (J)	**Neutron yield (n/J/sr/sec)**	Intensity (Wcm^{-2})
Roth *et al.* [57]	$^{9}Be(d,n)^{10}B$	1×10^{10}	45 mins shot cycle	80	5×10^{4}	$(1–10) \times 10^{20}$
Higginson *et al.* [90]	$^{7}Li(d,n)^{8}Be$	8×10^{8}	2 shots/hr	360	1×10^{3}	2×10^{19}
Lancaster *et al.* [91]	$^{7}Li(p,n)^{7}Be$	4×10^{8}	1 shots/hr	69	2×10^{3}	3×10^{19}
Higginson *et al.* [92]	$^{7}Li(p,n)^{7}Be$	1×10^{8}	2 shots/hr	140	4×10^{2}	1×10^{20}
Zulick *et al.* [93]	$^{7}Li(p,n)^{7}Be$	1×10^{7}	0.1 Hz	1.1	9×10^{5}	2×10^{21}
Norreys *et al.* [94]	$^{2}d(d,n)^{3}He$	7×10^{7}	1 shot/hr	20	1×10^{3}	1×10^{19}
Fritzler *et al.* [85]	$^{2}d(d,n)^{3}He$	1×10^{6}	1 shot/hr	62	4	2×10^{19}
Zulick *et al.* [93]	$^{2}d(d,n)^{3}He$	1×10^{5}	0.1 Hz	1.1	9×10^{3}	2×10^{21}
Willingale *et al.* [53]	$^{2}d(d,n)^{3}He$	5×10^{4}	1 shot/min	6	1×10^{2}	$(1–3) \times 10^{19}$
Ditmire *et al.* [88]	$^{2}d(d,n)^{3}He$	8×10^{2}	10 Hz	0.12	7×10^{4}	2×10^{16}
Ter-Avetisyan *et al.* [89]	$^{2}d(d,n)^{3}He$	5×10^{2}	10 Hz	0.6	8×10^{3}	1×10^{19}
Pretzler *et al.* [95]	$^{2}d(d,n)^{3}He$	20	10 Hz	0.2	1×10^{3}	1×10^{18}
This thesis	$^{2}d(d,n)^{3}He$	73	500 Hz	0.01	4×10^{6}	3×10^{18}
Fiber laser	$^{2}d(d,n)^{3}He$	–	10 kHz or higher	0.01	–	10^{16}

well-characterized laser neutron sources.

CHAPTER V

THz generation

5.1 Introduction

Among various regimes of electromagnetic radiation, Terahertz (THz) (1 THz = 10^{12} Hz) radiation has been intensively studied due to its applications in various areas [192–194]. For many decades, THz spectroscopy has been used in chemistry fields, because the rotational and/or vibration absorption spectra of many molecules fall in the THz frequency range [195]. Also, because of their non-intrusive characteristics, THz imaging techniques can scan samples that are covered with low Z materials such as paper or plastic. Another important feature is that, unlike X-rays, THz will not cause ionization of materials [196]. The main objective of this chapter is to optimize THz radiation using an adaptive optic (deformable mirror, DM) with an active feedback system (genetic algorithm, GA). Chapter III described the adaptive optic and its feedback routine in detail. A genetic algorithm, using the THz signal as a figure of merit, determines the voltage settings in a deformable mirror and results in up to a six-fold improvement in the THz signal, compared with the settings optimized for the best focus. It is possible to use this technique in optimizing for different THz generation processes. These studies will provide insights into revealing the exact mechanism of THz generation, which is still obscure.

Until the early 1990s, research on THz radiation was hindered because of the

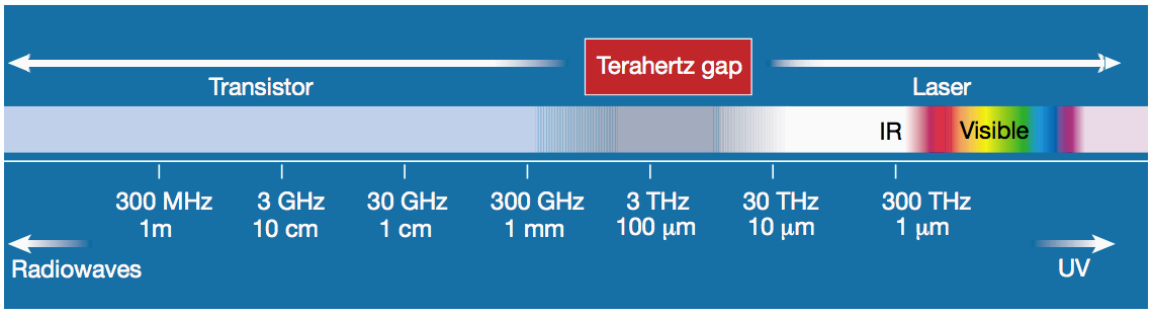

Figure 5.1 Terahertz gap in electromagnetic spectrum. Image is adapted from Ref. [197]

"*Terahertz gap*" (see Fig.5.1). The THz gap is the electromagnetic spectrum between optical/photonic and electronic sources of radiation. Many efforts have been undertaken to expand the frequency regime from both directions (high and low frequency regions). First, the electronic approach generates an electromagnetic wave by moving electrons, which means the wave frequency depends on how fast electrons alternate the direction of the electric fields. This is fundamentally limited by the speed of the electrons. But when a current-alternating frequency increases to approach the THz region, the travel distance of the electrons becomes shorter, and THz radiation fails to be generated. This is because there is not enough time for electrons to cross a transistor channel. Also, power output will suffer lower efficiency because of the high resistance from the high frequency of alternating fields. When it comes to the photonic approach or modern physical explanation, shorter wavelength radiation can be achieved when electrons move between atomic energy levels (characteristic X-ray emission). Also, when a charged particle decelerates and/or changes direction, the particle loses its kinetic energy, which is converted into a photon ("*Bremsstrahlung*"). The photonic approach also has a limitation in that it fails to approach the THz regime due to the atomic structure of materials. Energy levels of the atomic structure are discrete, and electrons only exist at the given energy level. However, most materials do not the have energy level differences required to generate THz radiation. Because the required energy gap for THz radiation is too small (e.g., 30 THz = 0.12

eV), it is hard to control the electron movements between two different energy levels to release the desired range of THz frequency. To resolve this issue, one can lower the temperature by limiting the electron movement. However, this would decrease energy conversion efficiency, and also result in more practical drawbacks involving extra costs for cryogenic systems and more space.

Improvements in photonics/laser technology provided a clue to reduce the gap [197–200]. From intense laser-induced plasma, certain electromagnetic waves can be irradiated. Early laser technology, however, did not provide short enough pulse duration to generate THz waves for the THz gap. Since the 1980s, a modern laser technology has been advanced in various ways. For example, a self-mode-locked femtosecond pulse duration laser system [38, 201] narrowed one end of the gap. Since Hamster *et al.* first reported THz wave generation from intense laser-plasma interaction in air [101, 202, 203], laser-plasma based THz sources have been the subject of intense research in the field. The method of using a laser induced plasma as a medium has been highlighted because plasma can be used at intensities well above the damage threshold of nonlinear crystals or semiconductors. Over the last two decades, investigators have shown that including a second harmonic signal in the driving laser field (known as 'two-color mixing' method) can enhance THz generation [103, 204–210]. Recently, Xie *et al.* [206] delivered frequency-doubled beams (2ω) in a time delay with respect to the original pulse beam (ω), and Peng *et al.* [211] also used an adjustable aperture to tailor the Gaussian beam to obtain enhanced THz radiation. Another study showed that the energy conversion efficiency of the second harmonic method could be improved using a cylindrical lens [212]. This changes the focal spot and the shape of the filament, improving the structure of the photocurrent within the filament as well as the controllability of the radiation pattern and generation efficiency. For these two-color techniques, the fundamental field and its second harmonic are viewed as being mixed in air, producing a directional current that drives

THz radiation within the timescale of the laser pulse [103]. The spectral extent of the directional current depends on the original spatio-temporal laser fields, which means that the radiated THz spectrum can be modified by manipulating the laser pulse using adaptive optics. While adaptive optics is new to the generation of strong THz radiation, it has been widely used for improving optical systems degraded by environmental effects [135, 136]. Numerous laser-driven plasma sources have employed GA to optimize the desired outcomes [140, 213, 214]. In this chapter, therefore, the generation of THz radiation from laser-filamentation and the optimization of THz are reported from a few millijoules of ultrashort laser pulses are focused in air.

5.2 THz generation theory

Following Hamster *et al.* [101, 203], a laser-induced plasma has been widely used for generating a strong THz radiation. A plasma wake excitation mechanism was introduced to explain the generation mechanism of THz [202]. In this model, the ponderomotive force induced by an intense laser pulse results in the production of a plasma wave that generates strong THz electromagnetic radiation. Recently, from a Laser Wakefield Accelerator (LWFA), THz has been reported [30, 31] and Coherent Transition Radiation (CTR) was proposed as the mechanism. When the electron propagates through the plasma-vacuum interface generated by the LWFA, it emits transition radiation. This radiation then interferes coherently for wavelengths longer than the electron bunch length. More details of the mechanism are described in Ref. [31].

In this section, THz generation theories will be reviewed; however, out of these, we specifically examine the theories related to the second harmonic method. To enhance the THz radiation for lower levels of input laser energy (< 1mJ), a frequency-doubled beam was introduced to the fundamental beam. This second harmonic method can enhance THz generation by more than 100 times [102]. A number of studies using

the second harmonic method have revealed other THz generation mechanisms [103, 204–208, 210]. Among many suggested theories, the two most well-known are the four-wave mixing model [102, 204–206] and the photocurrent model [103, 208, 215, 216]. Recently, many studies have shown that broadband THz spectra generated by the second harmonic method have multiple origins depending on their frequency range [210, 217–219]. In the low frequency region (1 THz to 5 THz), the free-electron photocurrent is the major contribution to THz radiation. As the frequency increases beyond 5 THz, the Kerr nonlinear response of the neutral molecules, which is related to four wave mixing, dominates.

5.2.1 Four-wave mixing model

FWM is one of the nonlinear effects due to 3rd order optical nonlinearity ($\chi^{(3)}$). The three input beams' frequencies ($2\omega, -\omega, -\omega$) add to nearly zero, and yield a 4th frequency. In the THz generation process from pulsed laser system, fundamental (ω) and its second harmonic (2ω) fields will interacts in a nonlinear medium (i.e., plasma) generating THz radiations by $\chi^{(3)}(\Omega_{THz} : 2\omega + \Omega_{THz}, -\omega, -\omega)$. From the four wave mixing theory, a generated THz field is given by [102]

$$E_{THz} \propto \chi^{(3)} E_{2\omega}\, E_{\omega}\, E_{\omega}\, cos(\theta) \tag{5.1}$$

where θ is the phase difference between a fundamental and its second harmonic fields. To prove the model, there have been many efforts. As shown in Eqn. 5.1, THz fields are subject to two input field strengths and their phase difference. The nonlinearity ($\chi^{(3)}$) is a very critical factor in the model and the value is changed by polarizations ($\chi^{(3)}{}_{\Omega,2\omega,\omega,\omega}$). Many experimental studies have examined THz generation by controlling polarization, phase and amplitude of input fields ($\omega, 2\omega$) [102, 204–206]. However, the four wave mixing theory based on the third order nonlinearity ($\chi^{(3)}_{\text{ions}}$

or/and $\chi^{(3)}_{\text{free electrons}}$), cannot explain the observed THz field because these nonlinearities are too small to explain the THz field strength [204].

5.2.2 Photocurrent model

The photocurrent model is proposed by Kim *et al.* [103, 208, 220]. When the strong electric field is applied by a single-color laser, the bound electrons of air molecules are liberated and oscillate along the laser field. Although these liberated electrons drifted away from ions, these electrons could not produce a directional current because of their symmetric drift from the single-color laser field. In case of two-color method, however, a non-vanishing directional current can be generated. The non-vanishing directional current can be shown by the asymmetry of the combined laser field (E_L).

$$E_L(t) = E_\omega \cos(\omega t) + E_{2\omega} \cos(2\omega t + \theta) \tag{5.2}$$

where E_ω and $E_{2\omega}$ are the amplitudes of the fundamental (ω) and the second harmonic (2ω) fields, respectively, and θ is the relative phase between ω and 2ω fields at the focus. As shown in Fig. 5.2, the combined laser fields (E_L) have different average fields depending on phase differences (θ), and corresponding electron drift velocities are plotted in Fig. 5.3.

The local plasma current density is given by

$$J(t) = -\int e v_d(t, t') dN_e(t') \tag{5.3}$$

where $dN(t')$ is the free electrons density produced by the laser field in the interval between t' and $t' + dt'$, and $v_d(t, t')$ is the electron drift velocity at t.

Because the ionization occurs near the peak of the laser field, only the the electron drift velocity near the peak would contribute to the overall electron current. In contrast to the $\theta = 0$ case, there is a net electron current with $\theta = \pi/2$. This net

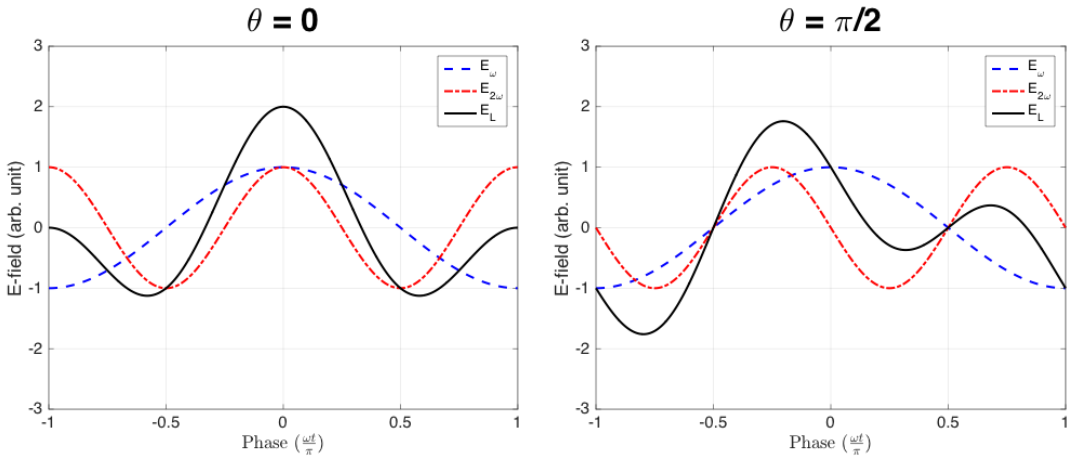

Figure 5.2 Fundamental (ω), second harmonic (2ω) and combined laser fields over one cycle of period with phase difference of (left) θ=0 and (right) θ=$\pi/2$

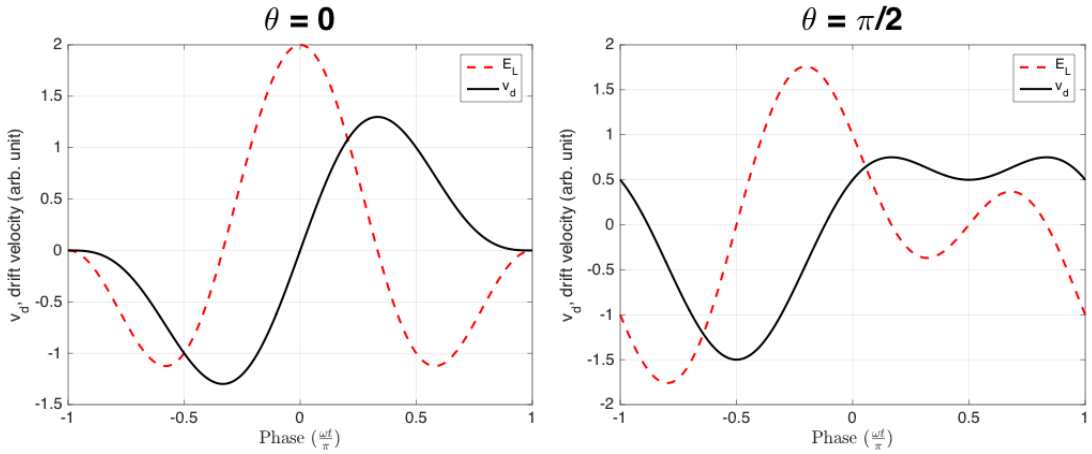

Figure 5.3 Free electron drift velocity (v_d) as a function of time with the combined laser field.

current over the entire laser field envelope produces a directional current surge which emits radiation. If the laser pulse duration is below 100 fs, this process can generate radiation, of which the frequency is between 1 and 10 THz.

5.3 Optimization experiment

5.3.1 Experiment setup

The experiments were performed using the Lambda-Cubed (λ^3) laser facility at the University of Michigan. Section 3.1.1 described the λ^3 system in detail. GA,

using the THz signal as a figure of merit, tested and optimized the mirror figure to achieve higher THz signals. The λ^3 laser delivered 1 to 12 mJ pulses onto a 0.1 mm thick Beta Barium Borate (BBO) frequency-doubling crystal to produce the asymmetric laser field required for the two-color THz radiation generation method. The laser pulses were focused by an $f/15$ lens to an interaction point where plasma filaments are generated, 25 cm behind a BBO crystal. A silicon window of thickness 5 mm filtered the two laser fields (800 nm and 400 nm), allowing only the THz field to pass. The THz field was subsequently collimated by an $f/6$, 90° parabolic reflector. It was relayed by a pair of parabolic mirrors to a Michelson interferometer and was refocused by a final parabolic mirror onto a pyroelectric detector (Gentec-EO, QS-IL). A commercial nitrocellulose pellicle (Thorlabs BP245B2) was used as a beam splitter. The experimental configuration is shown in Fig. 5.4. While Laser

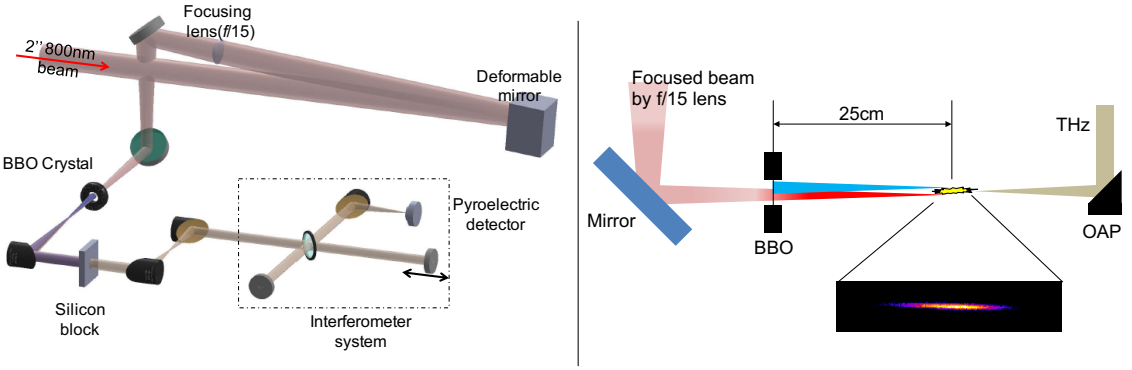

Figure 5.4 (Left) The experimental setup including a DM. The DM is controlled by a computer with the LabVIEW software. (Right) Corrected beam (800 nm, red in the figure) is focused by $f/15$ lens. To generated 400 nm beam (blue in the figure), a BBO crystal is located at 25 cm before the geometric focus.

pulses reach to the BBO crystal, laser wavefront experienced distortions due to air turbulence and optical imperfections. To compensate for these distortions and also to optimize the THz yield, the 47 mm of the input beam first impinged on a DM and then focused via the $f/15$ lens to generate plasma filaments. To find the best THz yielding mirror shape, wavefront distortions caused by air flow or imperfections on

optics must be corrected. Note that the correction procedure may include not only eliminating unwanted wavefront distortions, but also adding desired imperfections.

A computer controlled translation stage with 0.1 μm step size was used to scan the Michelson interferometer to determine the THz spectrum by Fourier Transform Spectroscopy. In the interferometric measurements, we experienced a signal variation due to acoustic effects, because the air-breakdown causes an acoustic signal that vibrates the pellicle. During optimization, the acoustic signal level varied slightly for each mirror shape generated by the genetic algorithm. To reduce the signal variation, a box was built around the interferometer to limit the vibration. We also enclosed the THz generation region in a foam tube to minimize microphonic effects in the pyroelectric detector.

5.3.2 Optimization process

At the beginning of the experiment, all 37 actuators are set to 0 V, i.e., relatively flat mirror shape for manual alignment (to have the best focus). When the genetic algorithm starts to optimize the output signal, the system applies 30 V to all actuators and "mutates" each actuator voltage from the that setting. More details of optimization process (GA) was descried in Sec. 3.3.2.

Figure 5.5 shows the signal improvement through 41 generations for 1.2 mJ of incident energy. The x-axis represents the generation of the GA, and the y-axis shows the signal relative to the starting point. In Fig. 5.5, there are the 10 best "offspring" for each generation. For the 1st generation, the 10 results were the mutations of the 30 V parents. Because GA has no preference for mutations, the first 10 mutations can generate both favorable mirror shapes and worse mirror shapes. Therefore, the initial results also show lower-than-unity FOM values (0.15 to 0.91). But, after the 1st generation, the GA proceeded to find better results with consistent improvement. After the 41st generation, the maximum signal was 2.4 times higher than the FOM

of the original 30 V mutations. This performance was consistent from run to run, though the particular mirror shapes were not necessarily repeated. For the THz yield, we obtained a 5.6 mV signal with the best output mirror shape, which corresponds to a 2.4 times improvement in THz yield relative to the 30 V mirror shape (2.3 mV). The same level of THz signal improvement were produced months later, from the same setup: measuring 2.1 mV (30 V mirror) and 5.1 mV (the optimized mirror) respectively. Repeating experiment with a 3 mJ incident energy, we obtained 4.8 times improvement.

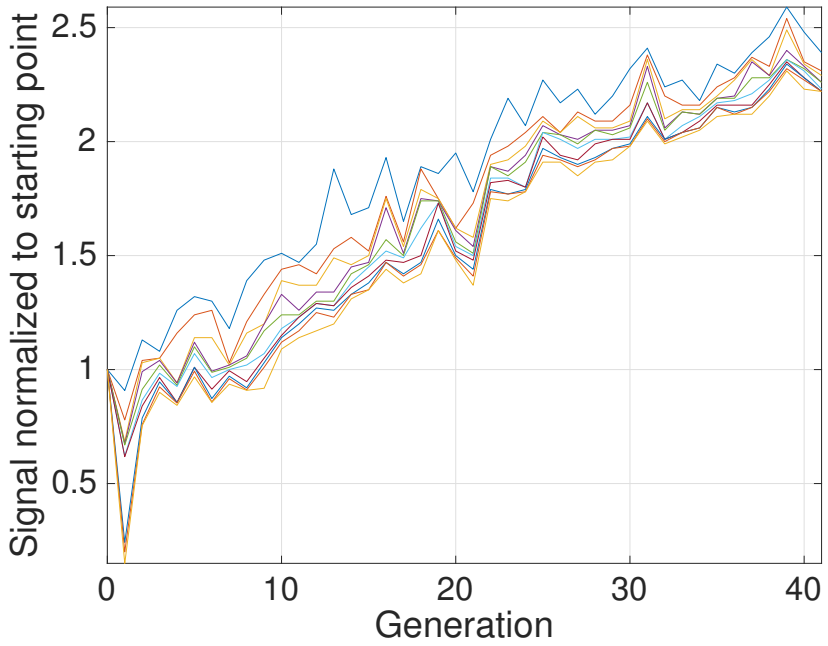

Figure 5.5 Signal improvement through 41 generations for 1.2 mJ incident pulse energy.

5.3.3 THz detection and spectral analysis

From the Michelson interferometry of the THz radiation, spectral analysis using a Fourier transform spectroscopy was conducted. In Fig. 5.6, the red lines show the interferogram and spectrum prior to optimization, and the blue lines show the results with the optimized mirror shape. The peak-to-valley difference in the interferogram

increased from 3.4 mV to 5.8 mV, and the bottom graph showed the THz spectrum improvement from 1 THz to 70 THz, with the signal doubling between 5 THz and 40 THz. In these frequency ranges, the generation of THz was affected by four wave mixing theory, indicating that our system improved the THz yields by modifying the Kerr nonlinear response of the neutral molecules. Note that for the low frequency range (<5 THz), there is strong attenuation due to water vapor in the air [221].

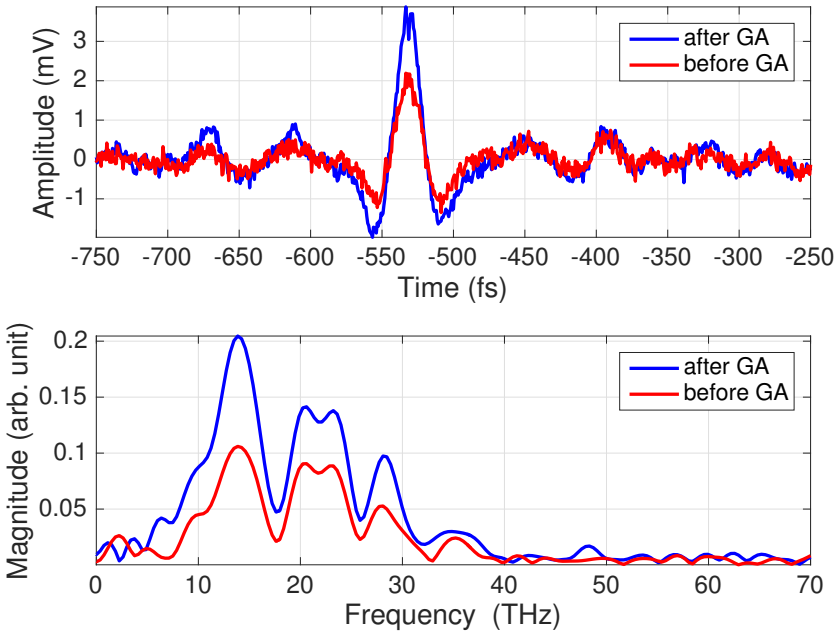

Figure 5.6 (Top) Two interferograms before(red)/after(blue) optimization (Bottom) Spectrum analysis.

We also characterize the THz yield with varying input pulse energy under different conditions (see Fig. 5.7). The THz field was detected by a pyroelectric detector after passing by a silicon window and the Michelson interferometer. The calibrated detector sensitivity was 3.7×10^5 V/J. The maximum measured THz signal was found to be 260 nJ per pulse with a conversion efficiency of 0.004 %.

There are two main experimental factors for determining the THz yield: 1) the use of the BBO crystal, 2) the optimization through the GA. Ideally, an optimization would be done at the desired laser energy. However, the random mirror shapes

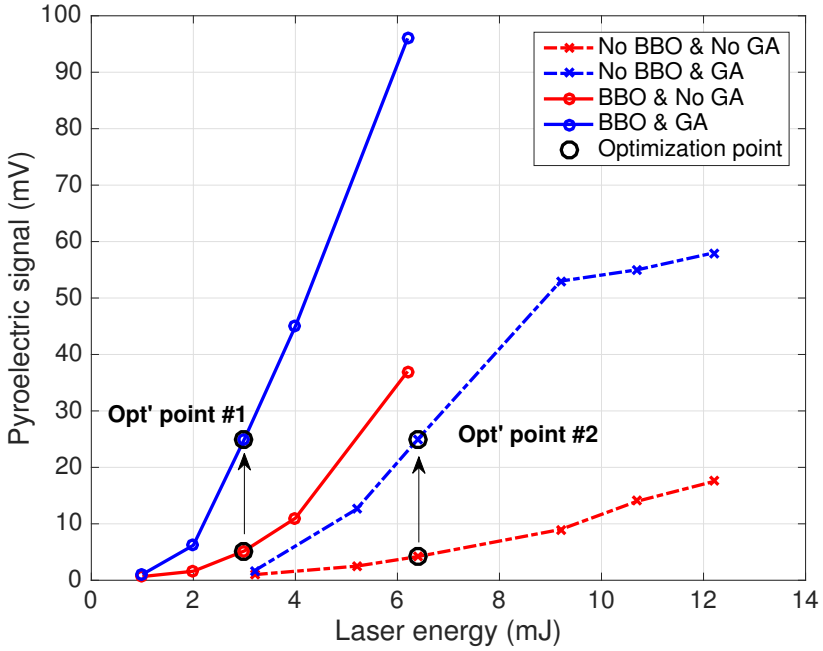

Figure 5.7 THz energy measurements with a pyroelectric detector. THz emission is measured at different situations. Dotted lines represent single-color results and solid lines show two-color results. Red and Blue color represent before/after optimization results, respectively. For the two-color case (Optimization point #1), optimization process was done at 3 mJ, and it required 99 generations, and 6.2 mJ and 47 generations for the single-color case (Optimization point #2). Note that the pyroelectric detector sensitivity was 3.7×10^5 V/J. The maximum THz energy was 260 nJ per pulse with an input energy of 6.2 mJ, resulting in the conversion efficiency of 0.004 %.

generated during the GA could make hotspots on the beam profile, causing damage on the BBO crystal. To avoid damage, the optimization process was done at a lower energy (3 mJ, optimization point #1 in Fig. 5.7), then, the resulting mirror shape was applied to generate THz radiation at higher energies. In this experiment, the THz signal increased a five-fold as a result of optimization, retaining greater than a three-fold improvement between energy levels 2 mJ to 6.2 mJ. Without the BBO crystal, damage is no longer a consideration, and the optimization process can be done with moderate incident energies (e.g. 6.4 mJ, optimization point #2 in Fig. 5.7) and the resulting mirror shape is applied to other energy levels showing the scalability of the solution. In the single-color case (without the BBO), the THz generation mechanism is different than two-color case. The source of the far-field THz radiation is the set of plasma waves generated due to the propagation of the laser through the atmosphere [101, 203]. Thus, the THz emission we optimized using the single-color method is likely due to the optimization of the plasma wave amplitude. This mechanism is more dependent on having the correct temporal pulse shape, and also having a focal spot similar in dimensions to the relativistic plasma wavelength. The relativistic plasma wavelength is a function of the electron density which is determined by the laser intensity. The amplitude of the plasma wave can also be improved if there are temporal structures in the driving laser pulse which are less than the plasma period. So the focal spot and the electron density are connected in a complicated way that also depends on pulse energy. Note that the temporal shape of the laser pulse is also affected by the filamentation process [222]. Thus, the shape of the plasma wave which optimizes the THz generation for the single-color method is not the same as that for the second harmonic method, and in these experiments, the optimized phase front of the single-color case is clearly different than that of the two-color case.

Figure 5.8 shows four optimized mirror shape illustrations for different THz generation mechanisms and pulse energies. It is clear that these mirror shapes will produce

different focal spot structures. However, it should be noted that for the same pulse energy and generation mechanism, although the precise mirror shape may differ from experiment to experiment, the amount of THz produced after mirror optimization is generally reproducible. Using the two-color method, diagonal voltage patterns are observed on the deformable mirror which cause the mirror to form a slightly cylindrical shape, thus generating a slight "line-focus" (see Fig. 5.8 (c) and (d)).

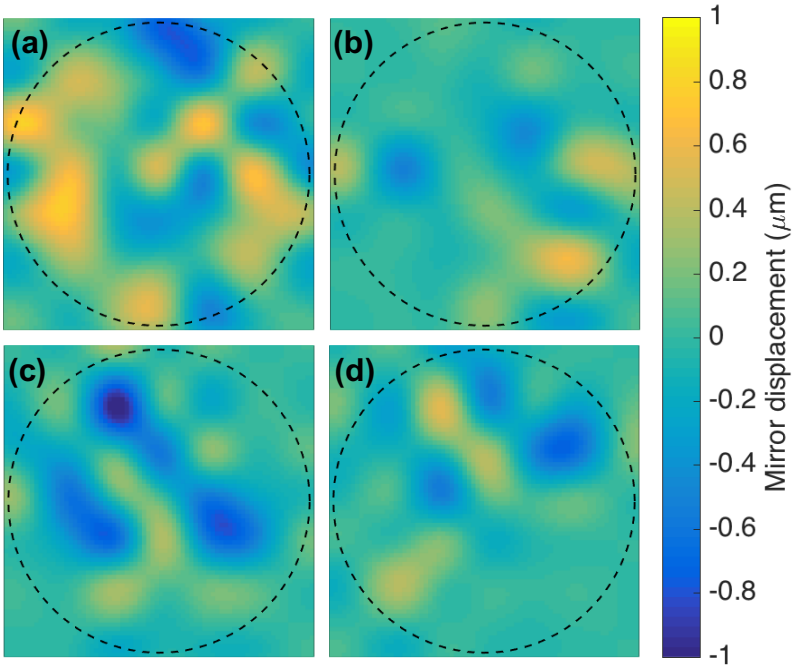

Figure 5.8 Various result mirror shape illustrations from different optimization conditions. The images are reconstructed from the applied voltage on electrostrictive actuators. (a) Single-color at 3mJ, (b) single-color at 6mJ, (c) two-color at 1.2mJ, and (d) two-color at 3mJ.

This focal spot structure is also not along the direction of laser polarization. By contrast, in the single-color case (without the BBO crystal), no distinct patterns of mirror deformation emerge. This suggests that a more complex and larger focal spot is produced such that the path lengths from various parts of the beam may result in pulse modulations. From these mirror shapes, it is clear that the presence of the BBO crystal has changed the wavefront of the optimized laser pulses significantly which results from optimization for a different THz generation mechanism. It is also clear

that the focal spot structure that optimizes the THz production for a particular energy is not the same as that which optimizes THz production at other pulse energies. This is precisely because of the complex 3D self-focusing and diffraction effects involved in the filamentation process. As the energy of the pulse is increased, the amount of mirror deformation required for optimum THz enhancement is reduced even though the amount of THz enhancement is similar as at lower energies. This is likely to be because the amount of asymmetry in the focal spot required to "seed" a particular filamentary structure is reduced at higher energies.

Figure 5.9 shows beam images from the two-color case, which were taken at the location of the BBO crystal. (a) is the cross-section image of the 0 V mirror (i.e., relatively flat mirror) and (b) is that of optimized mirror. Compared to (a), the intensity of (b) is lowered in its central region and higher on the lower right side. The right panel of Fig. 5.9 shows applied voltages on the deformable mirror for the best result and the voltage patterns on the mirror indicate that the focal spot is elongated. The best result does not have a specific geometric shape such as tip/tilt or focus/defocus, because it was identified via by selectively testing the various mirror figures applied by the GA. Also, changes in plasma filamentation are observed during

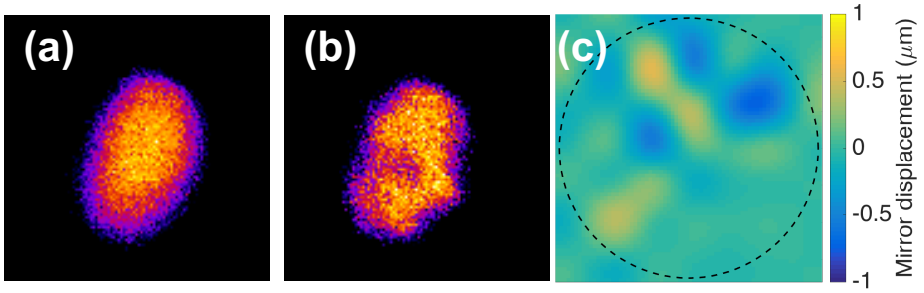

Figure 5.9 Beam cross-section image (a) before GA, and (b) after GA. (c) Optimized mirror shape generating the highest THz yield from two-color method after 75 generations. The deformable mirror with voltage distribution (c) changed the beam cross-section from (a) to (b)

optimization. Figure 5.10 shows that the length of the filament doubles and total light emission from filament decreases more than 3 times, denoting larger plasma

volumes. The larger plasma volume is known to generate stronger THz signals [223, 224]. Because the laser wavefront experiences great modifications through the plasma filaments, such variations of plasma filament characteristics are the key to understand THz generation from the laser plasma interaction.

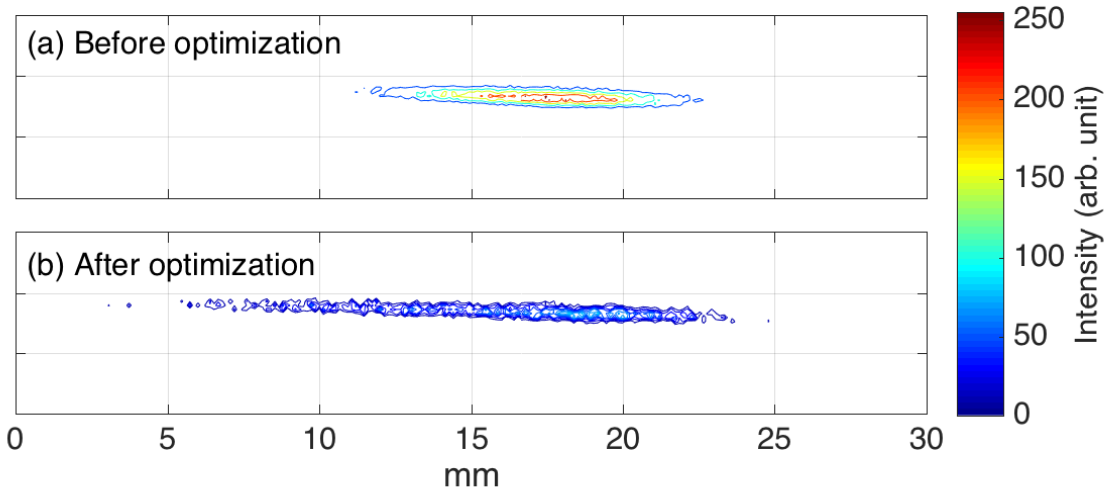

Figure 5.10 Plasma filament images, (a) before and (b) after optimization with 1.6 mJ laser input energy. The length of filament is doubled and its intensity decreases. As laser input energy increases, filament length increases up to 100 mm.

Taken together, these results indicate that our active feedback system optimized the mirror figure for enhanced THz generation correcting for defects in the whole optical system. This includes imperfections such as air turbulence and accounts for the details of the phase figure needed to maximize the THz generation via Kerr effects. Here, the optimal mirror shape was the best *time-averaged* figure for THz generation in the presence of air turbulence. This differs from astronomical applications which offer *real-time corrections* for air turbulence.

5.4 THz optimization with radiation source

Up to now, the THz generation and its optimization using DM was examined. From the analysis of filament characteristics (see Figs. 5.9 and 5.10), it was re-

vealed that the THz yield is closely related to the filament generation. If a stable predictable plasma filament can contain information regarding the ionization state of the surrounding air, then one expects that SNM identification could be realized with more confidence. The small volume occupied by the plasma filament (3 cm long and 150 μm in diameter) can be integrated over some time to observe any effect from sparse ionization.

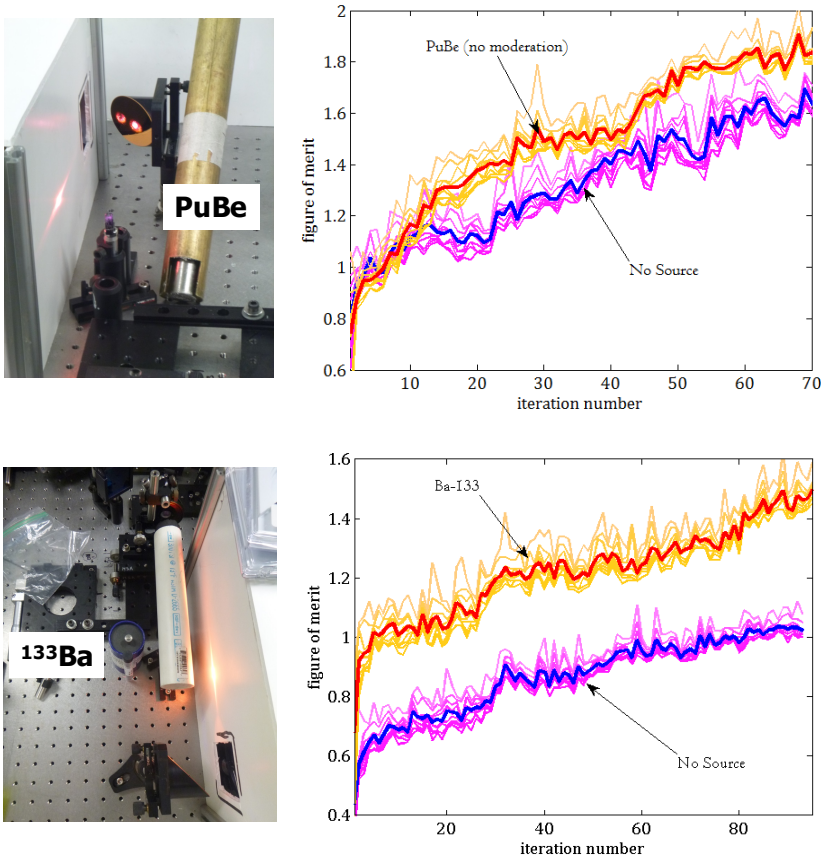

Figure 5.11 (Top) Optimization of the THz signal with/without PuBe neutron source. (Bottom) Optimization of the THz signal with/without ^{133}Ba gamma source

One set of experiments was to measure if the signal derived from the pyroelectric detect was modified by the presence of radiation. As the radiation source, 1 Ci of ^{239}PuBe for neutron and 2 mCi of ^{133}Ba for gamma were used, respectively. Each radiation source was located next to the filament (see Fig. 5.11). The one should

recognize that it have not been confirmed that the variation was due to air ionization alone, because it may be due the slightly altered geometry due to the presence of the source. Regardless, it was evident that the THz signal is highly sensitive to the immediate environment about the plasma filament source. Using the amplitude of the collected signal by the pyroelectric detector as the FOM to be maximized, the each optimization result was shown in Fig. 5.11.

In this section, the THz generation with the presence of radiation sources was examined. The next step with the THz experiment could be examination for the extent to which the plasma filament is sensitive to various ion concentrations. As mentioned above, THz signals are non-ideal carriers of ranged information due to water-absorption in air. Now that we have deployed the beam optimization system for the THz experiment, we would also utilize the technique for the ns-derived plasma pulses in Chapter VI.

5.5 Conclusion and future works

In summary, an active wavefront correction was made to improve the output of the THz radiation in air. The correction was controlled by a genetic algorithm and made by a deformable mirror. The distorted wavefront resulting from air turbulence or defects of the optical components was compensated by a deformable mirror figure obtained by the genetic algorithm. The method found the optimal spatial-phase configuration of the fundamental light for the generation of THz radiation, which would be impossible to obtain analytically. This included implicit manipulation of the phase configuration of both the fundamental and the second harmonic fields, and it yielded a significant enhancement in the THz radiation. With the optimal mirror shape on the deformable mirror, the THz signal amplitudes can be improved by 2 to 6 times compared to that before optimization. Using the feedback method, it shows the possibility of optimization on different THz configurations even though the

generation mechanisms are different and unclear. The optimized phase front for the two-color source is not the same as the optimized phase front for the single color source. Using this technique, one could also optimize the THz signal in a particular wavelength range by controlling the different THz generation mechanisms separately by the advantage of adaptive optics and the feedback system. Additionally, by locating anexternal radiation source near the filament, the change of the optimization precess was examined. It showed that the laser-induced filaments sensitively react to the radiation source yielding more THz radiation as a result. Because the origin of THz is still veiled, it is hard to conclude how the radiation sources result in higher yields of THz or other electromagnetic radiation; however, the experiment shows a possible fs-laser based SNM detection methods [225].

CHAPTER VI

SNM detection using ns-laser

6.1 Introduction

Due to increased threats of national security, the detection of illicit SNM becomes more important. Even though passive detection methods may work for some cases, radiation from SNMs, for instance HEU which has a low neutron emission rate and weak gamma, can be easily shielded. To resolve the problem, active interrogation methods can be applied. The active interrogation can increase the detection probability of shielded materials via induced fission reactions, providing some advantages compared to the passive way. By adjusting an interrogation energy, one can generate different responses from different SNMs, and also map possible shielded areas consisting of high density or high-Z materials from the responses. For these reasons, the active interrogation techniques are intensively studied and already adopted for actual applications [226, 227].

In this chapter, a novel SNM detection technique using a ns-laser system is reported. Compared to other active interrogation methods, the technique interrogates air molecules excited by SNM, rather than SNM itself. A pulsed laser delivers a sufficient electric field to induce a collisional cascade of radiation sources that is intensified by residual ionization and free electron density. The collisional cascade results in plasma spark, which emits strong light and is able to detect at long range. Thus,

a laser can be used as a radiation detector when the laser pulse encounters radiation-induced ionization or is intersected by the impinging radiation-induced charge track. For this study, a Q-switched Nd:YAG laser is employed and the conditions for a highly selective signature of the presence of radiation-induced ionization will be studied. In order to obtain a radiation-sensitive beam shape, a wavefront correction is applied to the system. From a practical view of deploying the device, an effect of aerosol- or dust-initiated plasma is statically analyzed.

The author wants to note that the work described in this chapter is a partial study of "Active Detection Of Fissile Materials Via Laser-Induced Ionization-Seeded Plasmas" funded by the Defense Threat Reduction Agency (DTRA). This chapter includes the research conducted during Phase II to V. However, some previous work by the group was introduced to provide background and progress before Phase II.

6.1.1 SNM detection using laser-induced plasma

Compared to typical active interrogation sources such as gamma-rays, X-rays, and neutrons, the laser pulse, of which wavelength falls in near IR, has more than 1000 times lower energy level and it is impossible to cause a fission reaction. When the laser pulse, however, is focused, it can introduce strong E-field to initiate breakdown phenomena. If the laser can be used as an active interrogation source, it has two advantages for long-range detection especially. The laser easily delivers the pulse to the target using optics. In contrast to other interrogation sources, it has no ionizing power until it is focused enough. The resultant is a very bright optical emission, i.e., breakdown plasma, which is easily detectable at long distance. The plasma emission spectra contain the key information.

Figure 6.1 shows possible detection architecture of *prove-and-detection*. An airborne-laser system may scan a target area on the ground. When the residual ionization or free electrons from the SNM intersects the region above the collisional cascading

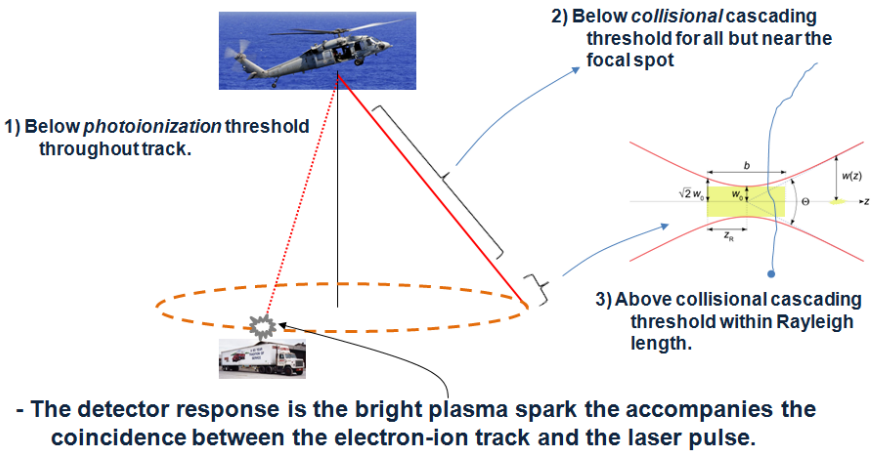

Figure 6.1 Illustration of *probe-and-detect* architecture, in which the laser power is mounted on a vehicle that allows one to scan out to distance on the horizon.

threshold, a bright plasma spark is generated and detected. The laser pulse energy is set so that plasma sparks will only occur: (a) within a Rayleigh length of the laser's focal spot, and (b) if a seed fast-electron (but not an ion) is present. Thus, if the truck contains SNM, then the air ionization near the truck will produce sparks with increased spatial frequency nearest to the source.

Figure 6.2 shows a schematic diagram of the laser waist in which the confocal length, which is twice the Rayleigh range, is shown as $b(= 2z_R)$. For a 10 μCi source placed 1 cm from the focus of the laser (our nominal setup), the rate in intersection with a typical Rayleigh range area is: 206 intersections/s for a 20 cm focal length, or 650 intersections/s for a 35 cm focal length. However, the short pulse duration (a few tens of nanoseconds) of the laser implies that the overlap between the radiation plasma and the high field pulse is improbable. Specifically, the count rate for a 40 μs decay time is 0.03 counts/second, for the long 35 cm focal length, yielding regular counts (i.e., sparks) from the radiation source. However, for the short 20 cm focal length, the small high-field volume results in a single count every 120 seconds, which implies that the counts should be few and far between if driven by intersection between the laser pulse and the radiation-induced electron-ion track.

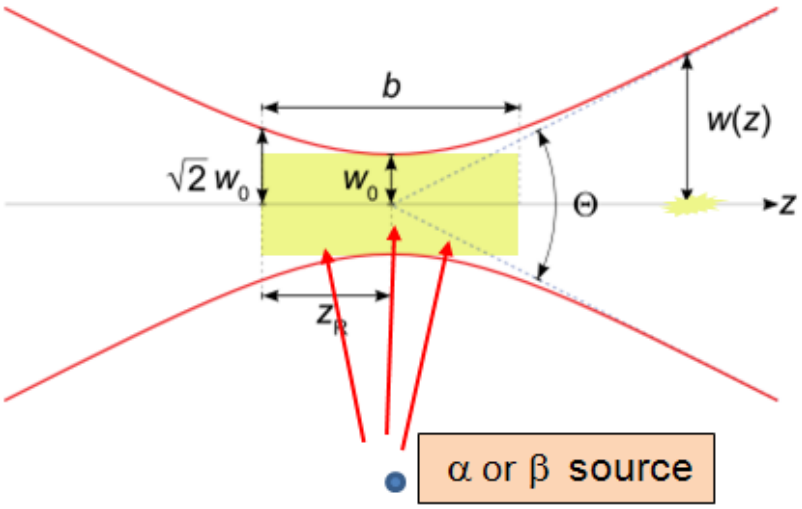

Figure 6.2 The effective volume of the radiation detector, in which the intersection of a radiation-induced charge track within the Rayleigh range, yields air breakdown. z-axis: laser propagation axis, z_R: Rayleigh range $w(z)$: Gaussian beam width as a function of the distance z along the beam, w_0: beam waist, b: depth of focus, Θ : total angular spread

The experiments (see Fig. 6.4) in which the addition of an alpha source causes plasma-spark formation too rapidly to correspond to the coincidence between the laser pulse and charge track - changing from roughly 1 in every 10 laser pulses to 1 in every laser pulse - confirm that the laser channel is not a conventional detector of radiation-induced charge tracks but rather a detector of the local ionization environment. The consequence is that the plasma spark does not provide a direct spectroscopic measure of the radiation, but it does provide a measure of the underlying gamma-ray and neutron spectroscopic distributions through the spatial distribution of the ionization.

6.1.2 Previous work by the Hammig group

As mentioned above, this chapter describes the results from the DTRA basic research project ("Active Detection of Fissile Materials via Laser-Induced Ionization-Seeded Plasmas"). In this section, the previous work conducted during Phase I is described. Figure 6.3 shows the experimental setup to observe laser-induced plasma discharges. The Nd:YAG laser system was used to induce a photoionization from the

radiation-induced tracks. The laser pulse was focused by lens (f = 300 to 1000 mm); laser-induced plasma discharges were detected and counted by a photodiode detector and analyzed by a oscilloscope. The number of plasma formations was counted by photodiode and acoustic detector (to locate the plasmas). The plasma spectra were collected by the standard manufacturer-provided 200 μm core size, 0.22 NA, high OH, 1 m-long fiber (Thorlabs P/N M0065-51-0034), and analyzed by the spectrometer (Thorlabs, CCS200).

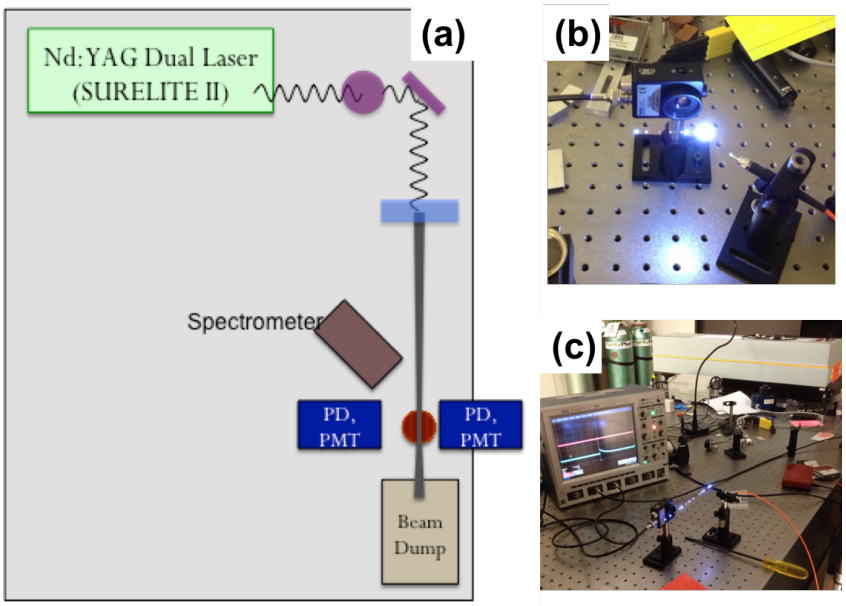

Figure 6.3 (a) Schematic diagram and the images of the laser system setup. Comparison of the plasma discharge region between the (b) f = 300 mm lens system and the (c) f = 1000 mm lens system. One can clearly observe the extended range of breakdown region when the f = 1000 mm lens was used. Optical fiber (orange cable in the (b) and (c)) collects the light emission and delivers to the CCS200 spectrometer.

Figure 6.4 shows the difference between "pristine" air and air-plasmas for which three ^{232}Th disk sources are distributed between 45" and 50". Using the known source activities, the radiation-induced ion concentration is approximately $10^7/\text{cm}^3$ (10^{-3} ppt) and therefore small. Nevertheless, the plasma generation rate increases from 33 counts/min to 190 counts/min, the roughly 5 to 10 times increase that can be typically

observed. However, the laser is producing pulses at a rate of 600 counts/min; thus, the initiation probability is relatively low. Recall that the greatest sensitivity occurs when the laser power is nearest the photoionization threshold. The plasma generation rate can be substantially enhanced by the presence of moderate amounts of radiation. Recall that in principle, nuclear materials can be detected and identified using count rate alone because one can map the ionization distribution near the source, the radial profile of which reveals the emissive make-up of the underlying material.

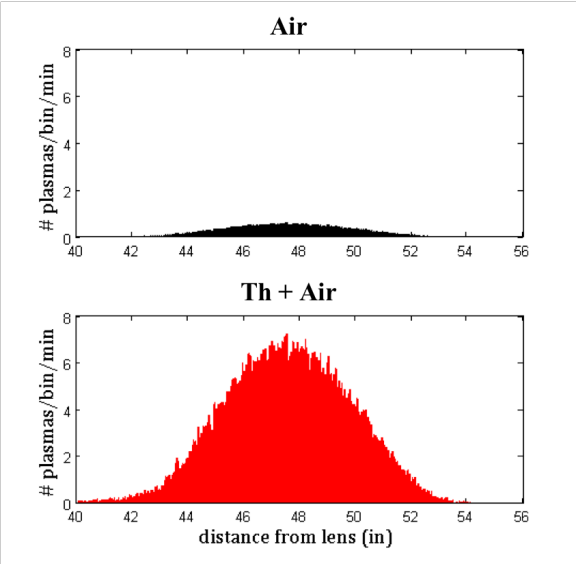

Figure 6.4 Spatial distribution of plasma formation probability as a function of distance from the lens, measured in inches, for the Nd:YAG laser discharging at 1300 V. The measurement periods were 755 minutes.

For a given measurement ("pristine" air vs ^{232}Th modified air), spectra from different locations were compared in Fig. 6.5. The source (^{232}Th) was distributed below the beam axis (47" to 49"). Figure 6.5 presents plasma spectra measured (a) derived above the source (47" to 49") and (b) away from the ionization plume (50" to 56"). As expected, Fig. 6.5 (b) shows that there was a much less noticeable difference in the spectra when measured in the pristine air versus the case in which the ionization density is small. That is because of the limited alpha range away from the radiation sources. Furthermore, the section of the spectra shown in Fig. 6.6 shows that there

were identifiable peaks (around 623 nm) with amplitude modulations compared to the rest of the spectra. In the Fig. 6.6 case, the neutral O I line is suppressed relative to the O II line unless the radiation source is present.

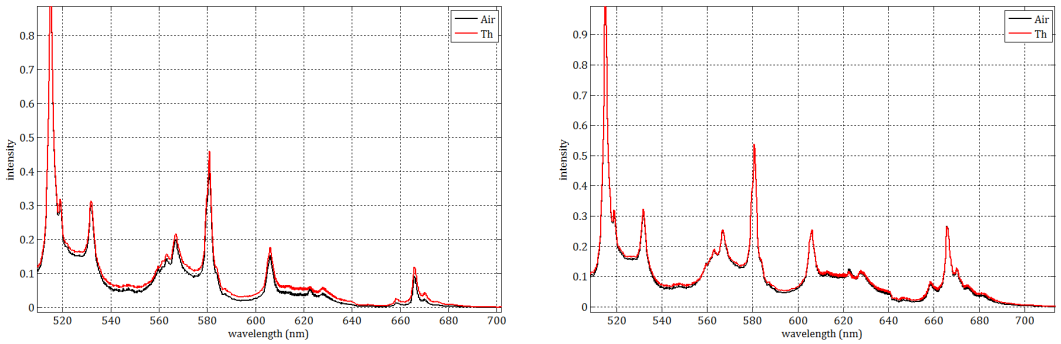

Figure 6.5 The spectra of average plasma compared (black) compared to that derived in the presence of three ^{232}Th disk sources, produced by a beam at 1000 mm focal length operated at 1400 V. (a) Plasma spectra above the alpha sources. (b) Plasma spectra away from alpha sources.

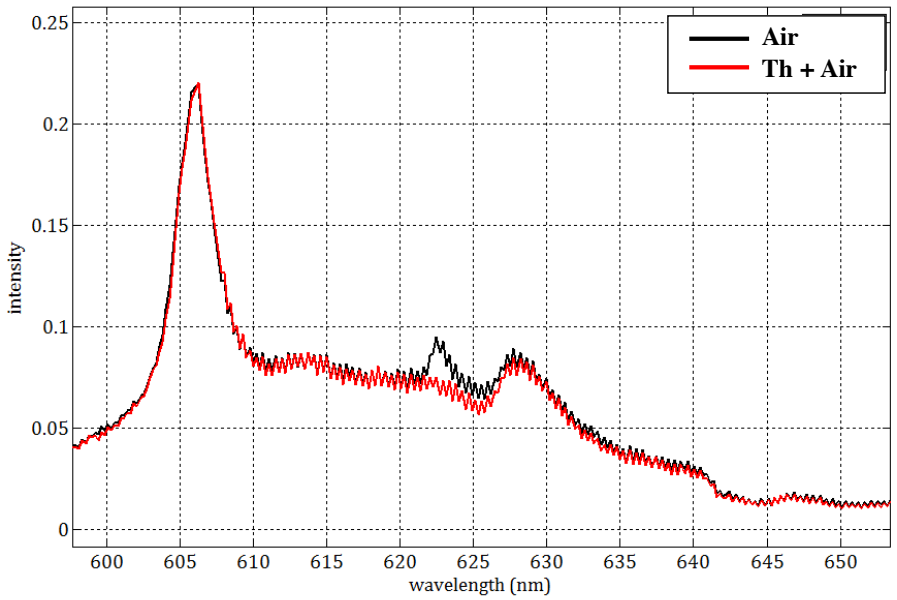

Figure 6.6 The spectra of the average plasma comparing air-plasmas to thorium-modified air-plasmas, with the laser operated at 1300 V and a 1000 mm focal length. Note the suppression of the neutral O I line near 623 nm in the radiation-present case.

Figure 6.7 compares the O I line at 617 nm with the nearby lines produced by ionic atomic species (N II and O II), and shows that the lines from the ionic species increased markedly compared with the neutral line. In general, one interesting feature was found that this line-comparison method was more sensitive as the beam was elongated and photo-ionizing at relatively low laser powers. Based on this, beam shape modification (optimization using DM) will be examined in Sec. 6.2.1.

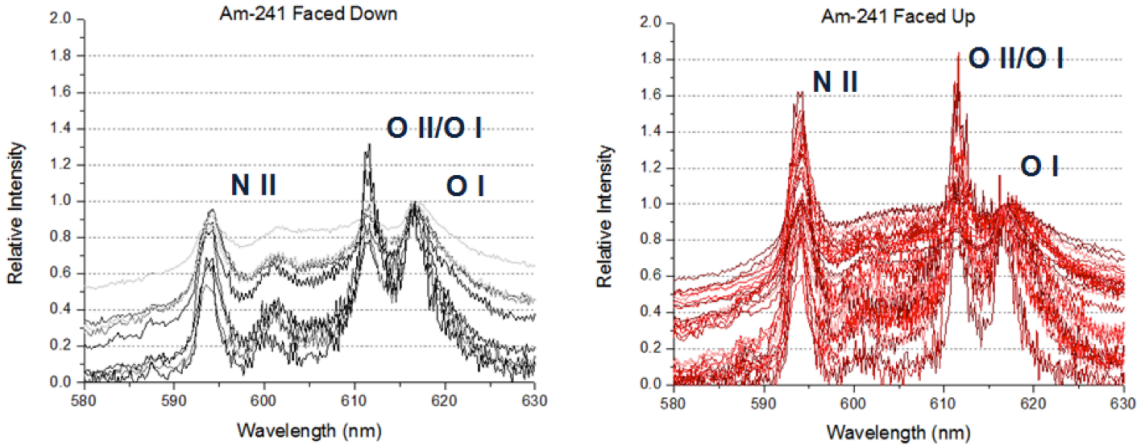

Figure 6.7 Focusing on the 610 nm region, the spectra of air-plasmas produced by an asymmetric beam at 300 mm focal length operated at 1200 V, when discharging (left) in "pristine" air and (right) in air modulated by the presence of an ^{241}Am within a centimeter of the beam waist.

6.2 Experimental setup

The work described in this chapter is the continuing study and partial research of "*Active Detection of Fissile Materials via Laser-Induced Ionization-Seeded Plasmas*" funded by the DTRA. This chapter includes the research conducted during Phase II to V. From Phase I, two interesting results were found: 1) the plasma count rate increases with a radiation source near the focal volume, 2) the line-comparison method can work as a radiation detecting mechanism. The latter finding, it shows that beam shape would affect the ionizations and then make clear better signal-to-noise ratio for line-comparison. Therefore, here, the deformable mirror and genetic algorithm was

applied to find laser pulse shape with higher radiation detection efficiency.

6.2.1 Optimization of SNM detection using adaptive optics

A deformable mirror system is widely used not only in the astronomy field, but also in laser experiments. The details about the deformable mirror system and its operations with a genetic algorithm are already described in Sec. 3.3. The deformable mirror has 47 mm of aperture, and to fully exploit its capability, beam size needs to be matched. The Nd:YAG laser beam output is 7 mm which is the same as one DM actuator spacing; from this small beam, significant compensation of a wavefront is hard to achieve. Therefore, a proper beam telescope (expanding/focusing) system is required. Four lenses were used for beam expanding and re-focusing. The last lens (the latter of the re-focusing lens pair) was actually negative lens to achieve longer focal distance ($\sim$ 2 m). To design the system, a simple gaussian beam propagation was calculated [228] and the results are shown in Table 6.1 and Fig. 6.8. The input laser beam has 7 mm of beam width and 0.5 mrad of divergence. The actual setup had a deformable mirror between lens #2 and #3 (200 mm behind lens #2). Four lenses with proper separations, a 7 mm of initial laser beam expanded and refocused at 2 m from the last lens having $f/55$ system. The exact separation was little modified at the actual system to consider a margin of on the each optics and deflection angle.

Table 6.1 Gaussian beam propagation simulation result. Initial beam has 7 mm beam width and 0.5 mrad of divergence. From given configuration, f-number of the system is about $f/55$.

Lens Element	Lens focal length (mm)	lens separation (mm)	Beam diameter at optics (mm)	Beam divergence (mrad)	focus location(mm)
1	-75	100	7	93.3	-74.99
2	500	375	42.0	9.33	-4499
3	750	750	49.0	56.0	875.0
4	-1000	200	37.8	18.2	2077

The DM was installed with its supporting high voltage supplier, and two detec-

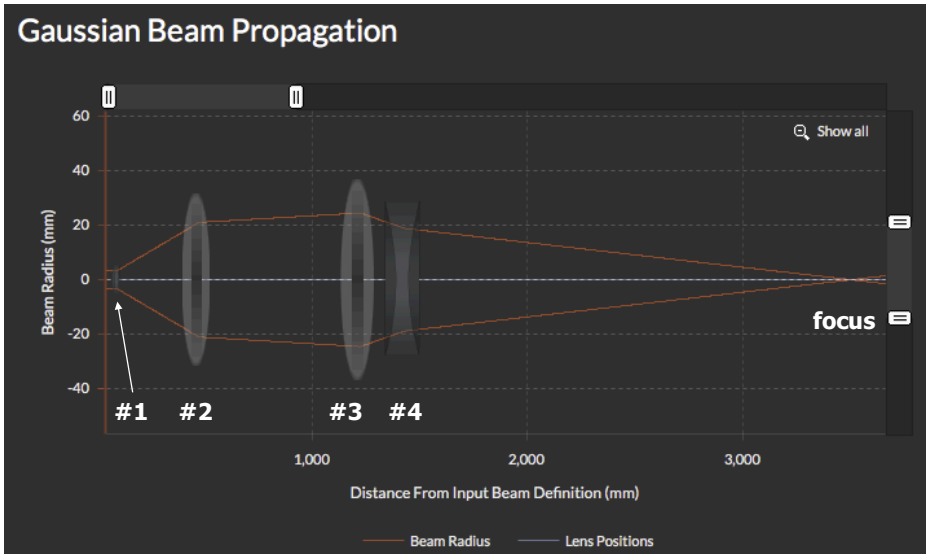

Figure 6.8 Gaussian beam propagation simulation [228].

tors and data acquisition system were included the experimental setup. The final experimental setup for optimizing beam shape is shown in Fig. 6.9.

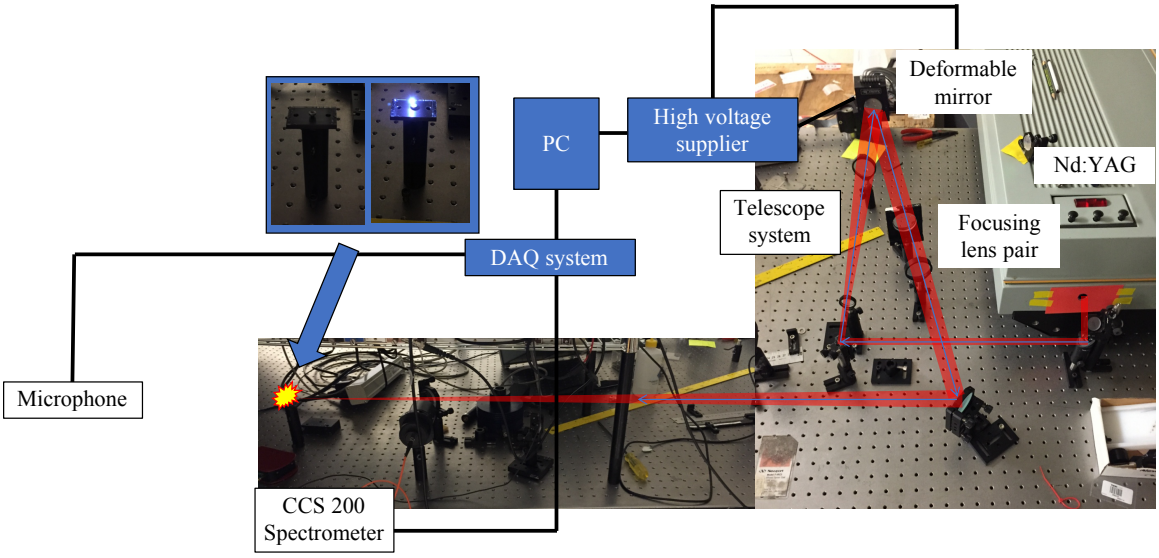

Figure 6.9 Experimental setup for wavefront correction system with the deformable mirror. Beam line is added as red color. The telescope system consists of four lenses to expand/re-focus beam.Two detectors (spectrometer and microphone) were placed to locate plasma and collect its spectrum. The sample was located near focus (1 cm below the focal axis).

The experiment was performed using a Q-switched Nd:YAG laser system(Continuum Surelite II). Its central wavelength is 1064 nm and the laser delivers up to 400 mJ

pulses with τ=7 ns FWHM duration, operating at 10 Hz, into the air. The reflected beam from the DM was focused down by a lens pair ($f/47$) and generates air-breakdown, a plasma spark. Plasma emission light was collected by a CCS 200 spectrometer through a fiber optic. A microphone acoustic detector was located at 0.85m after the focus. These measured (acoustic and spectral) signals were collected by a DAQ device (NI-DAQmx, USB-6343). A control PC collected signals and calculated the FOM values, which indicate how effective a current mirror generates output values. Here, the LabVIEW controls the whole process, including data acquisition and new voltage value generations for different mirror shapes on DM. Also, new voltage values were amplified by a high voltage supplier and applied to the DM.

6.2.2 Detection of dust-initiated plasma

Under a practical operation condition, the aerosol or dust particles can intercept laser beams and cause aerosol- or dust-initiated breakdown instead of air-breakdown that gives radiation-related spectral data. If the radiation signal was driven primarily by the altered charge-states of the *aerosol particles*, a kind of dust detector/imager can be used then extract a nuclear-material signature from the altered dust state in the air. In order to understand the nature of the initiating seed source of the plasma, the aerosol or dust particles imaging system was built (see Fig. 6.10), which was modified from the former optimization setup (Fig. 6.9). The imaging system was spatially and temporally correlated with the Nd:YAG laser pulse so that any particulate seed-sources producing the plasma discharges could be identified. The setup included a 405 nm blue laser-diode as an illumination source, a fast line-camera (The Imaging Source, DMK 23UX174) and associated optics to image both the aerosols and the plasma, and filters utilized to protect the components, principally from the high-intensity 1064 nm light. The laser diode illumination source used a microscope objective to collimate and focus a beam, and it was protected, from the 1064 nm

light, by a band-pass filter (Thorlabs, FGS600). The scatter of the blue light from the aerosols was imaged through a lens array and a filter (Thorlabs, FB405-10) that allowed 40 % transmission at 405 nm, in order to both protect the camera from the breakdown laser pulse at 1064 nm, but to also diminish the photonic loading of the CCD by the broadband plasma breakdown. Even with the filter, the CCD took several milliseconds to recover from the high-intensity splash of photons that accompanied the plasma discharge. The spatial imaging resolution of the system was calibrated and it has the resolution of 15.75 μm per pixel.

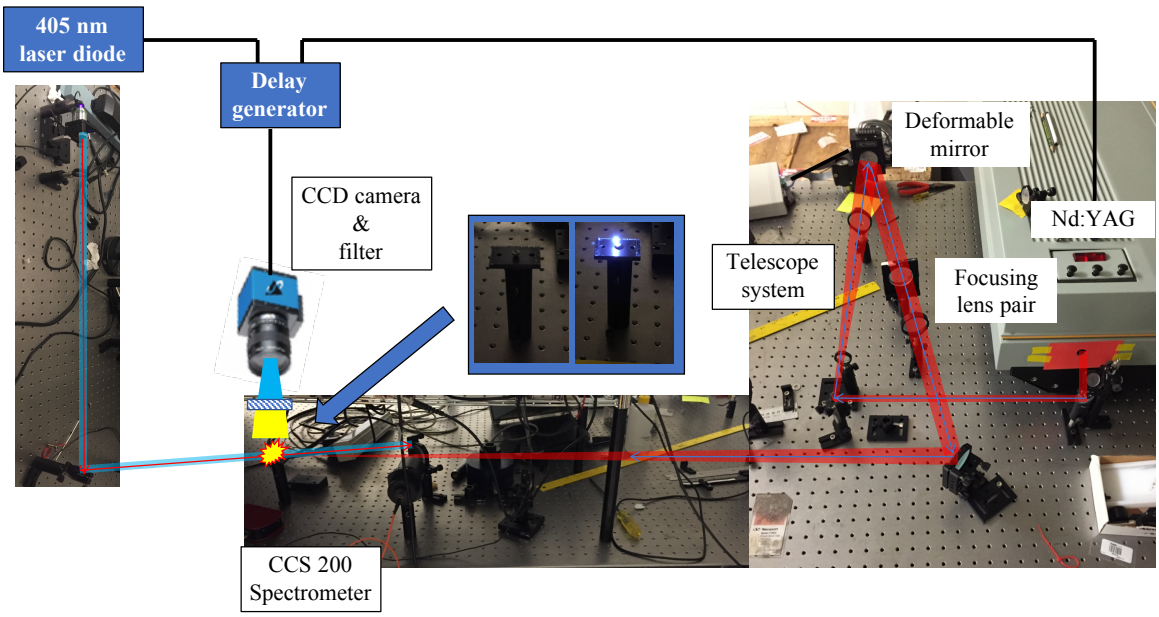

Figure 6.10 Experimental setup for the dust-initiated plasma detection. To image interaction region, a blue laser diode illuminate the interaction region, and its timing is controlled by a delay generator, which is triggered by a laser flashlamp signal.

6.3 Experiment results

6.3.1 Plasma position control

The deformable mirror with the genetic algorithm was employed in the laser system as shown in Fig. 6.9. Using the optimization process, a laser beam was modified

and optimized to have better radiation sensitivity. First, the DM and GA were tested to identify a *controllability* of the plasma by the optimization system. As the simplest characteristic, its position was set as the FOM. To locate the plasma, the time difference between the laser flash lamp signal and the measured acoustic signal was recorded by the DAQ system and the plasma location was calculated. (see Fig. 6.11).

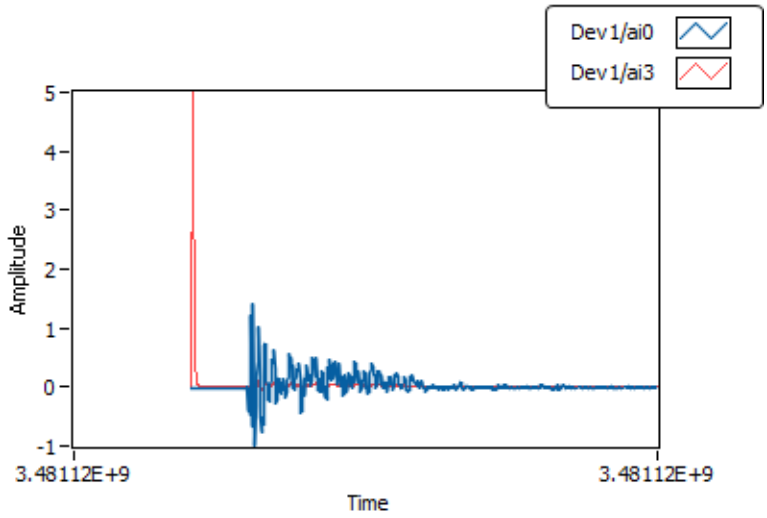

Figure 6.11 An example of time delay between a laser flash lamp and and acoustic signal to calculate plasma position. X-axis shows time axis (PC internal clock). The laser flash lamp signal (red) is recorded first, then acoustic signal (blue) follows after the flash lamp. The time delay gives plasma location.

Although there is also few nanoseconds of time delay between flash lamp and laser pulse arrival time, it is negligible compared to acoustic signal time scale (hundreds of μs to few ms). A microphone acoustic detector, located upstream (i.e., before the focus) of the laser beam, detects an acoustic signal from the air breakdown phenomenon. It should be noted that acoustic detector was located upstream (before the focus), and for other optimization experiment, it was located at downstream as shown in Fig. 6.9.

The data from Fig. 6.12 was collected by placing a solid target on the focus and measuring the histograms of the distributions of time delay. The lateral position along the optical bench was varied in 3 inch steps, from 12" to 30". Since the microphone

was below the laser and plasma plane, these positions were modified to reflect the diagonal distance between the plasma source and the center of the microphone. As shown in Fig. 6.12, there is a systematic offset of 0.5", which indicates a fixed delay in the measurement system which is of no consequence as long as the plasma position is known in this experiment. The important metric from Fig. 6.12 is that the position was measured with high certainty. For instance, for the 13.4" measurement, the standard deviation is 0.14", or 3.5 mm. This few millimeters of uncertainty is sufficient to localize the plasma because the radiation sources of interest are larger than this extent.

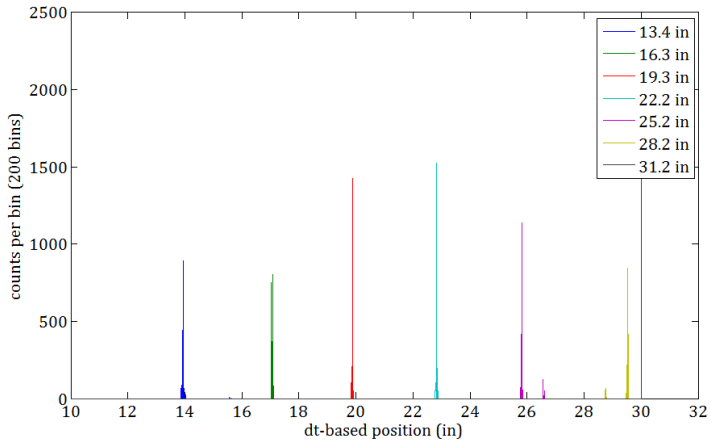

Figure 6.12 A measured spatial resolution of the detection system. A solid target is located generating plasma (optical, acoustic) signals. The target location varies in 3 in steps. There is systematic offset of 0.5 in.

The position of plasma is set to the FOM. Because the GA developed the mirror figures toward having higher FOMs, the optimization will push the plasma away from the microphone detector which cause a higher value of FOM. In Figs 6.13 and 6.14, the results of position optimization are plotted. More than 1200 data points were collected and y-axis represents the relative distance against to system geometric focus. The red line is the calculated moving average of the position. It was calculated from a total 31 data points. From the average line, plasma movement during the optimization process was observed and it moved further from original position about

3 cm, which is more than two times longer than system Rayleigh range (z_r=1.2 cm). As the optimization proceeded, the breakdown position moved toward downstream (i.e., away from the final optics). That meant the system would have longer focal length (higher f-number), and bigger beam width, then focal intensity lowered. As a consequence, the count rate (plasma formation per time) significantly dropped.

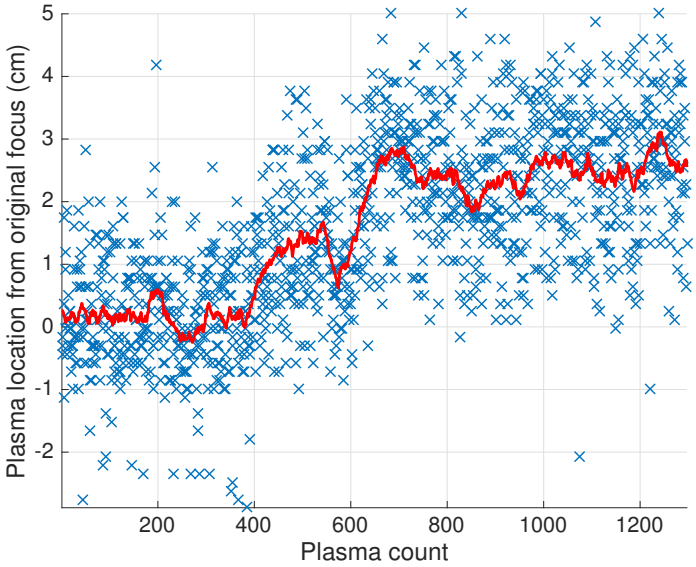

Figure 6.13 Distance optimization results. Through 1300 plasma data, plasma location was moved by about 3 cm. Red line is added to show moving average of 31 plasma locations (before/after 15 data).

In Fig. 6.14, three histograms of the plasma positions are shown. The blue, red, and grey histograms represent the earliest 33 % of the plasma-counts during optimization, the middle 33 %, and last 33 %, respectively, which reflected the temporal evolution of the system. The plasma moved away from the microphone and changed the position by several centimeters, as desired. Ideally, all optical components were aligned with a flat shape on the DM (i.e., all 37 actuators have 0 Volt). When the genetic algorithm applied any other shape except the flat mirror, the system lost the best focus beam alignment resulting in a low plasma count rate. Therefore, the modified results (the grey histogram in Fig. 6.14) required more data acquisition time for the same number of plasma counts. From the results (Figs. 6.13 and 6.14),

it was confirmed that DM working with GA has an ability to control the plasma characteristics.

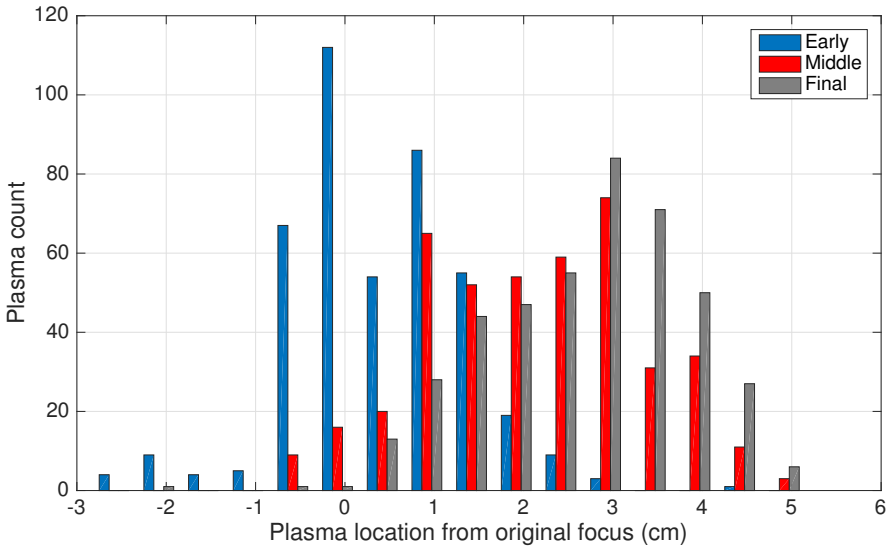

Figure 6.14 A histogram of spatial distribution of plasma.

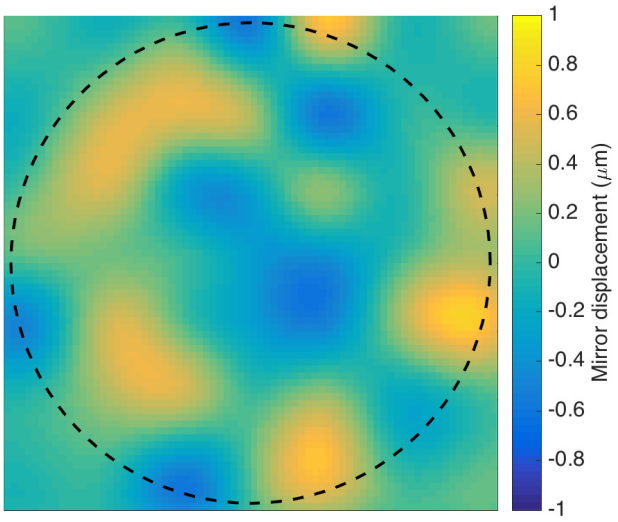

Figure 6.15 The best mirror shape result from the distance optimization. The dotted line is added to show mirror aperture size (diameter of 47 mm).

Figure 6.15 shows mirror displacements on the deformable mirror for the best result and the voltage patterns on the mirror indicated that the outer perimeter of

the mirror was pushed forward and center region was pulled back, having a negative mirror shape on the DM. The negative mirror shape can be expected in delayed plasma positions.

6.3.2 Plasma spectral ratio control

After testing DM (with GA) to control one of the plasma characteristic, the radiation-sensitive beam shape optimization was tested. As an index of radiation-sensitivity, a new FOM should be defined and assigned in GA. A change of surrounding air characteristics due to a presence of SNMs affects many characteristics of the air breakdown plasma such as its count rate, temperature, or ionization order (note: atomic line or 1nd ionization line, NI or NII, etc.). Specifically, an intensity of certain spectral emission lines would be suppressed/enhanced by an extra ionization due to radiation track from SNMs. If the beam profile can be optimized to be more sensitive to the certain spectral lines, the beam would be more effective for SNM detection. From the previous results (Sec. 6.1.2), it was already shown that the radiation materials such as ^{232}Th or ^{241}Am modified the plasma spectra from radiation-modified air (e.g., Figs. 6.6 and 6.7) and these changes were recognized from laser-induced air-breakdown spectra. To stand out this spectral feature, the line-comparison method was used, which can show the ionization degree of surrounding air. The optimization parameter (FOM), therefore, was set as the ratio between two emission lines of nitrogen (NII / NI, NI: 744nm, NII: 777 nm). To reduce collection error of the spectral ratio, the FOM value was calculated from 10 air-breakdowns with each mirror shape. The plasma formation process is stochastic in the sense that a given beam shape will not produce the same plasma every time but its characteristics will vary from plasma to plasma because the initiation and growth conditions are statistical. Note that if the mirror does not generate a plasma for a certain time period, a FOM value was assigned to zero to exclude the mirror shape due to low plasma count rate.

To optimize the spectrum ratio with the DM, the ^{241}Am alpha sources was located near the focal region. As shown in Fig. 6.9, plasma light was collected by an optical fiber and analyzed by CCS 200 spectrometer. The DAQ system collected spectral signals and acoustic signals and saved the spectral data when the spectral intensity is higher than certain threshold level. All DAQ and DM operation were controlled by LabVIEW code.

Figure 6.16 shows the evaluation of FOM values with the radiation sources (^{241}Am). The optimization process was taken more than 100th generation, and on the figure, the top 10 highest FOM values were plotted. and the averaged value was added with a thick black line. Two vertical dotted lines indicated the moments, at which a level of mutation was changed to guide and accelerate the GA process to the optimized solution. If the mutation percentage is too big through whole optimization stage, then the GA will not be allowed to steadily climb the hill to the local maximum because it would jump around the peak in the parameter space. Thus, when the progress chart was flattened (at the 57th generation), the mutation percentage was changed from 20 % to 10 %, and again from 10 % to 5 % at the 83rd generation. For the optimization, the 777 nm/747 nm spectral ratio improved by roughly 50 % (from 1 to 1.5) and the best mirror figure is shown in Fig. 6.17, which have a multi-modal shape, as will be explained later.

Temporal evolution of the spectral ratios is shown in Fig. 6.18. Compared to early duration of the optimization (blue bars), the last 33 % results showed higher spectral ratio values (grey bars). As the beam shape developed and got optimized, the spectral ratio distribution experienced obvious improvement. To check radiation sensitivity (the ratio of 777 and 747 nm emission lines), the final optimized mirror results were compared to non-optimized mirror results in Fig. 6.19.

These were collected in the presence of weakly ionizing radiation ($<$ 100 nCi ^{241}Am). The rightward shift in the red histogram from the optimized mirror relative

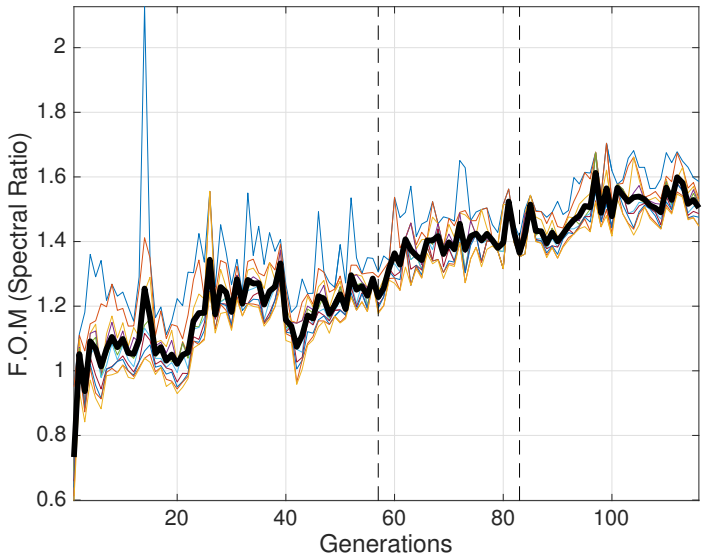

Figure 6.16 Spectral ratio (777/747 nm) optimization progress chart. The top 10 FOM values of each generation were plotted and average FOM was added as thick black line. Two vertical dotted lines indicate the moments when the mutation percentage changed.

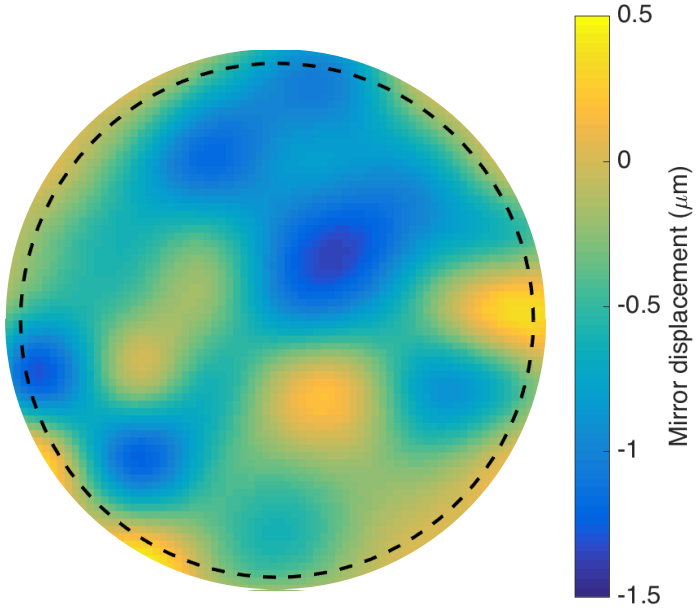

Figure 6.17 Mirror voltage distribution of the spectral optimization results

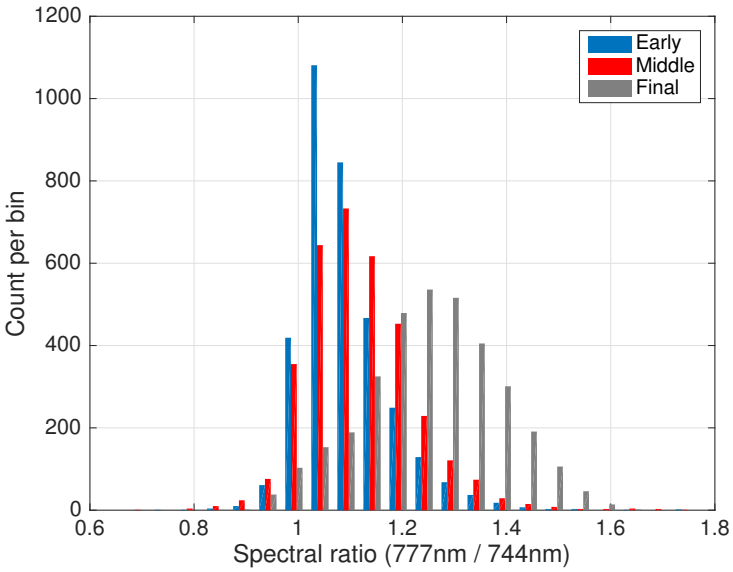

Figure 6.18 Histograms of spectral ratio optimization result. Three histograms represent early/middle/last 33 % results. As the optimization progresses, spectral ratio (FOM) becomes greater, at the last stage, peak values of the FOM are about 1.3.

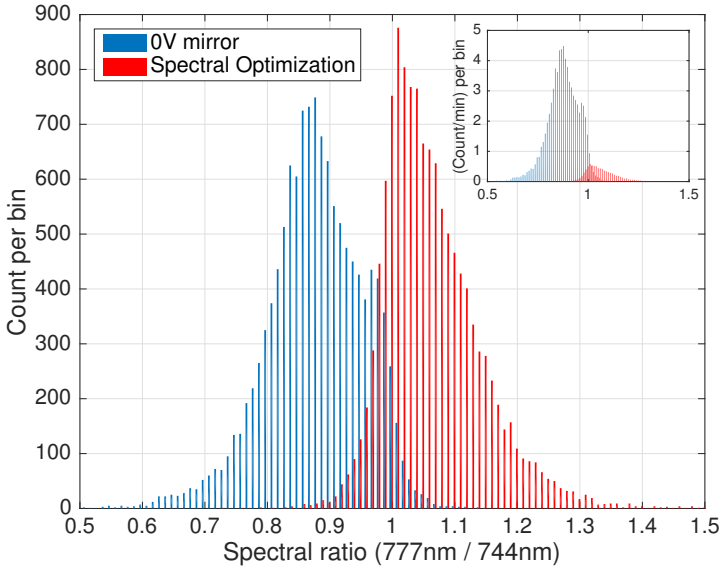

Figure 6.19 Spectral ratio comparison between two mirror shapes. The optimized mirror (red) generated higher spectral ratio than 0 V mirror results (blue). An inset figure shows time-normalized spectral ratio. The optimized mirror had a lower count rate.

to the blue histogram (flat mirror) shows the expected improvement in the ratio of atomic lines. For both measurements, a total of more than 13,000 data points were analyzed. The spectral ratio from flat mirror had a peak at 0.88 and the optimized result showed the peak spectral ratio at 1.01. Again, the ratio was defined as NII line intensity relative to NI lines. Therefore the laser beam from optimized mirror excited the neutral nitrogen (N I, 744 nm) more, having more the 1st degree of ionized nitrogen (N II, 777 nm). The histograms were clearly distinguishable, which were about one FWHM deviated from each other. However, as the explained above in Sec. 6.3.1, the optimized mirror lost the original beam alignment, suppressing count rate of the system significantly. The inset of Fig. 6.19 shows time-normalized histograms of two results. The optimized mirror histogram (red) was significantly lowered than flat mirror result.

Interestingly, that change in the optical characteristics of the plasma was also accompanied by a change in the plasma location, as shown in Fig. 6.20. This shows the temporal plasma location for the first, middle, and last of the plasmas formed during the spectral optimization. The breakdown positions were spatially moved by up to 4 cm along the beam line. For a 2-meter focal length, this few centimeter position variation was not sufficient to markedly increase/decrease the $f/\#$ of the optical system such that a sharper focus and more intense plasma results. Instead, as will be discussed below, the beam shape changed substantially, evolving into a bi-modal distribution, the effect of which was to extend the length along which radiation-induced ionization can impact the plasma formation. That impact can be gauged by examining the distributions with and without the presence of radiation sources. It should be noted again, the spectral optimization setup had acoustic detector at the downstream as shown in Fig. 6.9 (after the focus), thus, the plasma was moving toward upstream during the optimization process. Figure 6.21 compares the plasma location result between using the spectral optimization mirror and using flat mirror

shape. Clearly, the most probable location of the plasma was moved from zero to +2.5 cm.

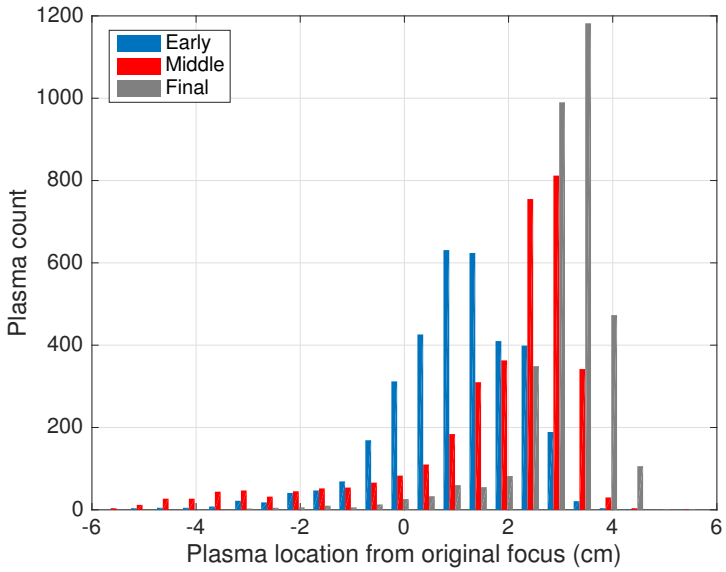

Figure 6.20 Plasma spatial movement during spectral optimization process. As the optimization proceeded, plasmas moved away from the acoustic detector.

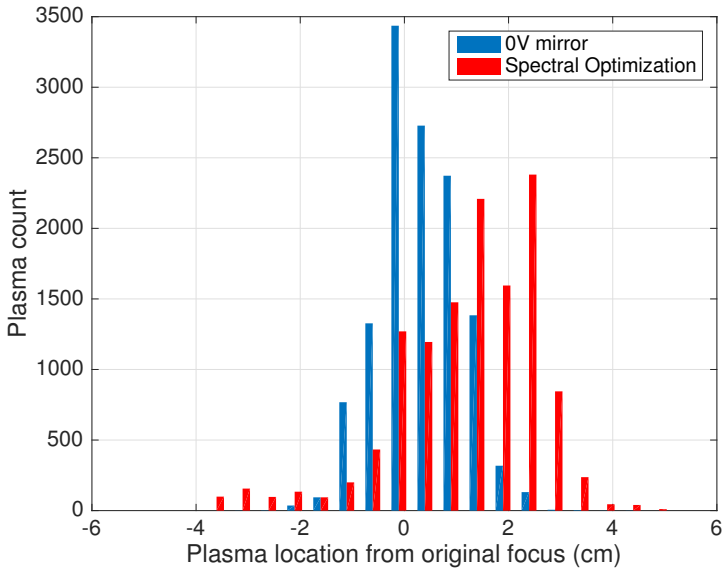

Figure 6.21 Plasma position comparison between the optimized mirror and a flat mirror. The optimized mirror generated plasmas at the upstream.

From the optimized mirror shape (see Fig. 6.17), a specific mirror shape (tip/tilt,

focus/defocus) was not founded. (c.f., the defocusing mirror shape was developed from the distance optimization, Fig. 6.15). Instead, two modal shapes were located at 12 o'clock and 8 o'clock. To check more details, the optimized beam profile was measured and compared with a flat mirror generating beam profile. Due to high beam intensity, a second-order reflection beam from a wedge is measured by a beam profiler (Thorlabs, BC106-VIS) with ND filters. Figure 6.22 shows the 2D images of the beam 5.5 cm before the focus (from the flat mirror) and beyond. The flat mirror (0 V) generated a circular beam shape with some fringes due to the various telescopes incorporated in the optical system (left). In contrast, the beam profile generated by the optimized mirror had three tails extending out from the hot spot and a highly asymmetric shape along the beam axis.

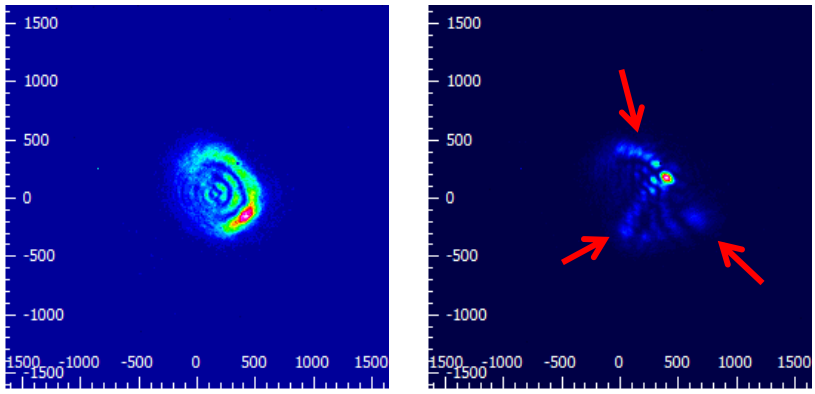

Figure 6.22 Beam profiles of 0 V mirror (left) and the optimized mirror (right) before the focus (−5.5cm). The optimized beam profile has a single hotspot at the center and three tails from the hot spot (red arrows).

In Fig. 6.23, beam shapes are captured at seven locations along the beam axis using 0 V mirror (top raw) and the optimized mirror (bottom row). The location of the focal point with 0 V, set as 0 cm, appears in the 3rd column. Different levels of ND filters were applied to the beam profiler to adjust proper saturation levels on the CCD. At the original focus (0 cm), the flat mirror focused the beam tightly and the beam had a 70 μm spot size with the hottest spot on beam center. However, for the optimized case, beam energy was shared between multiple modes in the beam front,

which impacts the energy level within each mode, as gauged by the saturation level of the sensor. At the original focus (0cm), the peak intensity of flat mirror case was 80 % of the saturation level of the beam profiler, but the optimized mirror peak intensity was only 30 %. As the beam passes the focal point, the 0 V flat mirror resulted in a rapidly expanding beam that quickly loses it intensity; however, the optimized mirror formed a bimodal distribution (two hot spots), which survived from 1.5 cm to 7.5 cm.

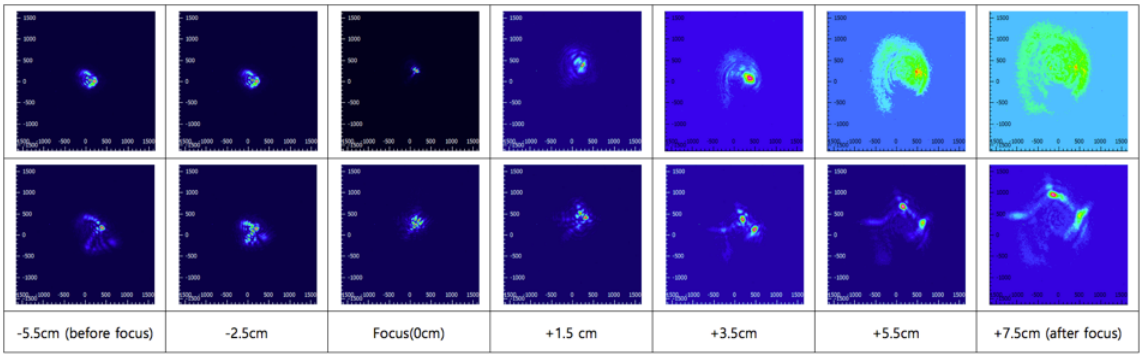

Figure 6.23 Beam profile table.

6.3.3 Detection of aerosol-induced plasmas

To understand the nature of the seed source of the plasma, the imaging system was built and the images were analyzed a motion of the rapidly moving, microscopic aerosol particles, spatially and temporally. A seemingly simpler method of identifying those plasmas that were initiated by dust is to use a Laser-Induced Breakdown Spectroscopy or LIBS modality in which non-air atomic peaks are sought in the optical spectra. For instance, the water-dominated aerosols reveal their participation in the seeding process through an observable hydrogen line, and carbon (organic particulate) or silicon (dirt) revealed through their appearance in the spectra. The imaging system was already described in Fig. 6.10.

The illuminating 405 nm beam focused and had a focal diameter of approximately 300 μm. The experimental requirement is to image any aerosols within this diameter just before the plasma discharge so that any spatial and temporal coincidence between

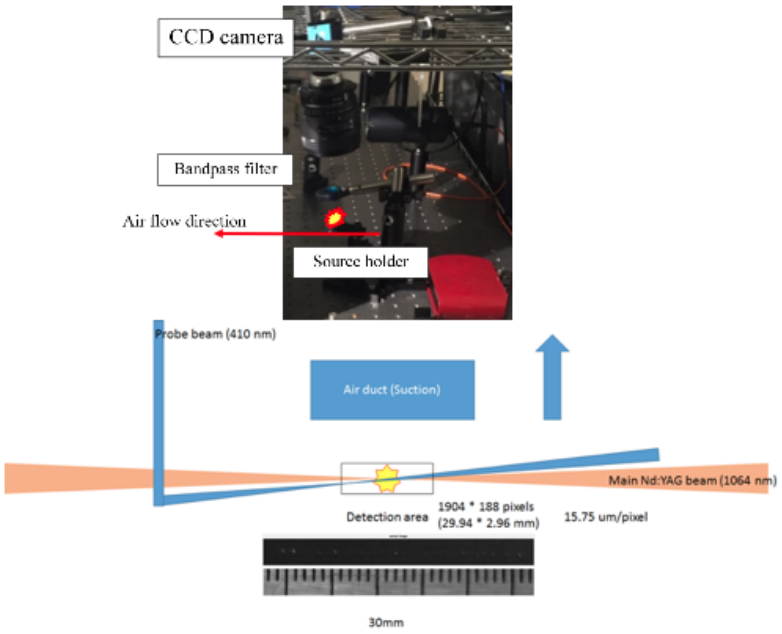

Figure 6.24 Photograph (top) and schematic diagram of the aerosol illumination system.

the aerosol streaks and the plasma formation can be observed. In order to have one-way directed aerosols, air-duct was installed at the one side. (see Figs. 6.24 and 6.25). Under one directional flow condition, aerosol speed was measured using CCD

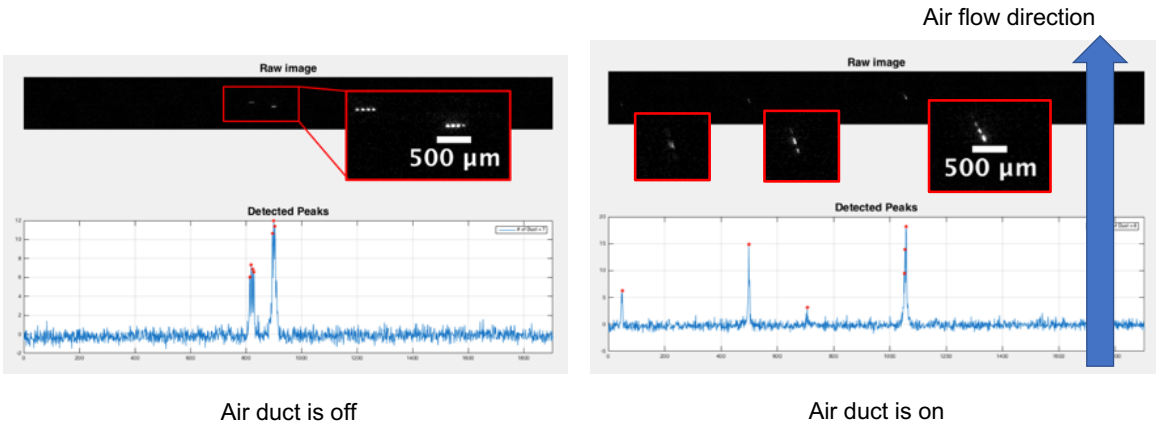

Figure 6.25 By introduce air-duct next to main laser beam focus, aerosol particles have one directional movement (upward direction in figure. Aerosol particles were imaged by a CCD camera and illumination source with air-duct (left) off and (right) on.

and illumination LED source. Using a pulse generator the illumination source was

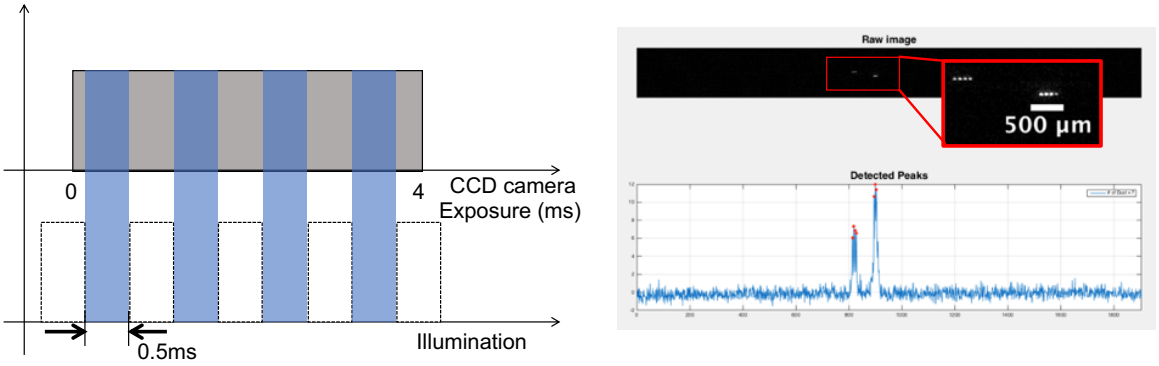

Figure 6.26 Dust movement is captured by CCD and the image was processed to find location. (Left) To image dusts, CCD camera records 4 ms duration, and a pulse generator illuminates dust four times during the camera exposure. (Right) Dust movement is recorded as dotted line due to four times of pulsed illuminations. Bottom graph shows peak a detection result. From given images, dust speed can be calculated.

turned on/off with 1 kHz with 50% duty factor while the CCD camera captured 4 ms. The timing and one example of dust movement were shown in Fig. 6.26. From this captured image, the dust speed can be calculated and range of the speed was from 100 m/s to 150 m/s when the air-duct was off and when the air-duct was on, particle move a lot faster (200 m/s to 300 m/s). The size of particles can be estimated from lateral dimension of the streak image. Some particles move along an angle, which make particles appear bigger. Through the post image process, image was rotated and the particle FWHM was estimated. In Fig. 6.27, a process of rotation and difference of the particle size was compared and the average particle size was 19.7±6.55 μm.

The plasma generation probability and aerosol-involvement probability were measured as a function of beam energy (per pulse). One expects that the plasma generation probability will be low until the photoionization threshold is approached above which a plasma will form on every laser shot. If a plasma is generated on every shot, whether or not a aerosol particle is present, then the aerosol generation probability will be low because there will be many more plasma generation events than aerosol transversal events. The important regime is the laser intensity just below the

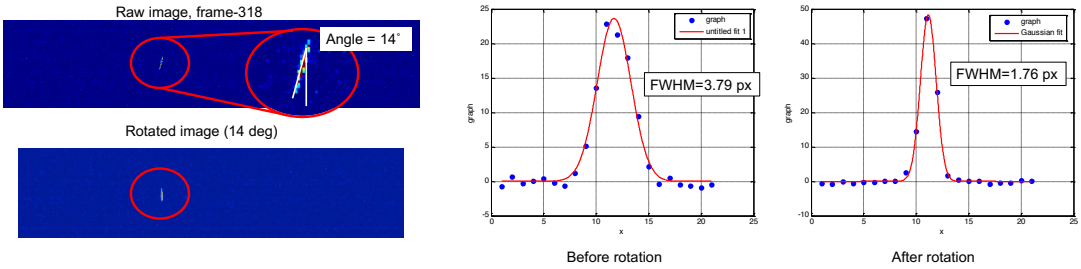

Figure 6.27 Example of tilted movement of a dust particle. The particle is diverted from the normal direction to 14 degree. False color is applied to identify the small particles. By rotating the image, estimated FWHMs of the particle sizes are shown (middle and right).

photoionization threshold where the greatest sensitivity to radiation sources can be found. In Fig. 6.28, the intensity profile was measured along with a line showing the photoionization threshold. When the main ns-laser pulse energy was focused by the

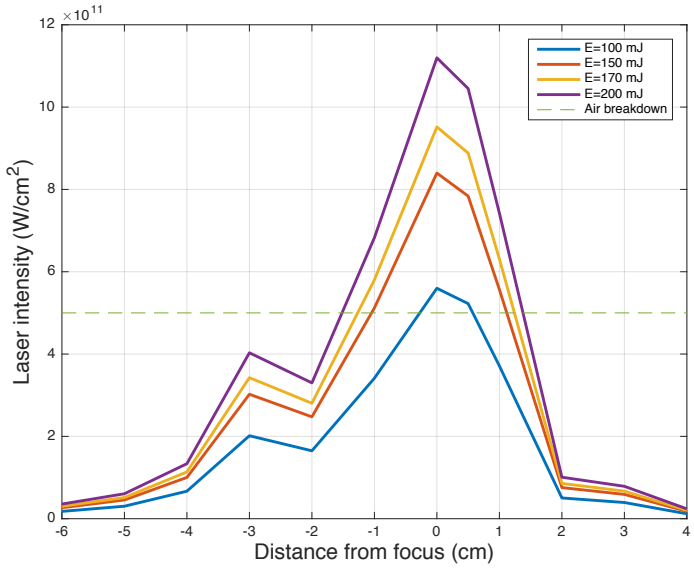

Figure 6.28 Laser intensity and air-breakdown threshold calculated from the measured beam profiles.

$f/35$ system, air-breakdown plasmas can be generated within ± 1.5 cm of the focus with 200 mJ of pulse energy. Because the clean air (aerosol-free) breakdown threshold is 100 times higher ($> 10^{11}$ W/cm^2) than the aerosol-induced breakdown threshold ($\sim 10^9$ W/cm^2) [229], plasma at lower energy ($< 10^{10}$ W/cm^2) could be initiated by

aerosol particles. The generation of plasma were measured and captured by triggering a CCD camera. The camera was triggered at -7.6 ms to capture dust image (before a main laser pulse arrives). And the plasma is imaged about 3 ms after its (potential) onset, a 3 ms of delay necessary to reduce the optical intensity so that the plasma position could be localized. The aerosol was then imaged as close in time as possible to the pulse arrival, but was restricted to 5 ms before the pulse beam because of the timing limitations of the camera operation speed related to size of region of interest. The detailed timing diagram is shown in Fig. 6.29. Note that a 89 nCi ^{241}Am sources modulate the radiation condition.

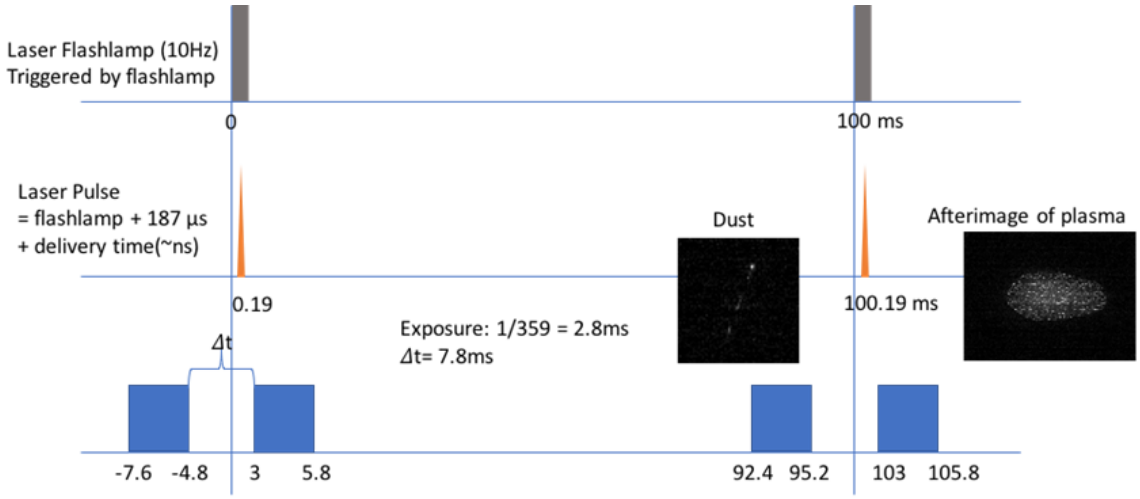

Figure 6.29 Timing diagram of the plasma formation, which starts at 0.19 ms. The blue boxes show the exposure windows of the delay-line camera, noting that there is a 2.81 ms delay from the arrival of the laser pulse and the opening of the plasma exposure window. The minimum possible frame separation allowed by the triggered camera, 7.8 ms is used to image the dust particle.

Figure 6.30 shows the beam-on views of the illumination and probe beams. Two beams (main beam and probe beam) were intentionally misaligned in horizontal axis (aerosol movement direction) to consider time gap between images, and aligned in vertical direction (z-axis) at the CCD focus plane. The relative horizontal positioning between the illumination and main beams depends on the aerosol velocity and angular offset. Specifically, during 2.8 ms pre-imaging stage, the dust particle left the streak

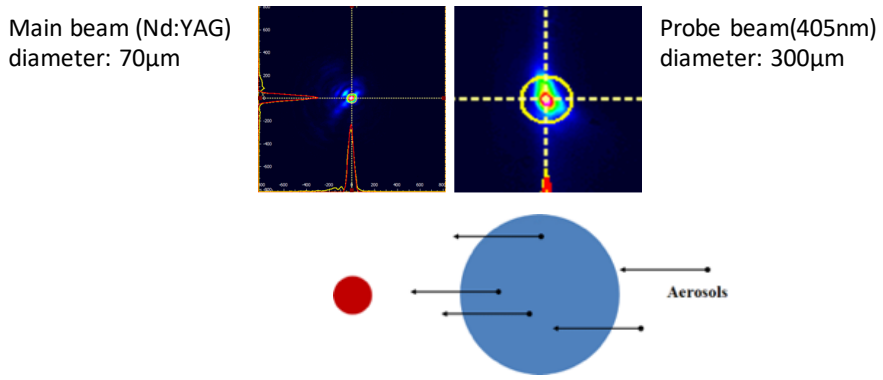

Figure 6.30 Illustration of vertical alignment of the 405 nm blue LD illumination beam and the 1064 nm Nd:YAG probe beam in the measured beam profile at the focus (top) and illustrated relative sizes (bottom)

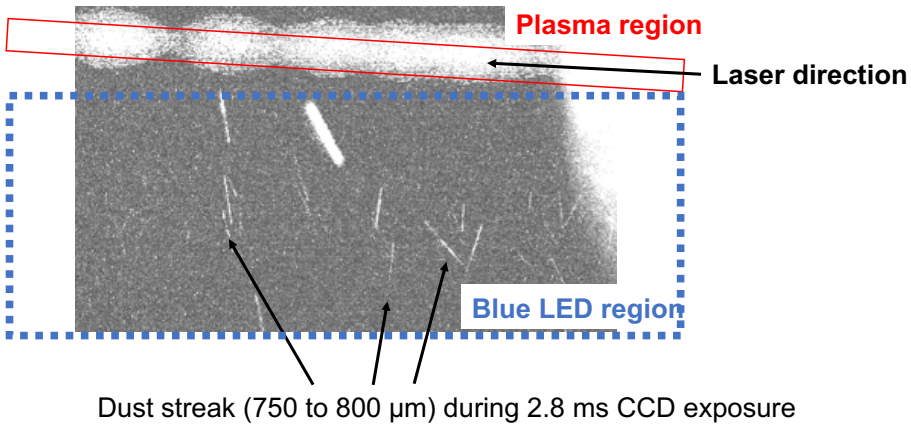

Figure 6.31 Accumulated z-projected image compilation of 50 images (25 dust streak images and 25 plasma images) showing the relative positioning of the 405 nm blue LD illumination beam and the 1064 nm Nd:YAG probe beam.

lengths of 750 μm (see streak lines in blue box in Fig. 6.31). This indicates a straight-line speed of 270 μm/ms. The aerosols imaged at a pre-illumination image (-7.6 to -4.8 ms) have a possibility to be ablated by main laser pulses only if those location is away from the main beam axis (red box region in Fig. 6.31) between 1.4 mm and 2.1 mm. The time required for the 270 μm/ms dust particle to traverse the 70 μm of probe beam is 0.25 ms, but the beginning of the dust particle track tells one where the dust particle at the beginning of the window, and the position some 7.8 ms later can be determined and correlated with the probe beam. Figure 6.32 (a) and (b) show

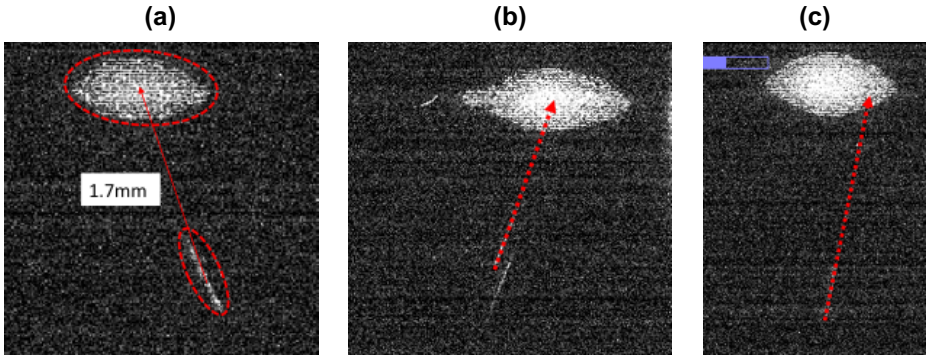

Figure 6.32 Dual successive images of dust and plasma, adjusted for contrast and brightness so that both can be observed, showing the separation [(a) 1.7 mm or (b) 1.5 mm] that results in a dust-initiated condition. (c) Dual successive images of dust and plasma, adjusted for contrast and brightness so that both can be observed, showing the separation (2.5 mm) that results in non-initiation by the dust.

examples in which the aerosol track is coincident, spatially and temporally, with the centroid of the after-image of the plasma. Figure 6.32 (c) shows an example of a track that, at first blush, appears to potentially initiate the plasma the collinear with the aerosol track. However, if the speed and positioning is taken into account, the separation of 2.5 mm implies that the particle is too far away to cause the plasma.

From this imaging system, plasma generation rate and dust-initiated plasma probability were measured and the results were plotted in Fig. 6.33. The ionization level was altered by two orders of magnitude from the background level of 2,000 ions/cm^3 to an ^{241}Am-induced ionization of 400,000 ions/cm^3. Nevertheless, if far from the

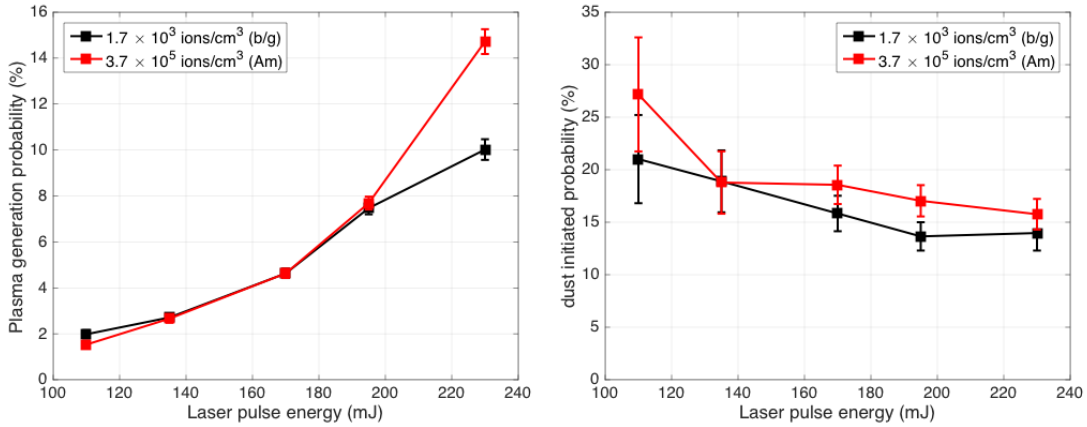

Figure 6.33 (Left) Plasma generation rate for the $f/35$ system as a function of pulse energy for two different levels of ionization. (Right) Probability that a plasma is initiated by an aerosol particle for the $f/35$ system as a function of pulse energy for two different levels of ionization.

photoionization threshold (I_{photo}) then the additional ionization has negligible consequence on the plasma generation rate. This observation is counterintuitive to the expectation that operation at those intensities where collisional cascading is dominant should be governed by seed-source initiation rather than multi-photon processes. However, this is consistent with our large collection of experimental results that indicate that the greatest sensitivity to seed-sources is for those experiments in which the laser intensity if nearest I_{photo}. The physical explanation for this observation is that the electric field is primed, readily to avalanche from any small perturbation in the environment. The increase in the plasma generation rate is roughly 50 %, as shown in Fig. 6.33 (left), for a laser profile that is not optimized, noting that the data was derived for the flat mirror case, rather than the optimized mirror figure. Figure 6.33 (right) reveals the percentage of plasmas initiated by aerosol particles that were imaged. As shown in the graphs, the number was quite high, at roughly 20 % regardless of the ionization level, at least for these relatively small ionization levels. Interestingly, the dust-initiated probability was higher when the ionization was higher, as one would expect given the higher charging of the dust in the environment.

One of the critical questions was whether aerosols could serve as long-term storage components for the radiation-induced ionization, which can be important if one is depending on the ionization to escape deliberate shielding of a SNM. As shown in Fig. 6.33 (right), the ionization near the targets do not modulate the sensitivity to a large degree. Furthermore, the results demonstrate that air ionization itself remains important even in an operational environment where high humidity or high dust-filled winds might spoil the entire approach. Instead, the results demonstrate the charged dust is still different than pristine dust and the count rate and spectral characteristics can still be converted into an ionization quantification.

6.4 Conclusion and future works

In conclusion, a new type of active interrogation technique for SNM detection using plasmas is reported. To induce plasma, a Nd:YAG laser is focused, and within the detection volume (near the focus), intensity is controlled below the air-breakdown threshold level to enhance the possibility of plasma generation by radiation-seeded ionizations. Previous studies showed that a radiation source could modulate surrounding environments (ionization orders), which were confirmed by optical emission spectra of plasmas. To generate specific mirror shapes that have better sensitivities for a certain ionization, a deformable mirror optimization was tested with the genetic algorithm. One of the prominent spectral features (ratio of N II by N I) was assigned as a FOM of the optimization. Through an optimization process, the values of NII emission over NI emission were changed from 1 to 1.5. The optimized beam profile was measured to show what features of the beam made this change. The beam had elongated the focal shape, and was fragmented (three tails from one hotspot in the center of the beam). This beam shape caused a slow intensity profile along the beam axis, rather than a fast rising/falling intensity profile near the focus. In addition, an involvement of aerosol in plasma generation was analyzed statistically. Probe beam

and imaging systems were aligned spatially and temporally to detect aerosol (or dust particles) that initiated breakdown phenomena. Because a breakdown threshold of aerosol is two order of magnitude lower than the air, a higher aerosol-initiated probability was expected at the low intensity level of laser, and it was confirmed experimentally. With a radiation source near the focus, the dust-initiated probability was higher, as one would expect, given the higher charging of the dust in the environment.

For practical deployment of long-range detection, some system modifications are recommended. With larger sized optics (keeping the same f-number of the system), the range of system could be extended to 30 m or 100 m with the same interaction volume. If the beam is expanded from a 7 mm diameter to 1", 5", 10", or 12" diameters − most simply accomplished through a telescope-sized mirror (see Fig. 6.34) − then the maximum achievable volume does not change, but instead, is realized at longer focal lengths, reflecting optical systems with equivalent f-number. With a 10" or 12" telescope mirror ($\sim$ \$1,000), the interrogation region can be moved from a 1 m to 30 m or 40 m long distance.

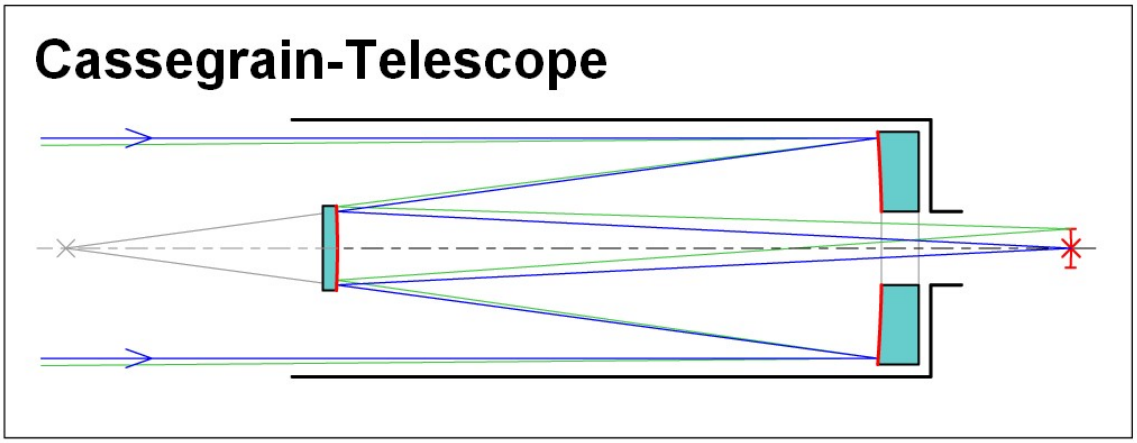

Figure 6.34 Telescopic mirror system used to enlarge the beam through a dual-mirror system.

As another alternative, a higher power laser system can enlarge a detection volume with the same level of energy density (intensity). For example, a CO_2 laser would be a good candidate because it can deliver higher energy, and its wavelength (λ_c =

10.6 μm) lowers air-breakdown threshold about 100 times as well. However, as target range increases, larger optical components are required to keep a proper level of f-number and to secure enough collection angle.

CHAPTER VII

Conclusions and outlook

7.1 Conclusions

The experiments in this thesis are proof-of-principle demonstrations of the use of high-power lasers for Homeland Security applications. The results of the experiments improve our understanding of laser-plasma interactions and the resulting radiation emission, as well as demonstrating the possibility that laser-plasma interactions may be used for these applications due to the unique characteristics of the radiation generated.

The main objectives of this work were to develop laser-plasma based radiation sources (neutron and THz) and an advanced laser-based SNM detection scheme. For the neutron generation experiment, the system has been simplified using a heavy-water liquid stream target, and it was the first demonstration of neutron production at room temperature conditions using pulse energies as low as a few millijoules. Without a bulk target-cooling system, a high time-averaged neutron flux (10^5 neutrons per second) was achieved, comparable to commercial neutron generators and far higher than previous laser-plasma studies in terms of neutrons per second per joule of laser energy. Another notable achievement in the thesis was a wide application of adaptive optics with active feedback techniques. The deformable mirror and the genetic algorithm improved the selected radiation signal (THz generation in Chapter V) and built

a specific mirror figure which is sensitive to certain emission spectra (SNM detection in Chapter VI). The combination of the deformable mirror and the genetic algorithm could be an important method for helping understand laser-plasma interaction physics.

7.2 Future applications and outlook

As future interrogation sources, these experimental studies demonstrated the potential for high power laser-based radiation sources. However, the laser-based scheme still has a number of challenges and room for improvement. For instance, to minimize unnecessary radiation exposure, directed radiation (anisotropic) sources are favorable. In order to have a directional (beam-like) DD fusion neutron source, a higher than 1 MeV energy, well-collimated deuteron beam is required. In this section, further follow-up experiments for practical applications will be suggested and possible applications will be reviewed.

7.2.1 Neutron generation

One challenge of the laser-based neutron sources presented in this thesis is neutron flux. A higher flux of neutron is required for better resolution of neutron imaging/scattering. Most of laser-driven neutron sources employ relatively high laser pulse energy ($>$ few joules) with low repetition-rate. Though high time-averaged neutron fluxes were achieved in this thesis, this flux is still a few orders lower compared to other high-flux neutron generating systems. In order to overcome this flux limitation, a high-power fiber laser can be used, which can support sub-millijoule, sub-picosecond pulses at 10 kHz or higher repetition-rate. In addition, using a coherent pulse stacking amplification technique, a fiber laser system generated a multi-millijoules of pulse energy [230]. If the fiber laser systems are employed for the neutron generation, a neutron flux can be scaled with its higher repetition rate. Of course, a complete

target surface recovery from the last laser pulse interaction should be guaranteed. In addition, as found in the preliminary research, the neutron flux was measured as a function of pulse duration or chamber backing pressure. The pulse duration experiment confirmed a nominal neutron generation at sub-picosecond pulse, which shows the possibility of neutron generation from a longer laser pulse (i.e., the fiber laser). By introducing background helium gas (up to atmospheric pressure), a vacuum-free neutron generation possibility was also examined.

7.2.2 THz generation

Although THz radiation has very attractive characteristics for security applications, it has struggled with a few challenges when considering real-world applications, not laboratory experiments, such as attenuation, and low conversion efficiency.

THz radiation experiences extreme atmospheric absorption due to water vapor. In Chapter V, the atmospheric absorption was also observed. With current THz source power levels, the absorption issue limits THz applications within a very small deploying distance. In addition, when a sample is covered by a metal or good conductive materials, THz imaging will fail; therefore, current THz sources can be utilized only in very limited conditions. Because of this issue, a relativistic laser-plasma THz source has been intensively studied to generate higher power THz radiation; however, the exact generation mechanisms are still unclear. In this thesis, THz power enhancement was achieved by a deformable mirror and the genetic algorithm without details of the mechanism. From the understanding of laser wavefronts, one could retrieve background interaction physics and figure out which mirror figures allow higher THz radiation. The activation feedback in this thesis controlled/optimized the laser system *spatially* using the deformable mirror. Because the THz generation process, especially in the case of two-color beams, is very sensitive to temporal structure of the laser pulse, an optimization of the laser temporal profile may have a greater impact

on THz generation. Thus, the active feedback could be applied to the acousto-optic programmable dispersive filter (Fastlite, Dazzler) to optimize a temporal profile of laser pulses.

7.2.3 SNM detection using ns-pulse laser

In order to have better SNM detection probability, the detection volume should be expanded as much as possible. Within the detection volume, the laser intensity (or E-field strength) is kept a little below air-breakdown threshold to allow the most sensitivity to radiation particles traversing the detection volume. To extend the detection volume, a large f-number optical system with a higher power laser would be required. For future applications ($>$ 100 m detection), a longer wavelength laser system is required to ensure enough dwell-time of the charge (ion or electron) within the high electric field, giving more chances to initiate plasma. The breakdown threshold is scaled with λ^{-2} empirically. Given 10.6 μm light (CO_2 laser), the effective detection volume will expand by a factor or 1,000. However, this application must be accompanied by a large collection system to secure enough statistical sampling of plasma spectra.

APPENDIX

APPENDIX A

List of publications

This thesis presents work reported by the Author in the following publications:

[1] **J. Hah**, G. M. Petrov, J. A. Nees, Z.-H. He, M. D. Hammig, K. Krushelnick, and A. G. R. Thomas, "High repetition-rate neutron generation by several-mJ, 35 fs pulses interacting with free-flowing D2O", *Appl. Phys. Lett.*, **109**, 144102 (2016)

[2] **J. Hah**, W. Jiang, Z.-H. He, J. A. Nees, B. Hou, A. G. R. Thomas, and K. Krushelnick, "Enhancement of THz generation by feedback-optimized wavefront manipulation", *Opt. Express*, **25**, 17271–17279 (2017)

[3] **J. Hah**, J. A. Nees, M. D. Hammig, K. Krushelnick, and A. G. R. Thomas, "Characterization of a high repetition-rate laser-driven short-pulsed neutron source", *Plasma Phys. Control. Fusion*, **60**, 054011 (2018)

The Author has also participated in research reported in the following publication(s) which is not presented in this thesis

[4] M. J. V. Streeter S. J. D. Dann, J. D. E. Scott, C. Baird, C. D. Murphy, S. Eardley, R. A. Smith, S. Rozario, J.-N. Gruse, S. P. D. Mangles, Z. Najmudin, S. Tata, M. Krishnamurthy, S.V. Rahul, D. Hazra, P. Pourmoussavi, J. Osterhoff,

J.Hah, N. Bourgeois, C. Thornton, C. D. Gregory, C. J. Hooker, O. Chekhlov, S. J. Hawkes, B. Parry, V. Marshall, Y. Tang, E. Springate, P. P. Rajeev, A. G. R. Thomas, and D. R. Symes, "Temporal feedback control of high-intensity laser pulses to optimize ultrafast heating of atomic clusters", *in press, Appl. Phys. Lett.*

[5] S. J. D. Dann, C. Baird, N. Bourgeois, O. Chekhov, S. Eardley, C. D. Gregory, J.-N. Gruse, **J.Hah**, D. Hazra, S. J. Hawkes, C. J. Hooker, K. Krushelnick, S. P. D. Mangles, V. Marshall, C. D. Murphy, Z. Najmudin, J. Nees, J. Osterhoff, B. Parry, P. Pourmoussavi, P. P. Rajeev, S. Rozario, D. Scott, R. A. Smith, E. Springate, Y. Tang, S. Tata, A. G. R. Thomas, C. Thornton, R. Venkata, D. R. Symes, and M. J. V. Streeter, "Laser wakefield acceleration with active feedback at 5 Hz", *in preparation*

BIBLIOGRAPHY

BIBLIOGRAPHY

[1] D. Albright and K. Kramer, "Civil HEU watch: Tracking Inventories of Civil Highly Enriched Uranium," Institute for Science and International Security p. 10 (2005).

[2] C. Grassley, M. Baucus, B. Thomas and C. Rangel, in *General Accounting Office, US Congress, GAO-03-770* (2003).

[3] D. Slaughter and D. Sprouse, "Screening cargo containers to remove a terrorist threat," Science and Technology Review pp. 12–15 (2004).

[4] M. Gai, "Scientists and home land security,", `http://astro.uconn.edu/Publications/IT/Gai_AveryPoint_29Sept11.pdf` (2011), Accessed: 2018-02-13.

[5] L. Gosnell, T. B., J. M. Hall, C. L. Jam, D. A. Knapp, Z. M. Koenig, S. J. Luke, B. A. Pohl, A. Schach von Wittenau and J. K. Wolford, "Gamma-ray identification of nuclear weapon materials," LLNL Technical Report, UCRL-ID-127436 (1997).

[6] T. Dragnev, "Non-destructive assay techniques for nuclear safeguards measurements," At. Energy Rev **11**, 341 (1973).

[7] R. Augustson and T. Reilly, "Fundamentals of passive nondestructive assay of fissionable material," LANL Technical Report, LA-5651-M (1974).

[8] J. Hall *et al.*, "The nuclear car wash: Neutron interrogation of cargo containers to detect hidden SNM," Nucl. Instr. Meth. Phys. Res. B **261**, 337 (2007).

[9] J. Church *et al.*, "Signals and interferences in the nuclear car wash," Nucl. Instr. Meth. Phys. Res. B **261**, 351 (2007).

[10] J. Stevenson, T. Gozani, M. Elsalim, C. Condron and C. Brown, "Linac based photofission inspection system employing novel detection concepts," Nucl. Instr. Meth. Phys. Res. A **652**, 124 (2011).

[11] M. Gmar, E. Berthoumieux, S. Boyer, F. Carrel, D. Doré, M.-L. Giacri, F. Lainé, B. Poumarède, D. Ridikas and A. Van Lauwe, "Detection of nuclear material by photon activation inside cargo containers," Proc. SPIE **6213**, 62130F (2006).

[12] A. G. Davies, A. D. Burnett, W. Fan, E. H. Linfield and J. E. Cunningham, "Terahertz spectroscopy of explosives and drugs," Mater. Today **11**, 18 (2008).

[13] A. Y. Pawar, D. D. Sonawane, K. B. Erande and D. V. Derle, "Terahertz technology and its applications," Drug Invent. Today **5**, 157 (2013).

[14] L. Ho, M. Pepper and P. Taday, "Terahertz spectroscopy: Signatures and fingerprints," Nat. Photon. **2**, 541 (2008).

[15] T. Tajima and J. M. Dawson, "Laser electron accelerator," Phys. Rev. Lett. **43**, 267 (1979).

[16] A. Modena *et al.*, "Electron acceleration from the breaking of relativistic plasma waves," Nature **377**, 606 (1995).

[17] R. Wagner, S.-Y. Chen, A. Maksimchuk and D. Umstadter, "Electron acceleration by a laser wakefield in a relativistically self-guided channel," Phys. Rev. Lett. **78**, 3125 (1997).

[18] A. Ting, C. I. Moore, K. Krushelnick, C. Manka, E. Esarey, P. Sprangle, R. Hubbard, H. R. Burris, R. Fischer and M. Baine, "Plasma wakefield generation and electron acceleration in a self-modulated laser wakefield accelerator experiment," Phys. Plasmas **4**, 1889 (1997).

[19] V. Malka *et al.*, "Electron acceleration by a wake field forced by an intense ultrashort laser pulse," Science **298**, 1596 (2002).

[20] S. P. D. Mangles *et al.*, "Monoenergetic beams of relativistic electrons from intense laser-plasma interactions," Nature **431**, 535 (2004).

[21] C. G. R. Geddes, C. Toth, J. van Tilborg, E. Esarey, C. B. Schroeder, D. Bruhwiler, C. Nieter, J. Cary and W. P. Leemans, "High-quality electron beams from a laser wakefield accelerator using plasma-channel guiding," Nature **431**, 538 (2004).

[22] J. Faure, Y. Glinec, A. Pukhov, S. Kiselev, S. Gordienko, E. Lefebvre, J. P. Rousseau, F. Burgy and V. Malka, "A laser–plasma accelerator producing monoenergetic electron beams," Nature **431**, 541 (2004).

[23] W. P. Leemans, B. Nagler, A. J. Gonsalves, C. Tóth, K. Nakamura, C. G. R. Geddes, E. Esarey, C. B. Schroeder and S. M. Hooker, "GeV electron beams from a centimetre-scale accelerator," Nat. Phys. **2**, 696 (2006).

[24] S. Kneip *et al.*, "Near-GeV acceleration of electrons by a nonlinear plasma wave driven by a self-guided laser pulse," Phys. Rev. Lett. **103**, 035002 (2009).

[25] D. H. Froula *et al.*, "Measurements of the critical power for self-injection of electrons in a laser wakefield accelerator," Phys. Rev. Lett. **103**, 215006 (2009).

[26] X. Wang *et al.*, "Quasi-monoenergetic laser-plasma acceleration of electrons to 2 GeV," Nat. Commun. **4**, 1988 (2013).

[27] R. D. Edwards *et al.*, "Characterization of a gamma-ray source based on a laser-plasma accelerator with applications to radiography," Appl. Phys. Lett. **80**, 2129 (2002).

[28] F. Albert *et al.*, "Isotope-specific detection of low-density materials with laser-based monoenergetic gamma-rays," Opt. Lett. **35**, 354 (2010).

[29] S. Cipiccia *et al.*, "A tuneable ultra-compact high-power, ultra-short pulsed, bright gamma-ray source based on bremsstrahlung radiation from laser-plasma accelerated electrons," J. Appl. Phys. **111**, 063302 (2012).

[30] W. P. Leemans *et al.*, "Observation of terahertz emission from a laser-plasma accelerated electron bunch crossing a plasma-vacuum boundary," Phys. Rev. Lett. **91**, 074802 (2003).

[31] J. van Tilborg, C. Schroeder, C. Filip, C. Tóth, C. Geddes, G. Fubiani, E. Esarey and W. Leemans, "Terahertz radiation as a bunch diagnostic for laser-wakefield-accelerated electron bunches," Phys. Plasmas **13**, 056704 (2006).

[32] E. L. Clark *et al.*, "Measurements of energetic proton transport through magnetized plasma from intense laser interactions with solids," Phys. Rev. Lett. **84**, 670 (2000).

[33] A. Maksimchuk, S. Gu, K. Flippo, D. Umstadter and V. Y. Bychenkov, "Forward ion acceleration in thin films driven by a high-intensity laser," Phys. Rev. Lett. **84**, 4108 (2000).

[34] R. A. Snavely *et al.*, "Intense high-energy proton beams from petawatt-laser irradiation of solids," Phys. Rev. Lett. **85**, 2945 (2000).

[35] I. S. Anderson, R. L. McGreevy and H. Z. Bilheux, *Neutron imaging and applications*, Vol. 200 (Springer, New York, NY, 2009).

[36] C. M. Brenner *et al.*, "Laser-driven x-ray and neutron source development for industrial applications of plasma accelerators," Plasma Phys. Control. Fusion **58**, 014039 (2016).

[37] I. Watts, M. Zepf, E. L. Clark, M. Tatarakis, K. Krushelnick, A. E. Dangor, R. Allott, R. J. Clarke, D. Neely and P. A. Norreys, "Measurements of relativistic self-phase-modulation in plasma," Phys. Rev. E **66**, 036409 (2002).

[38] D. Strickland and G. Mourou, "Compression of amplified chirped optical pulses," Opt. Commun. **56**, 219 (1985).

[39] V. Yanovsky *et al.*, "Ultra-high intensity- 300-TW laser at 0.1 Hz repetition rate.," Opt. Express **16**, 2109 (2008).

[40] M. Göppert-Mayer, "Über elementarakte mit zwei quantensprüngen," Annalen der Physik **401**, 273 (1931).

[41] P. A. Franken, A. E. Hill, C. W. Peters and G. Weinreich, "Generation of optical harmonics," Phys. Rev. Lett. **7**, 118 (1961).

[42] W. L. Kruer, *The physics of laser plasma interactions* (Reading, MA, Addison-Wesley Pub. Co. Inc,, 1988).

[43] P. Gibbon, *Short pulse laser interactions with matter* (London, Imperial College Press, 2007).

[44] A. Macchi, M. Borghesi and M. Passoni, "Ion acceleration by superintense laser-plasma interaction," Rev. Mod. Phys. **85**, 751 (2013).

[45] M. Passoni, C. Perego, A. Sgattoni and D. Batani, "Advances in target normal sheath acceleration theory," Phys. Plasmas **20**, 060701 (2013).

[46] S. C. Wilks, A. B. Langdon, T. E. Cowan, M. Roth, M. Singh, S. Hatchett, M. H. Key, D. Pennington, A. MacKinnon and R. A. Snavely, "Energetic proton generation in ultra-intense laser–solid interactions," Phys. Plasmas **8**, 542 (2001).

[47] P. McKenna, F. Lindau, O. Lundh, D. Neely, A. Persson and C.-G. Wahlström, "High-intensity laser-driven proton acceleration: influence of pulse contrast," Phil. Trans. R. Soc. A **364**, 711 (2006).

[48] M. Hegelich *et al.*, "MeV ion jets from short-pulse-laser interaction with thin foils," Phys. Rev. Lett. **89**, 085002 (2002).

[49] G. M. Petrov, L. Willingale, J. Davis, T. Petrova, A. Maksimchuk and K. Krushelnick, "The impact of contaminants on laser-driven light ion acceleration," Phys. Plasmas **17**, 103111 (2010).

[50] A. J. Mackinnon, M. Borghesi, S. Hatchett, M. H. Key, P. K. Patel, H. Campbell, A. Schiavi, R. Snavely, S. C. Wilks and O. Willi, "Effect of plasma scale length on multi-MeV proton production by intense laser pulses," Phys. Rev. Lett. **86**, 1769 (2001).

[51] D. T. Offermann, K. A. Flippo, J. Cobble, M. J. Schmitt, S. A. Gaillard, T. Bartal, D. V. Rose, D. R. Welch, M. Geissel and M. Schollmeier, "Characterization and focusing of light ion beams generated by ultra-intensely irradiated thin foils at the kilojoule scale," Phys. Plasmas **18**, 056713 (2011).

[52] B. Hou, J. A. Nees, Z. He, G. Petrov, J. Davis, J. H. Easter, A. G. R. Thomas and K. M. Krushelnick, "Laser-ion acceleration through controlled surface contamination," Phys. Plasmas **18**, 040702 (2011).

[53] L. Willingale *et al.*, "Comparison of bulk and pitcher-catcher targets for laser-driven neutron production," Phys. Plasmas **18**, 083106 (2011).

[54] J. T. Morrison *et al.*, "Selective deuteron production using target normal sheath acceleration," Phys. Plasmas **19**, 030707 (2012).

[55] L. Perkins, B. Logan, M. Rosen, M. Perry, T. D. de la Rubia, N. Ghoniem, T. Ditmire, P. Springer and S. Wilks, "The investigation of high intensity laser driven micro neutron sources for fusion materials research at high fluence," Nucl. Fusion **40**, 1 (2000).

[56] V. Kononov, M. Bokhovko, O. Kononov, N. Soloviev, W. Chu and D. Nigg, "Accelerator-based fast neutron sources for neutron therapy," Nucl. Instr. Meth. Phys. Res. A **564**, 525 (2006).

[57] M. Roth *et al.*, "Bright laser-driven neutron source based on the relativistic transparency of solids," Phys. Rev. Lett. **110**, 044802 (2013).

[58] S. J. Gitomer, R. D. Jones, F. Begay, A. W. Ehler, J. F. Kephart and R. Kristal, "Fast ions and hot electrons in the laser–plasma interaction," Phys. Fluids **29**, 2679 (1986).

[59] A. P. Fews, P. A. Norreys, F. N. Beg, A. R. Bell, A. E. Dangor, C. N. Danson, P. Lee and S. J. Rose, "Plasma ion emission from high intensity picosecond laser pulse interactions with solid targets," Phys. Rev. Lett. **73**, 1801 (1994).

[60] F. N. Beg, A. R. Bell, A. E. Dangor, C. N. Danson, A. P. Fews, M. E. Glinsky, B. A. Hammel, P. Lee, P. A. Norreys and M. Tatarakis, "A study of picosecond laser–solid interactions up to 10^{19} Wcm^{-2}," Phys. Plasmas **4**, 447 (1997).

[61] G. S. Sarkisov, V. Y. Bychenkov, V. N. Novikov, V. T. Tikhonchuk, A. Maksimchuk, S.-Y. Chen, R. Wagner, G. Mourou and D. Umstadter, "Self-focusing, channel formation, and high-energy ion generation in interaction of an intense short laser pulse with a He jet," Phys. Rev. E **59**, 7042 (1999).

[62] K. Krushelnick *et al.*, "Multi-MeV ion production from high-intensity laser interactions with underdense plasmas," Phys. Rev. Lett. **83**, 737 (1999).

[63] T. Ditmire, J. W. G. Tisch, E. Springate, M. B. Mason, N. Hay, R. A. Smith, J. Marangos and M. H. R. Hutchinson, "High-energy ions produced in explosions of superheated atomic clusters," Nature **386**, 54 (1997).

[64] M. Lezius, S. Dobosz, D. Normand and M. Schmidt, "Explosion dynamics of rare gas clusters in strong laser fields," Phys. Rev. Lett. **80**, 261 (1998).

[65] S. P. Hatchett *et al.*, "Electron, photon, and ion beams from the relativistic interaction of petawatt laser pulses with solid targets," Phys. Plasmas **7**, 2076 (2000).

[66] M. Allen, P. K. Patel, A. Mackinnon, D. Price, S. Wilks and E. Morse, "Direct experimental evidence of back-surface ion acceleration from laser-irradiated gold foils," Phys. Rev. Lett. **93**, 265004 (2004).

[67] T. E. Cowan *et al.*, "Ultralow emittance, multi-MeV proton beams from a laser virtual-cathode plasma accelerator," Phys. Rev. Lett. **92**, 204801 (2004).

[68] L. Romagnani *et al.*, "Dynamics of electric fields driving the laser acceleration of multi-MeV protons," Phys. Rev. Lett. **95**, 195001 (2005).

[69] A. Macchi, F. Cattani, T. V. Liseykina and F. Cornolti, "Laser acceleration of ion bunches at the front surface of overdense plasmas," Phys. Rev. Lett. **94**, 165003 (2005).

[70] A. P. L. Robinson, M. Zepf, S. Kar, R. G. Evans and C. Bellei, "Radiation pressure acceleration of thin foils with circularly polarized laser pulses," New Journal of Physics **10**, 013021 (2008).

[71] C. A. J. Palmer *et al.*, "Monoenergetic proton beams accelerated by a radiation pressure driven shock," Phys. Rev. Lett. **106**, 014801 (2011).

[72] S. Wilks, W. Kruer, M. Tabak and A. Langdon, "Absorption of ultra-intense laser pulses," Phys. Rev. Lett. **69**, 1383 (1992).

[73] H. Habara *et al.*, "Ion acceleration from the shock front induced by hole boring in ultraintense laser-plasma interactions," Phys. Rev. E **70**, 046414 (2004).

[74] L. Yin, B. Albright, B. Hegelich and J. Fernández, "GeV laser ion acceleration from ultrathin targets: The laser break-out afterburner," Laser Part. Beams **24**, 291 (2006).

[75] B. Hegelich *et al.*, "Experimental demonstration of particle energy, conversion efficiency and spectral shape required for ion-based fast ignition," Nuclear Fusion **51**, 083011 (2011).

[76] S. S. Bulanov *et al.*, "Accelerating monoenergetic protons from ultrathin foils by flat-top laser pulses in the directed-Coulomb-explosion regime," Phys. Rev. E **78**, 026412 (2008).

[77] N. Bennett *et al.*, "Development of the dense plasma focus for short-pulse applications," Phys. Plasmas **24**, 012702 (2017).

[78] C. Thoma, D. R. Welch, R. E. Clark, D. V. Rose and I. E. Golovkin, "Hybrid-pic modeling of laser-plasma interactions and hot electron generation in gold hohlraum walls," Phys. Plasmas **24**, 062707 (2017).

[79] M. Arai and K. Crawford, *Neutron Sources and Facilities* (Springer US, Boston, MA, 2009), pp. 13–30.

[80] 42 USC §16320. Spallation Neutron Source (d) Authorization of appropriations (1) Spallation Neutron Source Project, URL http://uscode.house.gov/view.xhtml?req=granuleid:USC-prelim-title42-section16320&num=0&edition=prelim.

[81] M. Roth, S. C. Vogel, M. A. M. Bourke, J. C. Fernandez, M. J. Mocko, S. Glenzer, W. Leemans, C. Siders and C. Haefner, Tech. Rep., Los Alamos National Lab.(LANL), Los Alamos, NM (United States) (2017).

[82] M. Kikuchi, K. Lackner and M. Q. Tran, *Fusion physics* (INTERNATIONAL ATOMIC ENERGY AGENCY, 2012).

[83] Evaluated Nuclear Data File (ENDF)/B-VIII, URL https://www-nds.iaea.org/exfor/e4explorer.htm.

[84] C. Toupin, E. Lefebvre and G. Bonnaud, "Neutron emission from a deuterated solid target irradiated by an ultraintense laser pulse," Phys. Plasmas **8**, 1011 (2001).

[85] S. Fritzler, Z. Najmudin, V. Malka, K. Krushelnick, C. Marle, B. Walton, M. S. Wei, R. J. Clarke and A. E. Dangor, "Ion heating and thermonuclear neutron production from high-intensity subpicosecond laser pulses interacting with underdense plasmas," Phys. Rev. Lett. **89**, 165004 (2002).

[86] S. Karsch, S. Düsterer, H. Schwoerer, F. Ewald, D. Habs, M. Hegelich, G. Pretzler, A. Pukhov, K. Witte and R. Sauerbrey, "High-intensity laser induced ion acceleration from heavy-water droplets," Phys. Rev. Lett. **91**, 015001 (2003).

[87] C. L. Ellison and J. Fuchs, "Optimizing laser-accelerated ion beams for a collimated neutron source," Phys. Plasmas **17**, 113105 (2010).

[88] T. Ditmire, J. Zweiback, V. Yanovsky, T. Cowan, G. Hays and K. Wharton, "Nuclear fusion from explosions of femtosecond laser-heated deuterium clusters," Nature **398**, 489 (1999).

[89] S. Ter-Avetisyan, M. Schnürer, D. Hilscher, U. Jahnke, S. Busch, P. V. Nickles and W. Sandner, "Fusion neutron yield from a laser-irradiated heavy-water spray," Phys. Plasmas **12**, 012702 (2005).

[90] D. P. Higginson *et al.*, "Production of neutrons up to 18 MeV in high-intensity, short-pulse laser matter interactions," Phys. Plasmas **18**, 100703 (2011).

[91] K. L. Lancaster *et al.*, "Characterization of ^{7}Li(p,n)^{7}Be neutron yields from laser produced ion beams for fast neutron radiography," Phys. Plasmas **11**, 3404 (2004).

[92] D. P. Higginson *et al.*, "Laser generated neutron source for neutron resonance spectroscopy," Phys. Plasmas **17**, 100701 (2010).

[93] C. Zulick *et al.*, "Energetic neutron beams generated from femtosecond laser plasma interactions," Appl. Phys. Lett. **102**, 124101 (2013).

[94] P. A. Norreys, A. P. Fews, F. N. Beg, A. R. Bell, A. E. Dangor, P. Lee, M. B. Nelson, H. Schmidt, M. Tatarakis and M. D. Cable, "Neutron production from picosecond laser irradiation of deuterated targets at intensities of 10^{19} Wcm^{-2}," Plasma Phys. Control. Fusion **40**, 175 (1998).

[95] G. Pretzler *et al.*, "Neutron production by 200 mJ ultrashort laser pulses," Phys. Rev. E **58**, 1165 (1998).

[96] J. Zweiback, R. A. Smith, T. E. Cowan, G. Hays, K. B. Wharton, V. P. Yanovsky and T. Ditmire, "Nuclear fusion driven by Coulomb explosions of large deuterium clusters," Phys. Rev. Lett. **84**, 2634 (2000).

[97] G. Grillon *et al.*, "Deuterium-Deuterium fusion dynamics in low-density molecular-cluster jets irradiated by intense ultrafast laser pulses," Phys. Rev. Lett. **89**, 065005 (2002).

[98] D. H. Auston and P. R. Smith, "Generation and detection of millimeter waves by picosecond photoconductivity," Appl. Phys. Lett. **43**, 631 (1983).

[99] M. Beck, H. Schäfer, G. Klatt, J. Demsar, S. Winnerl, M. Helm and T. Dekorsy, "Impulsive terahertz radiation with high electric fields from an amplifier-driven large-area photoconductive antenna," Opt. Express **18**, 9251 (2010).

[100] C. Vicario, A. V. Ovchinnikov, S. I. Ashitkov, M. B. Agranat, V. E. Fortov and C. P. Hauri, "Generation of 0.9-mJ thz pulses in DSTMS pumped by a Cr:Mg_2SiO_4 laser," Opt. Lett. **39**, 6632 (2014).

[101] H. Hamster, A. Sullivan, S. Gordon, W. White and R. W. Falcone, "Subpicosecond, electromagnetic pulses from intense laser-plasma interaction," Phys. Rev. Lett. **71**, 2725 (1993).

[102] D. J. Cook and R. M. Hochstrasser, "Intense terahertz pulses by four-wave rectification in air," Opt. Lett. **25**, 1210 (2000).

[103] K. Y. Kim, J. H. Glownia, A. J. Taylor and G. Rodriguez, "Terahertz emission from ultrafast ionizing air in symmetry-broken laser fields," Opt. Express **15**, 4577 (2007).

[104] M. D. Thomson, V. Blank and H. G. Roskos, "Terahertz white-light pulses from an air plasma photo-induced by incommensurate two-color optical fields," Opt. Express **18**, 23173 (2010).

[105] Z. He, "Laser wakefield acceleration using few-millijoule laser pulses at kilohertz repetition-rate," Ph. D. Thesis, University of Michigan (2014).

[106] R. Trebino, K. W. DeLong, D. N. Fittinghoff, J. N. Sweetser, M. A. Krumbügel, B. A. Richman and D. J. Kane, "Measuring ultrashort laser pulses in the time-frequency domain using frequency-resolved optical gating," Rev. Sci. Instrum. **68**, 3277 (1997).

[107] B. Cartwright, E. Shirk and P. Price, "A nuclear-track-recording polymer of unique sensitivity and resolution," Nucl. Instr. Meth. **153**, 457 (1978).

[108] R. Cassou and E. Benton, "Properties and applications of CR-39 polymeric nuclear track detector," Nucl. Track Detection **2**, 173 (1978).

[109] J. F. Ziegler, M. Ziegler and J. Biersack, "SRIM – The stopping and range of ions in matter (2010)," Nucl. Instr. Meth. Phys. Res. B **268**, 1818 (2010).

[110] J. A. Frenje *et al.*, "Absolute measurements of neutron yields from DD and DT implosions at the OMEGA laser facility using CR-39 track detectors," Rev. Sci. Instrum. **73**, 2597 (2002).

[111] D. A. Glaser, "Some effects of ionizing radiation on the formation of bubbles in liquids," Phys. Rev. **87**, 665 (1952).

[112] R. E. Apfel, "The superheated drop detector," Nucl. Instr. Meth. **162**, 603 (1979).

[113] H. Ing and H. Birnboim, "A bubble-damage polymer detector for neutrons," Nucl. Tracks Radiat. Meas. **8**, 285 (1984).

[114] J. Schulze, W. Rosenstock and H. Kronholz, "Measurements of fast neutrons by bubble detectors," Radiat. Prot. Dosimetry **44**, 351 (1992).

[115] H. Bonin, G. Desnoyers and T. Cousins, "Fast neutron dosimetry and spectroscopy using bubble detectors," Radiat. Prot. Dosimetry **46**, 265 (1993).

[116] F. d'Errico and W. Alberts, "Superheated-drop (bubble) neutron detectors and their compliance with ICRP-60," Radiat. Prot. Dosimetry **54**, 357 (1994).

[117] F. d'Errico, W. Alberts, G. Curzio, S. Guldbakke, H. Kluge and M. Matzke, "Active neutron spectrometry with superheated drop (bubble) detectors," Radiat. Prot. Dosimetry **61**, 159 (1995).

[118] W. Rosenstock, J. Schulze, T. Köble, G. Kruzinski, P. Thesing, G. Jaunich and H. Kronholz, "Estimation of neutron energy spectra with bubble detectors: Potential and limitations," Radiat. Prot. Dosimetry **61**, 133 (1995).

[119] F. Vanhavere, M. Loos, A. Plompen, E. Wattecamps and H. Thierens, "A combined use of the BD-PND and BDT bubble detectors in neutron dosimetry," Radiat. Meas. **29**, 573 (1998).

[120] F. d'Errico, "Fundamental properties of superheated drop (bubble) detectors," Radiat. Prot. Dosimetry **84**, 55 (1999).

[121] S. Agosteo, M. Silari and L. Ulrici, "Improved response of bubble detectors to high energy neutrons," Radiat. Prot. Dosimetry **88**, 149 (2000).

[122] G. Zhang *et al.*, "Study on bubble detectors used as personal neutron dosimeters," Appl. Radiat. Isot. **69**, 1453 (2011).

[123] F. Castillo, B. Leal, H. Martìnez, J. Rangel and P. G. Reyes, "Measurements of fast neutrons by bubble detectors," AIP Conference Proceedings **1544**, 31 (2013).

[124] P. K. Mondal, R. Sarkar and B. K. Chatterjee, "Response of superheated droplet detector (SDD) and bubble detector (BD) to interrupted irradiations," Nucl. Instr. Meth. Phys. Res. A **857**, 111 (2017).

[125] M. Gherendi *et al.*, "Super-heated fluid detectors for neutron measurements at jet," J. Optoelectron. Adv. Mater. **10**, 2092 (2008).

[126] H. Ing, "Neutron measurements using bubble detectors—terrestrial and space," Radiat. Meas. **33**, 275 (2001).

[127] V. P. Skripov, *Metastable liquids* (New York, NY, Wiley, 1974).

[128] `https://assets.thermofisher.com/TFS-Assets/CAD/product-images/F72973~p.eps-250.jpg`, Accessed: 2018-02-10.

[129] G. F. Knoll, *Radiation detection and measurement* (Hoboken, NJ, John Wiley & Sons, 2010), 4th ed.

[130] E. Sakai, "Present status of room temperature semiconductor detectors," Nucl. Instr. Meth. **196**, 121 (1982).

[131] P. Siffert, A. Cornet, R. Stuck, R. Triboulet and Y. Marfaing, "Cadmium telluride nuclear radiation detectors," IEEE Trans. Nucl. Sci. **22**, 211 (1975).

[132] P. Siffert, "Cadmium telluride detectors and applications," MRS Proceedings **16** (1982).

[133] D. McGregor and H. Hermon, "Room-temperature compound semiconductor radiation detectors," Nucl. Instr. Meth. Phys. Res. A **395**, 101 (1997), proceedings of the Fourth International Workshop on GaAs Detectors and Related Compounds.

[134] `https://www.nuclear-power.net/wp-content/uploads/2015/03/attenuation.png`, Accessed: 2018-01-30.

[135] H. W. Babcock, "The possibility of compensating astronomical seeing," PASP **65**, 229 (1953).

[136] F. Eisenhauer, R. Schödel, R. Genzel, T. Ott, M. Tecza, R. Abuter, A. Eckart and T. Alexander, "A geometric determination of the distance to the galactic center," ApJ **597**, L121 (2003).

[137] R. Tyson and V. Lakshminarayanan, "Adaptive optics," J. Mod. Opt. **59**, 1032 (2012).

[138] M. J. Booth, "Adaptive optics in microscopy," Phil. Trans. R. Soc. A **365**, 2829 (2007).

[139] J. Liang, D. R. Williams and D. T. Miller, "Supernormal vision and high-resolution retinal imaging through adaptive optics," J. Opt. Soc. Am. A **14**, 2884 (1997).

[140] O. Albert, H. Wang, D. Liu, Z. Chang and G. Mourou, "Generation of relativistic intensity pulses at a kilohertz repetition rate," Opt. Lett. **25**, 1125 (2000).

[141] C. Danson *et al.*, "Vulcan petawatt—an ultra-high-intensity interaction facility," Nucl. Fusion **44**, S239 (2004).

[142] S.-W. Bahk, P. Rousseau, T. A. Planchon, V. Chvykov, G. Kalintchenko, A. Maksimchuk, G. A. Mourou and V. Yanovsky, "Generation and characterization of the highest laser intensities (10^{22} W/cm^2)," Opt. Lett. **29**, 2837 (2004).

[143] M. Borghesi, "Laser-driven ion acceleration: State of the art and emerging mechanisms," Nucl. Instr. Meth. Phys. Res. A **740**, 6 (2014), Proceedings of the first European Advanced Accelerator Concepts Workshop 2013.

[144] T. Z. Esirkepov *et al.*, "Proposed double-layer target for the generation of high-quality laser-accelerated ion beams," Phys. Rev. Lett. **89**, 175003 (2002).

[145] H. Schwoerer, S. Pfotenhauer, O. Jackel, K. U. Amthor, B. Liesfeld, W. Ziegler, R. Sauerbrey, K. W. D. Ledingham and T. Esirkepov, "Laser-plasma acceleration of quasi-monoenergetic protons from microstructured targets," Nature **439**, 445 (2006).

[146] M. Chen, A. Pukhov, T. P. Yu and Z. M. Sheng, "Enhanced collimated GeV monoenergetic ion acceleration from a shaped foil target irradiated by a circularly polarized laser pulse," Phys. Rev. Lett. **103**, 024801 (2009).

[147] A. A. Andreev, S. Steinke, T. Sokollik, M. Schnürer, S. T. Avetsiyan, K. Y. Platonov and P. V. Nickles, "Optimal ion acceleration from ultrathin foils irradiated by a profiled laser pulse of relativistic intensity," Phys. Plasmas **16**, 013103 (2009).

[148] O. Klimo, J. Psikal, J. Limpouch, J. Proska, F. Novotny, T. Ceccotti, V. Floquet and S. Kawata, "Short pulse laser interaction with micro-structured targets: simulations of laser absorption and ion acceleration," New J. Phys. **13**, 053028 (2011).

[149] D. Margarone *et al.*, "Laser-driven proton acceleration enhancement by nanostructured foils," Phys. Rev. Lett. **109**, 234801 (2012).

[150] D. Khaghani *et al.*, "Enhancing laser-driven proton acceleration by using micropillar arrays at high drive energy," Scientific Reports **7**, 11366 (2017).

[151] M. Richardson, D. Torres, C. DePriest, F. Jin and G. Shimkaveg, "Mass-limited, debris-free laser-plasma EUV source," Opt. Commun. **145**, 109 (1998).

[152] J. Myatt, W. Theobald, J. A. Delettrez, C. Stoeckl, M. Storm, T. C. Sangster, A. V. Maximov and R. W. Short, "High-intensity laser interactions with mass-limited solid targets and implications for fast-ignition experiments on OMEGA EP," Phys. Plasmas **14**, 056301 (2007).

[153] S. Buffechoux *et al.*, "Hot electrons transverse refluxing in ultraintense laser-solid interactions," Phys. Rev. Lett. **105**, 015005 (2010).

[154] A. Henig *et al.*, "Laser-driven shock acceleration of ion beams from spherical mass-limited targets," Phys. Rev. Lett. **102**, 095002 (2009).

[155] C. Spindloe, M. K. Tolley and E. Dival, "High repetition rate microtarget delivery to the Astra Gemini laser,", `https://www.clf.stfc.ac.uk/Pages/ar08-09_s7_high-repetition-rate-microtarget.pdf` (2009), Accessed: 2018-04-04.

[156] I. Prencipe *et al.*, "Targets for high repetition rate laser facilities: needs, challenges and perspectives," High Power Laser Science and Engineering **5**, e17 (2017).

[157] T. Nayuki, Y. Oishi, T. Fujii, K. Nemoto, T. Kayoiji, Y. Okano, Y. Hironaka, K. G. Nakamura, K. Kondo and K. Ueda, "Thin tape target driver for laser ion accelerator," Rev. Sci. Instrum. **74**, 3293 (2003).

[158] B. Hou, J. Easter, K. Krushelnick and J. A. Nees, "Generation of hard x rays by femtosecond laser pulse interaction with Cu in laminar helium flow in ambient air," Appl. Phys. Lett. **92**, 161501 (2008).

[159] L. Rymell and H. Hertz, "Droplet target for low-debris laser-plasma soft X-ray generation," Opt. Commun. **103**, 105 (1993).

[160] L. Malmqvist, L. Rymell, M. Berglund and H. M. Hertz, "Liquidjet target for laserplasma soft xray generation," Rev. Sci. Instrum. **67**, 4150 (1996).

[161] J. Davis, G. M. Petrov, T. Petrova, L. Willingale, A. Maksimchuk and K. Krushelnick, "Neutron production from ^{7}Li(d, xn) nuclear fusion reactions driven by high-intensity laser–target interactions," Plasma Phys. Control. Fusion **52**, 045015 (2010).

[162] A. Maksimchuk, A. Raymond, F. Yu, G. M. Petrov, F. Dollar, L. Willingale, C. Zulick, J. Davis and K. Krushelnick, "Dominant deuteron acceleration with a high-intensity laser for isotope production and neutron generation," Appl. Phys. Lett. **102**, 191117 (2013).

[163] S. Kar *et al.*, "Beamed neutron emission driven by laser accelerated light ions," New J. Phys. **18**, 053002 (2016).

[164] M. Nantel *et al.*, "Temporal contrast in Ti:sapphire lasers, characterization and control," IEEE J. Sel. Top. Quantum Electron. **4**, 449 (1998).

[165] I. Jovanovic, B. J. Comaskey, C. A. Ebbers, R. A. Bonner, D. M. Pennington and E. C. Morse, "Optical parametric chirped-pulse amplifier as an alternative to Ti:sapphire regenerative amplifiers," Appl. Opt. **41**, 2923 (2002).

[166] S. Backus, D. M. Gold, H. Nathel, H. C. Kapteyn, M. M. Murnane and W. White, "Prepulse suppression for high-energy ultrashort pulses using self-induced plasma shuttering from a fluid target," Opt. Lett. **18**, 134 (1993).

[167] D. M. Gold, "Direct measurement of prepulse suppression by use of a plasmashutter," Opt. Lett. **19**, 2006 (1994).

[168] G. Doumy, F. Quéré, O. Gobert, M. Perdrix, P. Martin, P. Audebert, J. C. Gauthier, J.-P. Geindre and T. Wittmann, "Complete characterization of a plasma mirror for the production of high-contrast ultraintense laser pulses," Phys. Rev. E **69**, 026402 (2004).

[169] V. Chvykov, P. Rousseau, S. Reed, G. Kalinchenko and V. Yanovsky, "Generation of 10^{11} contrast 50 TW laser pulses," Opt. Lett. **31**, 1456 (2006).

[170] D. Neely, P. Foster, A. Robinson, F. Lindau, O. Lundh, A. Persson, C.-G. Wahlström and P. McKenna, "Enhanced proton beams from ultrathin targets driven by high contrast laser pulses," Appl. Phys. Lett. **89**, 021502 (2006).

[171] A. Henig *et al.*, "Radiation-pressure acceleration of ion beams driven by circularly polarized laser pulses," Phys. Rev. Lett. **103**, 245003 (2009).

[172] F. Dollar *et al.*, "Control of energy spread and dark current in proton and ion beams generated in high-contrast laser solid interactions," Phys. Rev. Lett. **107**, 065003 (2011).

[173] M. Kaluza, J. Schreiber, M. I. K. Santala, G. D. Tsakiris, K. Eidmann, J. Meyer-ter Vehn and K. J. Witte, "Influence of the laser prepulse on proton acceleration in thin-foil experiments," Phys. Rev. Lett. **93**, 045003 (2004).

[174] P. McKenna *et al.*, "Effects of front surface plasma expansion on proton acceleration in ultraintense laser irradiation of foil targets," Laser Part. Beams **26**, 591 (2008).

[175] T. Z. Esirkepov *et al.*, "Prepulse and amplified spontaneous emission effects on the interaction of a petawatt class laser with thin solid targets," Nucl. Instr. Meth. Phys. Res. A **745**, 150 (2014).

[176] M. L. Zhou, J. H. Bin, D. Haffa, X. Q. Yan and J. Schreiber, "The impact of femtosecond pre-pulses on nanometer thin foils for laser-ion acceleration," Plasma Phys. Control. Fusion **59**, 055020 (2017).

[177] Y. Sentoku, T. E. Cowan, A. Kemp and H. Ruhl, "High energy proton acceleration in interaction of short laser pulse with dense plasma target," Physics of Plasmas **10**, 2009 (2003).

[178] Y. Glinec, G. Genoud, O. Lundh, A. Persson and C.-G. Wahlström, "Evolution of energy spectrum from laser-accelerated protons with a 100 fs intense prepulse," Appl. Phys. B **93**, 317 (2008).

[179] S. Bastiani, A. Rousse, J. P. Geindre, P. Audebert, C. Quoix, G. Hamoniaux, A. Antonetti and J. C. Gauthier, "Experimental study of the interaction of subpicosecond laser pulses with solid targets of varying initial scale lengths," Phys. Rev. E **56**, 7179 (1997).

[180] S. Lee *et al.*, "Effect of the prepulse width on the neutron generation in a femtosecond, deuterated, polystyrene plasma," J. Korean Phys. Soc. **51**, 1695 (2007).

[181] J. T. Morrison, E. A. Chowdhury, K. D. Frische, S. Feister, V. M. Ovchinnikov, J. A. Nees, C. Orban, R. R. Freeman and W. M. Roquemore, "Backward-propagating MeV electrons from 10^{18} W/cm^2 laser interactions with water," Phys. Plasmas **22**, 043101 (2015).

[182] B. Hou, J. Nees, A. Mordovanakis, M. Wilcox, G. Mourou, L. Chen, J.-C. Kieffer, C. Chamberlain and A. Krol, "Hard X-ray generation from solids driven by relativistic intensity in the lambda-cubed regime," Appl. Phys. B **83**, 81 (2006).

[183] Y. Kitagawa *et al.*, "Efficient fusion neutron generation using a 10-TW high-repetition rate diode-pumped laser," Plasma Fusion Res. **6**, 1306006 (2011).

[184] J. Davis and G. M. Petrov, "Angular distribution of neutrons from high-intensity laser–target interactions," Plasma Phys. Control. Fusion **50**, 065016 (2008).

[185] Y. Jiang, T. Lee and C. G. Rose-Petruck, "Generation of ultrashort hard-x-ray pulses with tabletop laser systems at a 2-kHz repetition rate," J. Opt. Soc. Am. B **20**, 229 (2003).

[186] Y. Jiang, T. Lee, W. Li, G. Ketwaroo and C. G. Rose-Petruck, "High-average-power 2-kHz laser for generation of ultrashort x-ray pulses," Opt. Lett. **27**, 963 (2002).

[187] J. M. Dawson, "Particle simulation of plasmas," Rev. Mod. Phys. **55**, 403 (1983).

[188] J. Hah, G. M. Petrov, J. A. Nees, Z.-H. He, M. D. Hammig, K. Krushelnick and A. G. R. Thomas, "High repetition-rate neutron generation by several-mJ, 35 fs pulses interacting with free-flowing D_2O," Appl. Phys. Lett. **109**, 144102 (2016).

[189] J. M. Yang *et al.*, "Neutron production by fast protons from ultraintense laser-plasma interactions," J. Appl. Phys. **96**, 6912 (2004).

[190] T. Žagar, J. Galy, J. Magill and M. Kellett, "Laser-generated nanosecond pulsed neutron sources: scaling from VULCAN to table-top," New J. Phys. **7**, 253 (2005).

[191] D. Giulietti *et al.*, "D+D fusion reactions in 10^{18} W/cm^2 intensity and repetitive laser-plasma interactions," Europhys. Lett. **119**, 65001 (2017).

[192] M. Tonouchi, "Cutting-edge terahertz technology," Nat. Photon. **1**, 97 (2007).

[193] P. H. Siegel, "Terahertz technology in biology and medicine," IEEE Trans. Microw. Theory Techn. **52**, 2438 (2004).

[194] H. B. Liu, H. Zhong, N. Karpowicz, Y. Chen and X. C. Zhang, "Terahertz spectroscopy and imaging for defense and security applications," Proc. IEEE **95**, 1514 (2007).

[195] B. Ferguson and X.-C. Zhang, "Materials for terahertz science and technology," Nat. Mater. **1**, 26 (2002).

[196] B. B. Hu and M. C. Nuss, "Imaging with terahertz waves," Opt. Lett. **20**, 1716 (1995).

[197] C. Sirtori, "Applied physics: Bridge for the terahertz gap," Nature **417**, 132 (2002).

[198] J. M. Chamberlain, "Where optics meets electronics: recent progress in decreasing the terahertz gap," Phil. Trans. R. Soc. Lond. A **362**, 199 (2004).

[199] R. Kleiner, "Filling the terahertz gap," Science **318**, 1254 (2007).

[200] B. Clough, J. Dai and X.-C. Zhang, "Laser air photonics: beyond the terahertz gap," Mater. Today **15**, 50 (2012).

[201] D. E. Spence, P. N. Kean and W. Sibbett, "60-fsec pulse generation from a self-mode-locked Ti:sapphire laser," Opt. Lett. **16**, 42 (1991).

[202] H. Hamster and R. W. Falcone, *Proposed Source of Sub-picosecond Far Infrared Radiation* (Springer Berlin Heidelberg, Berlin, Heidelberg, 1990), pp. 125–127.

[203] H. Hamster, A. Sullivan, S. Gordon and R. W. Falcone, "Short-pulse terahertz radiation from high-intensity-laser-produced plasmas," Phys. Rev. E **49**, 671 (1994).

[204] M. Kreß, T. Löffler, S. Eden, M. Thomson and H. G. Roskos, "Terahertz-pulse generation by photoionization of air with laser pulses composed of both fundamental and second-harmonic waves," Opt. Lett. **29**, 1120 (2004).

[205] T. Bartel, P. Gaal, K. Reimann, M. Woerner and T. Elsaesser, "Generation of single-cycle THz transients with high electric-field amplitudes," Opt. Lett. **30**, 2805 (2005).

[206] X. Xie, J. Dai and X.-C. Zhang, "Coherent control of THz wave generation in ambient air," Phys. Rev. Lett. **96**, 075005 (2006).

[207] H. Roskos, M. Thomson, M. Kreß and T. Löffler, "Broadband THz emission from gas plasmas induced by femtosecond optical pulses: From fundamentals to applications," Laser & Photonics Reviews **1**, 349 (2007).

[208] K. Y. Kim, A. J. Taylor, J. H. Glownia and G. Rodriguez, "Coherent control of terahertz supercontinuum generation in ultrafast laser-gas interactions," Nat. Photon. **2**, 605 (2008).

[209] E. Matsubara, M. Nagai and M. Ashida, "Ultrabroadband coherent electric field from far infrared to 200 THz using air plasma induced by 10 fs pulses," Appl. Phys. Lett. **101**, 011105 (2012).

[210] A. V. Borodin, N. A. Panov, O. G. Kosareva, V. A. Andreeva, M. N. Esaulkov, V. A. Makarov, A. P. Shkurinov, S. L. Chin and X.-C. Zhang, "Transformation of terahertz spectra emitted from dual-frequency femtosecond pulse interaction in gases," Opt. Lett. **38**, 1906 (2013).

[211] X.-Y. Peng *et al.*, "Strong terahertz radiation from air plasmas generated by an aperture-limited gaussian pump laser beam," Appl. Phys. Lett. **94**, 101502 (2009).

[212] D. Kuk, Y. J. Yoo, E. W. Rosenthal, N. Jhajj, H. M. Milchberg and K. Y. Kim, "Generation of scalable terahertz radiation from cylindrically focused two-color laser pulses in air," Appl. Phys. Lett. **108**, 121106 (2016).

[213] Z. H. He, B. Hou, V. Lebailly, J. A. Nees, K. Krushelnick and A. G. R. Thomas, "Coherent control of plasma dynamics," Nat. Commun. **6**, 7156 (2015).

[214] A. C. Englesbe, Z. He, J. A. Nees, A. G. Thomas, A. Schmitt-Sody and K. Krushelnick, "Control of the configuration of multiple femtosecond filaments in air by adaptive wavefront manipulation," Opt. Express **24**, 6071 (2016).

[215] H.-C. Wu, J. M. ter Vehn and Z.-M. Sheng, "Phase-sensitive terahertz emission from gas targets irradiated by few-cycle laser pulses," New J. Phys. **10**, 043001 (2008).

[216] L. Bergé, S. Skupin, C. Köhler, I. Babushkin and J. Herrmann, "3D numerical simulations of THz generation by two-color laser filaments," Phys. Rev. Lett. **110**, 073901 (2013).

[217] A. Debayle, L. Gremillet, L. Bergé and C. Köhler, "Analytical model for THz emissions induced by laser-gas interaction," Opt. Express **22**, 13691 (2014).

[218] N. V. Vvedenskii, A. I. Korytin, V. A. Kostin, A. A. Murzanev, A. A. Silaev and A. N. Stepanov, "Two-color laser-plasma generation of terahertz radiation using a frequency-tunable half harmonic of a femtosecond pulse," Phys. Rev. Lett. **112**, 055004 (2014).

[219] V. A. Andreeva *et al.*, "Ultrabroad terahertz spectrum generation from an air-based filament plasma," Phys. Rev. Lett. **116**, 063902 (2016).

[220] K.-Y. Kim, "Generation of coherent terahertz radiation in ultrafast laser-gas interactions," Phys. Plasmas **16**, 056706 (2009).

[221] C. D'Amico, A. Houard, M. Franco, B. Prade, A. Mysyrowicz, A. Couairon and V. T. Tikhonchuk, "Conical forward THz emission from femtosecond-laser-beam filamentation in air," Phys. Rev. Lett. **98**, 235002 (2007).

[222] C. Hauri, W. Kornelis, F. Helbing, A. Heinrich, A. Couairon, A. Mysyrowicz, J. Biegert and U. Keller, "Generation of intense, carrier-envelope phase-locked few-cycle laser pulses through filamentation," Appl. Phys. B **79**, 673 (2004).

[223] F. Théberge, W. Liu, P. T. Simard, A. Becker and S. L. Chin, "Plasma density inside a femtosecond laser filament in air: Strong dependence on external focusing," Phys. Rev. E **74**, 036406 (2006).

[224] J. Xie, W.-H. Fan and X. Chen, "Systematic experimental study on a highly efficient terahertz source based on two-color laser-induced air plasma," Laser Phys. **26**, 055002 (2016).

[225] H. L. Xu and S. L. Chin, "Femtosecond laser filamentation for atmospheric sensing," Sensors **11**, 32 (2011).

[226] T. Gozani, "Advances in accelerator based explosives detection systems," Nucl. Instr. Meth. Phys. Res. B **79**, 601 (1993).

[227] D. Strellis and T. Gozani, "Classifying threats with a 14-MeV neutron interrogation system," Appl. Radiat. Isot. **63**, 799 (2005), 8th International Conference on Applications of Nuclear Techniques.

[228] Gaussian Beam Propagation, URL https://lightmachinery.com/optical-design-center/more-optical-design-tools/gaussian-beam-propagation/.

[229] R. G. Pinnick, P. Chýlek, M. Jarzembski, E. Creegan, V. Srivastava, G. Fernandez, J. D. Pendleton and A. Biswas, "Aerosol-induced laser breakdown thresholds: wavelength dependence," Appl. Opt. **27**, 987 (1988).

[230] J. Ruppe, H. Pei, M. Sheikhsofla, S. Chen, R. Wilcox, W. Leemans, J. Nees and A. Galvanauskas, in *Conference on Lasers and Electro-Optics* (Optical Society of America, 2017), p. SM4I.1.